Interaction Region Design for a 100 TeV Proton-Proton Collider

DISSERTATION

zur Erlangung des akademischen Grades
doctor rerum naturalium
(Dr. rer. nat.)
im Fach Physik

Spezialisierung: Experimentalphysik

eingereicht an der
Mathematisch-Naturwissenschaftlichen Fakultät
Institut für Physik
der Humboldt-Universität zu Berlin

von
Herrn Roman Martin, M. Sc.

Präsidentin der Humboldt-Universität zu Berlin:
Prof. Dr.-Ing. Dr. Sabine Kunst

Dekan der Mathematisch-Naturwissenschaftlichen Fakultät:
Prof. Dr. Elmar Kulke

Gutachter:

1. Prof. Dr. Thomas Lohse
2. Prof. Dr. Andreas Jankowiak
3. Prof. Dr. Rüdiger Schmidt

Eingereicht am: 01.06.2017
Tag der mündlichen Prüfung: 23.11.2017

Abstract

The discovery of the Higgs boson is the start of a measurement program that aims to study the properties of this new particle with the highest possible precision in order to test the validity or the Standard Model of particle physics and to search for new physics beyond the Standard Model. For that purpose, the Large Hadron Collider (LHC) and its upgrade, the High Luminosity-LHC, will operate and produce data until 2035.

Following the recommendations of the European Strategy Group for Particle Physics, CERN launched the Future Circular Collider (FCC) study to design large scale particle colliders for high energy physics research in the post-LHC era. This thesis presents the development of the interaction region for FCC-hh, a proton-proton collider operating at $100\,\mathrm{TeV}$ center-of-mass energy.

The interaction region is the centerpiece of a collider as it determines the achievable luminosity. It is therefore crucial to aim for maximum production rates from the beginning of the design process. Starting from the lattices of LHC and its proposed upgrade, the High Luminosity LHC (HL-LHC), scaling strategies are derived to account for the increased beam rigidity. After identifying energy deposition from debris of the collision events as a driving factor for the layout, a general design strategy is drafted and implemented, unifying protection of the superconducting final focus magnets from radiation with a high luminosity performance. The resulting lattice has become the reference design for the FCC-hh project, having significant margins to the performance goals in terms of β^*.

The approach to protect the final focus magnets from radiation with thick shielding, limits the minimum β^* and therefore the luminosity. An alternative strategy to increase the magnet lifetime by distributing the radiation load more evenly is developed. A proof of principle of this method, the so-called Q1 split, is provided. In order to demonstrate the feasibility of the derived interaction region lattices, first dynamic aperture studies are conducted.

Zusammenfassung

Mit der Entdeckung des Higgs-Bosons hat ein Messprogramm begonnen, bei dem die Eigenschaften dieses neuen Teilchens mit der höchstmöglichen Präzision untersucht werden soll um die Gültigkeit des Standardmodells der Teilchenphysik zu prüfen und nach neuer Physik jenseits des Standardmodells zu suchen. Für dieses Ziel wird der Large Hadron Collider (LHC) und sein Upgrade, der High Luminosity-LHC bis etwa zum Jahr 2035 laufen und Daten produzieren.

Um an der Spitze der Teilchenphysik zu bleiben, hat die "European Strategy Group for Particle Physics" empfohlen, ambitionierte Nachfolgeprojekte für die Zeit nach dem LHC zu entwickeln. Entsprechend dieser Empfehlung hat das CERN die "Future Circular Collider" (FCC) -Studie gestartet, die die Machbarkeit neuer Speicherringe für Teilchenkollisionen (Collider) untersucht. In dieser Arbeit wird die Entwicklung der Wechselwirkungszonen für FCC-hh, einem Proton-Proton-Speicherring mit einer Schwerpunktsenergie von 100 TeV und einem Umfang von 100 km, beschrieben.

Die Wechselwirkungszone ist das Herzstück eines Colliders, da sie die erreichbare Luminosität bestimmt. Es ist daher entscheidend, schon früh im Entwicklungsprozess eine möglichst hohe Kollisionsrate anzustreben. Ausgehend von der optische Struktur der Wechselwirkungszonen des LHC und dem geplanten High Luminosity-LHC (HL-LHC) werden Strategien zur Skalierung hergeleitet um der höheren Strahlenergie gerecht zu werden. Bereits früh im Entwicklungsprozess wird die Strahlungsbelastung durch Teilchentrümmer vom Wechselwirkungspunkt als entscheidender Faktor für das Layout der Wechselwirkungszone identifiziert und eine allgemeine Design-Strategie, die den Schutz der supraleitenden Endfokussierungsmagnete mit einer hohen Luminosität verbindet, wird formuliert und implementiert. Aufgrund des deutlichen Spielraums in Bezug auf β^* wurde die resultierende Magnetstruktur zum Referenzdesign für das FCC-hh-Projekt.

Die Herangehensweise, die Endfokussierungsmagnete mit Hilfe von dicker Abschirmung vor Strahlung zu schützen, begrenzt das kleinste erreichbare β^* und damit die Luminosität. Eine alternative Strategie die Lebenszeit der Magnete zu erhöhen, indem die Strahlungsbelastung gleichmäßig verteilt wird, wird vorgestellt und die Wirksamkeit dieses Prinzips, dem so genannten Q1 Split, wird nachgewiesen. Um die Machbarkeit der entwickelten Wechselwirkungszone zu demonstrieren, werden erste Studien zur dynamische Apertur durchgeführt.

Erklärungen

Ich erkläre, dass ich die Dissertation selbständig und nur unter Verwendung der von mir gemäß §7 Abs. 3 der Promotionsordnung der Mathematisch-Naturwissenschaftlichen Fakultät, veröffentlicht im Amtlichen Mitteilungsblatt der Humboldt-Universität zu Berlin Nr. 126/2014 am 18.11.2014 angegebenen Hilfsmittel angefertigt habe.

Die vorliegende elektronische Version enthält minimale Korrekturen gegenüber der angenommenen Dissertationsschrift.

Contributions

The development of an interaction region for a particle collider is an immense task that can only be accomplished in a team effort. This thesis relies heavily on FLUKA simulations of collision debris, all of which have been run, analyzed and interpreted by the FCC-hh FLUKA team [1]. Furthermore, the valuable input from discussions with members of the FCC-hh optics design team [2] has contributed to the fast and substantial progress the interaction region design of FCC-hh has made in the past three years.

The original contributions to the FCC-hh project made in this thesis can be summarized as:

- Comparison of different interaction region lattices scaled from LHC and HL-LHC

- Deduction of a scaling law for the minimum β^*

- Formulation of a design strategy for the final focus triplet to minimize β^* in the presence of thick shielding

- Derivation and proof of concept for a novel radiation mitigation strategy for the first final focus triplet magnet, named the Q1 split

- Design of the current baseline interaction region lattice for FCC-hh

- First dynamic aperture studies with triplet errors

The results of the Q1 split (Chapter 5) have first been reported at the 7th International Particle Accelerator Conference (IPAC) 2016 [3]. The scaling strategies, the different L^* lattices as well as the dynamic aperture studies have been published in [4].

Roman Martin

Symbols and abbreviations

Symbols:

α_{s}	Longitudinal scaling factor
β, α, γ	Twiss parameters
β^*, α^*	β and α functions at the interaction point
γ_{L}	Lorentz factor
ϵ	Emittance
ϵ_{n}	Normalized Emittance
$\mu_{x,y}$	Horizontal/vertical phase advance
Ψ	Phase of the betatron oscillation
$\sigma_{x,y}$	Transverse beam size
$\sigma_{x'}$	Transverse beam divergence
θ	Crossing angle
B	Magnetic field
b_n, a_n	Normal and skew field component of the order n
c	Speed of light
$D_{x,y}$	Horizontal/vertical Dispersion
$D_{p_{x,y}}$	Dispersion of the horizontal/vertical momentum
e	Elementary charge
E	Particle energy
f	Focal length
k	Normalized quadrupole gradient
L	Length of an element or drift
L^*	Distance between interaction point and first quadrupole
$\mathcal{L}$	Luminosity
M	Transport matrix
$m_{i,j}$	Element (i,j) of the transport matrix
p	Particle momentum
Q	Tune
x, y, s	Transverse (x, y) and longitudinal (s) coordinates in the moving reference frame

Abbreviations

ATS	Achromatic Telescopic Squeeze
BSC	Beam Stay Clear
Dn	nth dipole from the IP
DA	Dynamic Aperture
DS	Dispersion Suppressor
FCC	Future Circular Collider
HL-LHC	High Luminosity LHC
IP	Interaction Point
IR	Interaction Region
LHC	Large Hadron Collider
Qn	nth quadrupole from the IP
QTn	Trim quadrupole belonging to Qn
RF	Radio Frequency
SSC	Superconducting Super Collider
TAS	Target Absorber Secondaries

Contents

Chapter 1

Introduction

In 2012 the standard model of particle physics was completed with the discovery of the Higgs boson in the ATLAS and CMS experiments [5, 6] at the Large Hadron Collider (LHC). Recent results of the LHC imply that the standard model works up to energy scales in the TeV range, the study of which just has just begun. However, there is strong evidence that the standard model must be modified in order to address fundamental questions unanswered yet, e.g. the nature of dark matter, the matter-antimatter asymmetry of the universe or supersymmetry. As a result the capabilities of the LHC and its high luminosity upgrade, the HL-LHC, must be fully exploited. Depending on the future results of these studies, it is likely that the probed energy range must be extended to search for new physics.

There are two fundamental approaches to the search for physics beyond the standard model: the first is to push the energy frontier to new levels in search for new physics. The means of choice for such a discovery machine is a high energy proton-proton collider as protons have a high mass and thus emit significantly less synchrotron radiation than electrons, so the reachable energy is limited by magnet strength and circumference only. The second approach is to use precision measurements of properties of the Higgs boson as well as searches for rare decays indicating new physics. In this case, a high intensity electron-positron collider is an attractive solution, due to cleaner experimental conditions as collisions of elementary particle have no underlying events. Furthermore the energy and momentum of the colliding particles are known more precisely than in a proton-proton collider.

Following the recommendations of the European Strategy Group for Particle Physics [7], CERN has launched the Future Circular Collider (FCC) study [8] exploring possible designs of storage rings for the post-LHC era. Among the studied options are a High Energy upgrade of the LHC (HE-LHC), an e^+e^- collider (FCC-ee) and a hadron collider with a focus on proton-proton collisions at a center-of-mass energy of 100 TeV and the option of heavy ion operation (FCC-hh). Another potential option is an electron-proton collider (FCC-he) providing deep-inelastic scattering collision to study the quark structure of the proton.

FCC-ee: FCC-ee is a high-luminosity circular electron-positron collider envisioned to operate at center-of-mass energies from 90 to 350 GeV, allowing high-precision measurements of the properties of the Z, W and Higgs bosons as well as the top quark. It is considered to be a predecessor of FCC-hh and hosted in the same 100 km tunnel. Synchrotron radiation limits the beam energy of FCC-ee well below
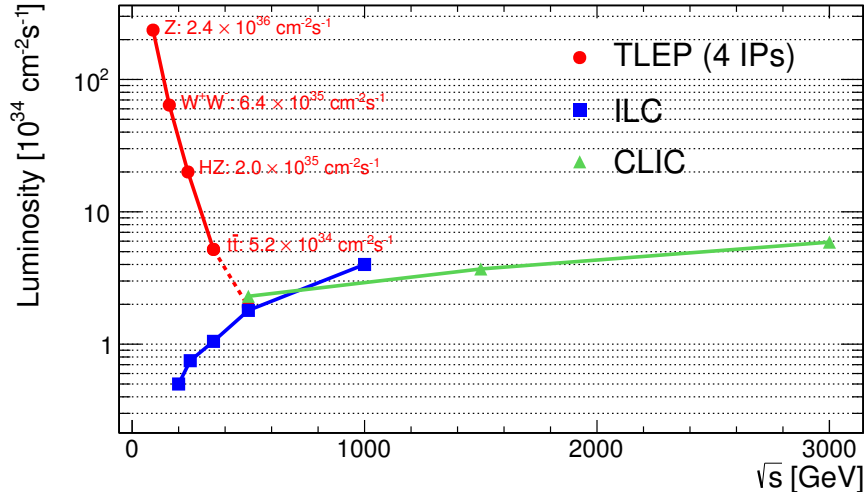
1

Figure 1.1: Expected luminosity of FCC-ee (TLEP) with four Interaction Points (IPs) as a function of the center-of-mass energy $\sqrt{s}$ compared to ILC and CLIC [11].

that of linear lepton collider projects such as the International Linear Collider (ILC) and the Compact LInear Collider (CLIC) [9, 10]. However, higher collision rates, higher beam current and the possibility to install up to four experiments allow for a much higher luminosity in FCC-ee as illustrated in Fig. 1.1. This makes FCC-ee the ideal candidate for precision measurements and the search for rare decays in the center-of-mass energy range below 500 GeV.

FCC-hh: FCC-hh is a proton-proton collider with a center-of-mass energy of 100 TeV with the option to operate with heavy ions. The ring circumference is determined by the magnetic field strength of the arc dipole magnets. With dipoles based on Nb_3Sn technology a field of 16 T is achievable, resulting in a circumference of about 100 km. A possible location for the tunnel in the Geneva area is illustrated in Fig. 1.2.

An alternative option is the **HE-LHC**, also studied in the scope of the FCC study. In this project, the Nb_3Sn magnet technology of FCC-hh is used in the 26.7 km long LHC tunnel. With a magnetic strength of 16-20 T this would allow to collide protons at a center-of-mass energy of up to 33 TeV [13] at considerably lower costs than the other FCC options, as large parts of the required infrastructure, specifically the tunnel, already exist.

The current layout of FCC-hh is shown in Fig. 1.3. It consists of straight sections with various functionalities, connected by arc sections bending the beam on a circular orbit. Like the LHC, FCC-hh features two high luminosity Interaction Regions (IRs) for general purpose experiments in the opposing straight section A and G as well two low luminosity IRs in the sections L and B that also contain the injection. One proposal for an experiment in the low-luminosity IRs is **FCC-he** where one proton beam of FCC-hh is brought in collision with an electron beam provided by a recirculating energy recovery linac as designed for the LHeC project. FCC-he is envisioned to operate in parallel to the main experiments in FCC-hh.

In addition to the interaction regions, there are dedicated short straight sections
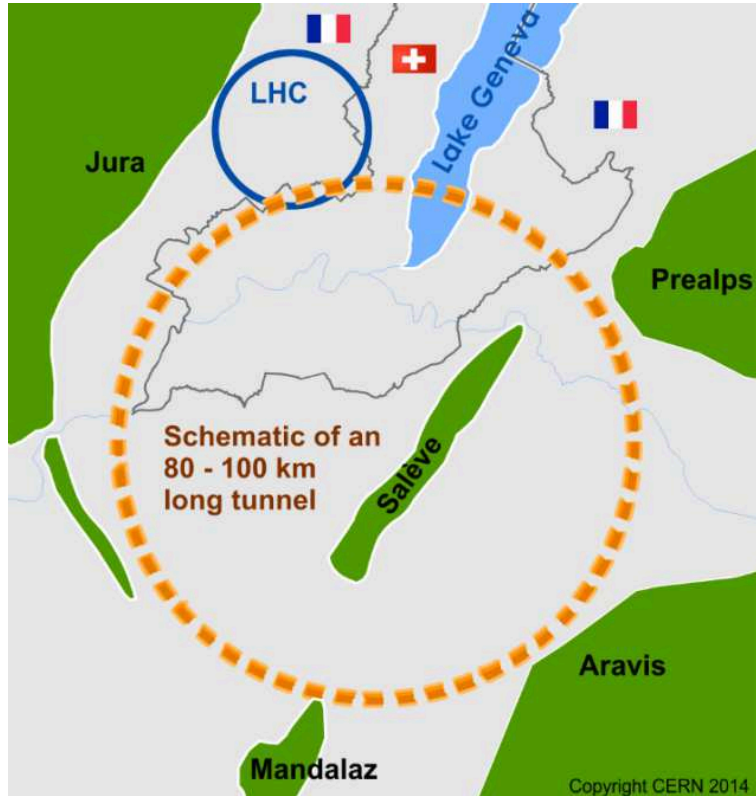
Figure 1.2: Schematic of a possible site for the FCC tunnel in the Geneva area. [12]

for momentum collimation (section F) and for the radio frequency (RF) cavities used for acceleration (section H). All short straight sections, including the IRs, have a length of 1.4 km. Furthermore, two long straight sections with 2.8 km length are foreseen for betatron collimation (section J) and extraction and beam dump (section D). The high luminosity IRs are connected to the adjacent short straight sections by short arc sections of 3.2 km length while the other straight sections are connected by long arcs of 16 km. Lastly, all straight sections are surrounded by dispersion suppressors of 0.4 km length. They are matching the large dispersion of the arcs to the usually dispersion free straight sections.

In Table 1.1 key parameters of FCC-hh are compared to those of the LHC and HL-LHC. FCC-hh features two parameter sets: a baseline option with a luminosity of $5 \times 10^{34}\,\mathrm{cm}^{-2}\mathrm{s}^{-1}$ and $250\,\mathrm{fb}^{-1}$ average integrated luminosity per year as well as the more ambitious so-called "ultimate" option increasing the peak luminosity up to a value of $30 \times 10^{34}\,\mathrm{cm}^{-2}\mathrm{s}^{-1}$ with $1000\,\mathrm{fb}^{-1}$ per year on average, including long maintenance shutdown periods. The current operational scenario foresees 10 years of operation using the baseline parameters and 15 years of "ultimate" operation, reaching a total integrated luminosity of $17\,500\,\mathrm{fb}^{-1}$ [15]. The major challenges for the machine design of FCC-hh are:

- The development of 16 T dipole magnets based on $\mathrm{Nb_3Sn}$ technology that can be produced with high precision on a large scale

- Protection of the cold, superconducting magnets from the synchrotron radiation
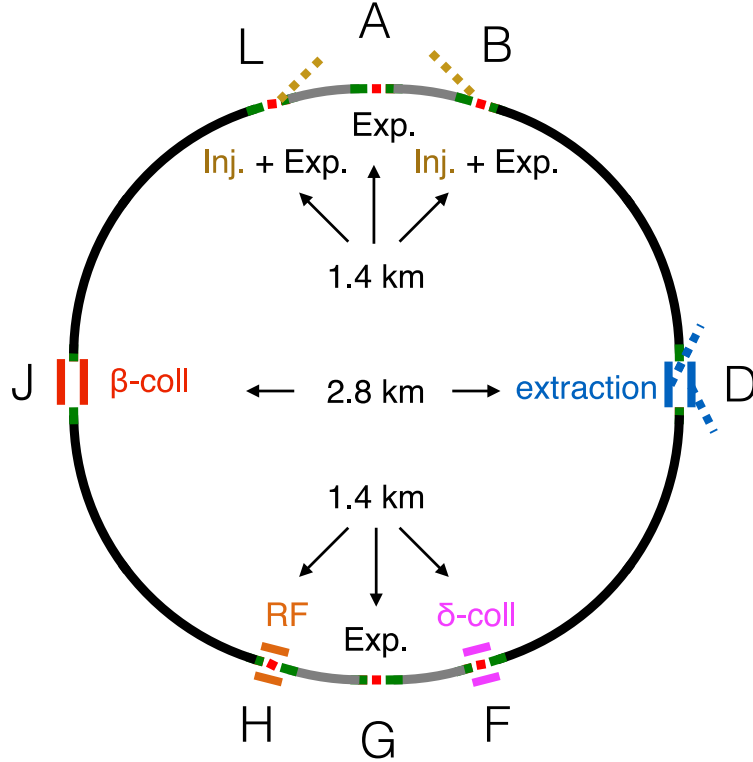
Figure 1.3: Schematic layout of FCC-hh. The straight sections are illustrated in red and blue and identified by a letter. Long arcs are in black, short arcs in gray. The dispersion suppressors are shown in green [14].

Table 1.1: Key parameters of FCC-hh compared to LHC and HL-LHC [15].

	LHC	HL-LHC	FCC-hh Baseline	"Ultimate"
Center-of-mass energy [TeV]	14	14	100	
Injection energy [TeV]	0.45	0.45	3.3	
Ring circumference [km]	26.7	26.7	97.75	
Arc dipole field [T]	8.33	8.33	16	
Number of IPs	2+2	2+2	2+2	
Number of bunches per beam n_b	2808	2748	10600 (53000)	
Beam current [A]	0.58	1.11	0.5	
Peak luminosity/IP [10^{34} cm^{-2}s^{-1}]	1	5	5	30
Events/crossing	27	135	170	1020 (204)
Stored beam energy [GJ]	0.4	0.7	8.4	
Synchrotron power per beam [MW]	0.0036	0.0073	2.4	
Arc synchrotron radiation [W/m/beam]	0.18	0.35	28.4	
IP beta function β^* [m]	0.4	0.15	1.1	0.3
Bunch spacing [ns]	25	25	25 (5)	
Initial norm. rms emittance [μm]	3.75	2.5	2.2 (0.45)	
Initial bunch population N_b[10^{11}]	1.15	2.2	1.0 (0.2)	
Transv. emittance damping time [h]	25.8	25.8	1.1	

- An interaction region design that can provide the high peak luminosity and survive the high energy deposition from collision debris

- An injector complex with a short turn-around time (i.e. the time between a beam dump and begin of collisions with the new beam) will significantly impact the average luminosity production

- Machine protection and beam dump design at 8.4 MJ stored beam energy

For the detector design the pile-up for the "ultimate" parameter represents a real challenge in terms of vertex finding. New methods, e.g. using timing to separate vertices or sensors in the beam pipe, will be required to cope with more than 1000 events per bunch crossing. A work-around on the accelerator side is a reduced bunch spacing of 5 ns. The respective parameters for this option are included in brackets in Table 1.1 and feature a reduced bunch charge to keep the beam current the same. With only 200 events per crossing, the pile-up would be in the same order as foreseen for the HL-LHC and considered possible to handle. The 5 ns option has a challenging normalized emittance goal of 0.45 μm. It is therefore important to explore the possibility to achieve significantly smaller β^* than specified for the "ultimate" parameter option, in order to have a leverage to keep the goal for the integrated luminosity realistic, should the normalized emittance goal not be met.

Challenges for FCC-hh interaction region design   This thesis focuses on the design of the high luminosity interaction regions for FCC-hh. These interaction regions will require a strongly focused beam but at the same time they need to provide enough space (most significantly L^*) for the detectors. Consequently, they will feature the largest β functions in the whole machine, along with all the associated challenges like mechanical aperture constraints, chromaticity and dynamic aperture.

In the scope of this work, the same quadrupole magnet technology as in the HL-LHC is assumed, while the beam energy increases by a factor of ≈ 7.6, so the limitations on performance arising from this scaling need to be evaluated. The center-of-mass energy of 100 TeV is unprecedented and new challenges coming with it must be identified and addressed. One of the expected challenges is the radiation load in the final focus system coming from collision debris from the interaction point. The high luminosity upgrade of the LHC already requires dedicated shielding inside the final focus magnets to cope with the increased radiation load. For FCC-hh the picture will become even worse as the radiation load increases with:

- Center-of-mass energy E_{cm}

- Proton-Proton inelastic cross section $\sigma_{\mathrm{inel,pp}}$

- Peak Luminosity

- Integrated Luminosity

The corresponding values are listed in Table 1.2 for LHC, HL-LHC and FCC-hh. The instantaneous luminosity drives the peak power density in the superconducting magnets, possibly causing quenches, but also the heat load. The peak power density must be well below the quench limit, otherwise stable operation is impossible. The total power at the Interaction Point (IP) is expected to be 43 kW with baseline

Table 1.2: Parameters contributing to the radiation load

	LHC	HL-LHC		FCC-hh	
		baseline	ultimate	baseline	ultimate
E_{cm} [TeV]	14	14		100	
$\sigma_{\mathrm{inel,pp}}$ [mb]	81 ± 3[1]	81 ± 3[1]		108[2]	
Peak luminosity [10^{34} cm^{-2}s^{-1}]	1	5	7.5	5	30
Integrated luminosity [fb^{-1}]	300	3000	4000	17500[3]	

[1] Based on TOTEM measurements at $E_{\mathrm{cm}} = 7$ TeV and extrapolation using various models [16]   [2] Value taken from [17]   [3] Assuming 10 years of operation with baseline parameters followed by 15 years with ultimate parameters [15]

parameters, compared to 1 kW for LHC and 4.76 kW for HL-LHC. For ultimate parameters the power will increase to 260 kW. While the resulting power densities in the superconducting coils of the final focus system will depend on the geometry, magnet strengths and crossing angles, we can expect them to scale in the same order of magnitude if no additional mitigation measures are taken. The integrated luminosity on the other hand will determine long term radiation damage, mainly due to the degradation of insulator material and epoxy resin used to impregnate coils, as well as the activation of the magnets. Again a rough estimate from the integrated luminosity goal suggests an increase of the peak doses by two to three orders of magnitude.

Starting from general concepts of accelerator physics in Chapter 2, scaling strategies for the the LHC and HL-LHC interaction region will be derived in Chapter 3 in order to use the existing lattices at higher energies for FCC-hh. The resulting lattices, identified by their respective L^*, are presented in Chapter 4 where also first studies of collision debris identify radiation protection as a main driver for the IR design. Furthermore, a general IR design strategy to combine radiation protection with high luminosity is deduced. In an effort to reduce the radiation load on the final focus system further, a novel mitigation method, named Q1 split, is derived and studied in Chapter 5. In Chapter 6 the approach for the integration of the interaction region into the full ring lattice is presented, together with the resulting optics and the limitations. Lastly, first studies of the dynamic aperture are shown in Chapter 7 in an effort to show the feasibility of the interaction region lattice developed in this thesis.

Chapter 2

Concepts of accelerator physics

This chapter introduces the basic principles of accelerator physics relevant to this thesis. More details can be found in standard text books, e.g. [18].

2.1 Coordinate system

The trajectory in an accelerator taken by a particle with design momentum is called the design orbit. To describe the motion of particles with small deviations from the design momentum or the design orbit, an orthogonal right-handed coordinate system (s, x, y) moving along the orbit and following the longitudinal particle motion as shown in Fig. 2.1 is introduced. For every longitudinal position along the orbit s, particles have the perpendicular horizontal and vertical offsets $x(s)$ and $y(s)$. In regions with a local bending radius R, the coordinate system is rotated accordingly, so the s-axis is always tangential to the design orbit. In a circular accelerator the orbit is periodic, meaning the ideal particle will follow the same trajectory every turn.
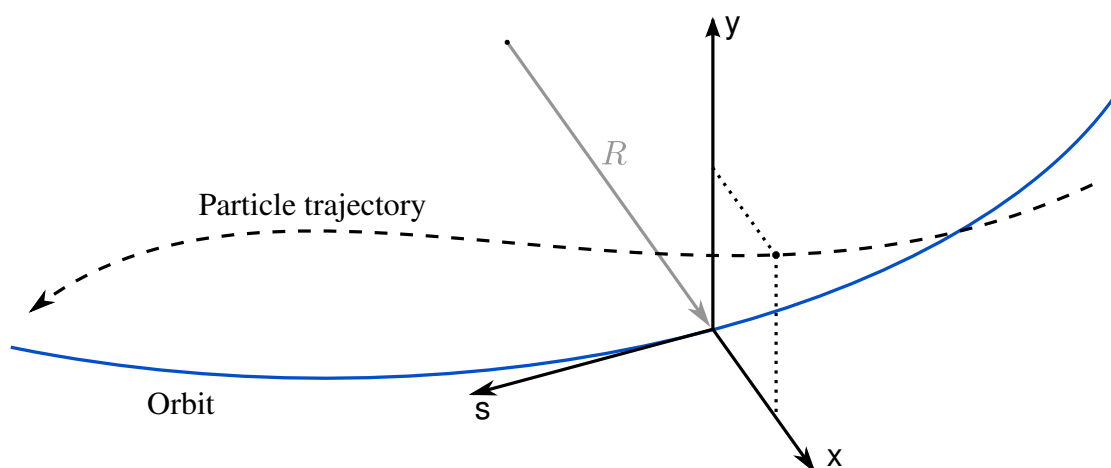

Figure 2.1: Coordinate system used for accelerators. The trajectory of a particle is described as an offset $(x(s), y(s))$ from the reference orbit at the longitudinal position s.

2.2 Lorentz force

In order to accelerate and steer charged particle in an accelerator, electric ($\mathbf{E}$) and magnetic ($\mathbf{B}$) fields are used. They act on a particle with charge q and velocity $\mathbf{v}$ via the Lorentz force

$$\mathbf{F} = q \cdot (\mathbf{E} + \mathbf{v} \times \mathbf{B}) \tag{2.1}$$

As the direction of magnetic part of the Lorentz force is always perpendicular to the particle motion, it can deflect the particle but not accelerate it. Thus electric fields in so-called Radio Frequency (RF) cavities are used for acceleration. On the other hand, the multiplication with the velocity increases the force of a magnetic field with higher energies. At relativistic energies with $v \approx c$, a magnetic field of $1\,\mathrm{T}$ exerts the same force as an electric field of $3 \times 10^8\,\mathrm{Vm^{-1}}$. While $1\,\mathrm{T}$ can be easily reached with normal conducting magnets, an electric field of $3 \times 10^8\,\mathrm{Vm^{-1}}$ is far beyond technical possibilities, making magnets the means of choice for any kind of deflection.

Ideally, particles should only have a small offset x from the design orbit. Thus it is possible to expand the magnetic field around the ideal orbit $x = 0$:

$$B_y = B_{y0} + \frac{\mathrm{d}B_y}{\mathrm{d}x}x + \frac{1}{2!}\frac{\mathrm{d}^2 B_y}{\mathrm{d}x^2}x^2 + \frac{1}{3!}\frac{\mathrm{d}^3 B_y}{\mathrm{d}x^3}x^3 + ... \tag{2.2}$$

This expansion assumes the one-dimensional case without a vertical offset, $y = 0$. The deflection of a moving particle is obtained by multiplying with the beam rigidity e/p, which gives

$$
\begin{aligned}
\frac{e}{p}B_y \quad &= \quad \frac{e}{p}B_{y0} \quad + \quad \frac{e}{p}\frac{\mathrm{d}B_y}{\mathrm{d}x}x \quad + \quad \frac{e}{p}\frac{1}{2!}\frac{\mathrm{d}^2 B_y}{\mathrm{d}x^2}x^2 \quad + \quad \frac{e}{p}\frac{1}{3!}\frac{\mathrm{d}^3 B_y}{\mathrm{d}x^3}x^3 \quad + \quad ... \\
&= \quad \frac{1}{R} \quad + \quad kx \quad + \quad \frac{1}{2!}mx^2 \quad + \quad \frac{1}{3!}ox^3 \quad + \quad ... \\
&\quad\quad \text{Dipole} \quad\quad \text{Quadrupole} \quad\quad \text{Sextupole} \quad\quad \text{Octupole} \quad\quad ...
\end{aligned}
\tag{2.3}
$$

These elements can be identified as dipolar ($\frac{1}{R}$), quadrupolar (kx), sextupolar ($\frac{1}{2!}mx^2$), etc. components. Usually, only the two lowest components define the optics of an accelerator, with dipoles used for beam steering and quadrupole for beam focusing, while the higher multipoles are used for corrections, e.g sextupoles for chromaticity correction and octupoles for Landau damping. As a result of Maxwell's equations a quadrupole is focusing only in one plane and defocusing in the perpendicular plane. To achieve a net focusing effect in both planes, a combination of at least two quadrupoles is required. This leads to the so-called FODO structure with alternating focusing (F) and defocusing (D) quadrupoles separated by non-focusing elements (O) like drifts.

2.3 Equation of motion

The transverse motion of a particle in a linear lattice can be described by the differential equation

$$x'' + \left(\frac{1}{R^2} - k\right)x = \frac{1}{R}\frac{\Delta p}{p} \tag{2.4}$$

and similar in y. Here the prime indicates the derivative $\frac{\mathrm{d}}{\mathrm{d}s}$. k is the normalized quadrupole strength as defined in Eq. (2.3) while the term $\frac{1}{R^2}$ on the left hand side of Eq. (2.4) is connected to the geometric focusing property of dipole magnets, called weak focusing as opposed to the strong focusing quadrupoles.

In the case of on-momentum particles ($\frac{\Delta p}{p} = 0$), neglecting weak focusing ($\frac{1}{R} = 0$), Eq. (2.4) reduces to

$$x'' - kx = 0. \tag{2.5}$$

Assuming a constant focusing quadrupole strength $k = \text{const}$, $k < 0$, this is the differential equation of a harmonic oscillator and can be solved analytically by

$$x(s) = x_0 \cos \sqrt{|k|}s + \frac{x_0'}{\sqrt{|k|}} \sin \sqrt{|k|}s \tag{2.6}$$

$$x'(s) = -x_0 \sqrt{|k|} \sin \sqrt{|k|}s + x_0' \cos \sqrt{|k|}s \tag{2.7}$$

with the initial conditions $x_0 = x(0)$ and $x_0' = x'(0)$. It is possible to express Eqs. 2.6 and 2.7 using vectors.

$$\begin{pmatrix} x(s) \\ x'(s) \end{pmatrix} = M_{\mathrm{QF}} \cdot \begin{pmatrix} x(s) \\ x'(s) \end{pmatrix} \quad \text{with} \quad M_{\mathrm{QF}} = \begin{pmatrix} \cos \sqrt{|k|}s & \frac{1}{\sqrt{|k|}} \sin \sqrt{|k|}s \\ -\sqrt{|k|} \sin \sqrt{|k|}s & \cos \sqrt{|k|}s \end{pmatrix} \tag{2.8}$$

In this notation, M_{QF} is called the transfer matrix of the focusing quadrupole. Likewise, it is possible to obtain the transfer matrices of all other linear elements in an accelerator, i.e. defocusing quadrupoles, dipoles and drift spaces. Using the same approach as before with $k > 0$, the transfer matrix of a defocusing quadrupole is

$$M_{\mathrm{QD}} = \begin{pmatrix} \cosh \sqrt{k}s & \frac{1}{\sqrt{k}} \sinh \sqrt{k}s \\ \sqrt{k} \sinh \sqrt{k}s & \cosh \sqrt{k}s \end{pmatrix} \tag{2.9}$$

and the transfer matrix of a drift space with length L and $k = 0$ can simply be obtained by integrating Eq. (2.5) to get

$$x(L) = x_0 + x_0' \cdot L \tag{2.10}$$

$$x'(L) = x_0' \tag{2.11}$$

with the transfer matrix

$$M_{\mathrm{drift}} = \begin{pmatrix} 1 & L \\ 0 & 1 \end{pmatrix}. \tag{2.12}$$

When weak focusing is neglected, dipoles behave like drift spaces. The transfer matrix of a sequence of these elements is then obtained by the product of the transfer matrices of the elements, e.g.

$$M_{\mathrm{FODO}} = M_{\mathrm{drift}} \cdot M_{\mathrm{QD}} \cdot M_{\mathrm{drift}} \cdot M_{\mathrm{QF}} \tag{2.13}$$

for a FODO cell.

When describing a circular accelerator, the particle will travel through the same magnet structure multiple times. In this case the position dependent quadrupole strength $k(s)$ becomes periodic $k(s) = k(s + L_{\mathrm{ring}})$, resulting in Hill's equation of motion

$$x'' - k(s)x = 0. \tag{2.14}$$

This differential equation can be solved by the ansatz

$$x(s) = A \cdot u(s) \cos\left(\Psi(s) + \phi_0\right), \tag{2.15}$$

where $A \cdot u(s)$ is a position dependent amplitude function and $\Psi(s)$ the phase of an oscillation around the design orbit. It is now worth to derive the evolution of the amplitude. This can be done by differentiating Eq. (2.15) and inserting the result into Eq. (2.14)

$$A\left(u'' - u'\Psi'^2 - k(s)u\right)\cos\left(\Psi(s) + \phi_0\right) - A\left(2u'\Psi' + u\Psi''\right)\sin\left(\Psi(s) + \phi_0\right) = 0 \tag{2.16}$$

which can only be solved generally for

$$u'' - u'\Psi'^2 - k(s)u = 0 \tag{2.17}$$

$$2u'\Psi' + u\Psi'' = 0 \tag{2.18}$$

By separating the u and Ψ terms in Eq. (2.18) and integrating logarithmically, we get

$$\Psi(s) = \int\limits_0^s \frac{1}{u^2(\tilde{s})} \mathrm{d}\tilde{s}. \tag{2.19}$$

Inserting this into Eq. (2.17) results in

$$u''(s) - \frac{1}{u^3(s)} - k(s)u(s) = 0 \tag{2.20}$$

Equation 2.20 describes the behaviour of the amplitude of the particle oscillation around the design orbit and cannot be solved analytically. Instead, it is usually evaluated numerically.

2.4   Emittance and phase space

By introducing the beta function $\beta(s) = u^2(s)$ and replacing A in Eq. (2.15) with the square root of the emittance $\sqrt{\epsilon}$ we get the solution of the Hill's equation

$$x(s) = \sqrt{\epsilon\beta(s)}\cos\left(\Psi(s) + \phi_0\right) \tag{2.21}$$

$$x'(s) = \sqrt{\frac{\epsilon}{\beta(s)}}\left(\alpha(s)\cos\left(\Psi(s) + \phi_0\right) + \sin\left(\Psi(s) + \phi_0\right)\right) \tag{2.22}$$

with $\alpha = -\frac{\beta'(s)}{2}$. The amplitude function $\sqrt{\epsilon\beta(s)}$ is an envelope of all the trajectories a particle can follow over various turns.

Equation (2.21) can be solved for the cosine term and substituted into Eq. (2.22). Solving the result for the remaining sine term and using the relation $\sin^2\Phi + \cos^2\Phi = 1$ yields the equation

$$\gamma(s)x^2(s) + 2\alpha(s)x(s)x'(s) + \beta(s)x'^2(s) = \epsilon \tag{2.23}$$

with $\gamma = \frac{1+\alpha^2(s)}{\beta(s)}$. This equation describes an ellipse in the phase space (x, x') with the area $\pi \cdot \epsilon$. According to Liouville's theorem, the phase space volume is constant
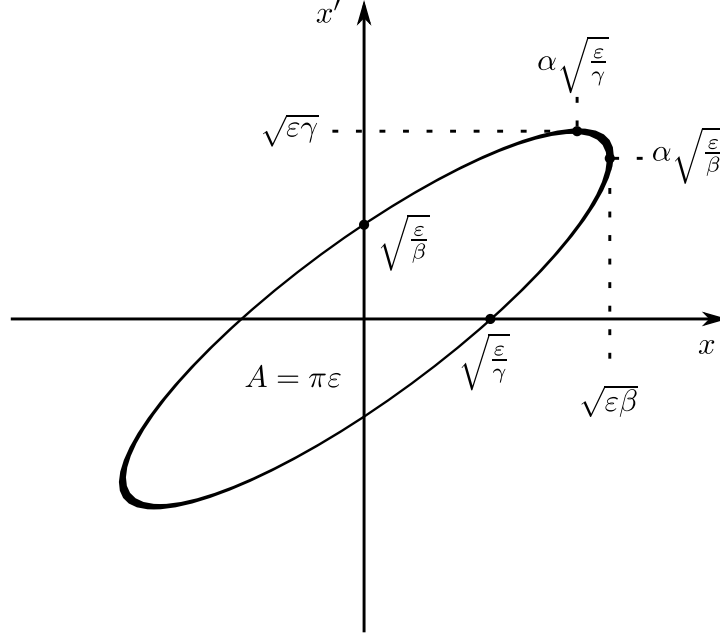
Figure 2.2: Phase space diagram of a particle motion in $x - x'$ space.

under conservative forces. This means the area of the phase space ellipse and hence the emittance are invariants of the particle motion. The shape and orientation of the ellipse in the phase space are functions of the focusing properties of the lattice and determined by the so-called Twiss parameters β, α and γ as shown in Fig. 2.2. While the emittance is a property of a single particle, a beam emittance can be defined e.g. by

$$\epsilon_{\text{beam}} = \frac{\sigma_x^2}{\beta} \tag{2.24}$$

with σ_x the horizontal rms beam size. In the following ϵ will always refer to the beam emittance. Hence $\sqrt{\epsilon\beta(s)}$ describes the rms beam size at the position s. An important consequence of the invariance of the emittance is that a strongly focused beam (i.e. small σ_x) has a large divergence (large $\sigma_{x'}$).

With a constant emittance, we can use Eq. (2.23) to determine the evolution of the Twiss parameters β, α and γ, as the evolution of $x(s)$ and $x'(s)$ is given by the transfer matrix M (see Eq. 2.8). The result can also be written in matrix notation.

$$\begin{pmatrix} \beta \\ \alpha \\ \gamma \end{pmatrix} = \begin{pmatrix} m_{11}^2 & -2m_{11}m_{12} & m_{12}^2 \\ -m_{11}m_{21} & m_{11}m_{22} + m_{12}m_{21} & -m_{22}m_{12} \\ m_{21}^2 & -2m_{22}m_{21} & m_{22}^2 \end{pmatrix} \cdot \begin{pmatrix} \beta_0 \\ \alpha_0 \\ \gamma_0 \end{pmatrix} \tag{2.25}$$

where $m_{i,j}$ are the matrix elements of the 2D transfer matrix. Conversely, it is also possible to determine the transfer matrix between two positions if the Twiss parameters and the phase advance are known. In that case, M is

$$M = \begin{pmatrix} \sqrt{\frac{\beta}{\beta_0}}\left(\cos\Psi + \alpha_0\sin\Psi\right) & \sqrt{\beta\beta_0}\sin\Psi \\ \frac{(\alpha_0-\alpha)\cos\Psi-(1+\alpha_0\alpha)\sin\Psi}{\sqrt{\beta\beta_0}} & \sqrt{\frac{\beta_0}{\beta}}\left(\cos\Psi - \alpha\sin\Psi\right) \end{pmatrix}. \tag{2.26}$$

An acceleration parallel to the design orbit decreases the emittance as laid out
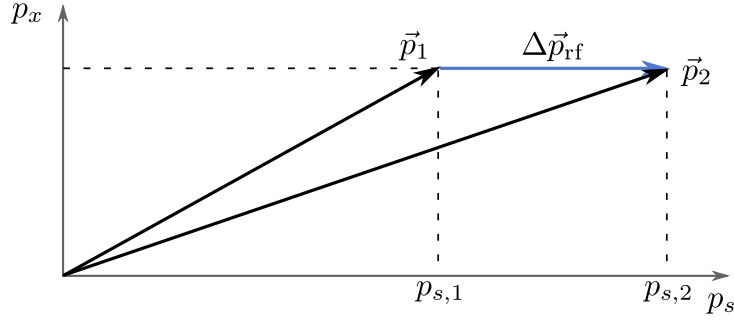
Figure 2.3: Decrease of the emittance due to acceleration. With $x' = p_x/p_s$ a forward acceleration $\Delta\vec{p}_{\rm rf}$ increases only p_s and decreases x' without any direct effect on x.

in Fig. 2.3. To take this into account, the normalized emittance is introduced

$$\epsilon_{\rm n} = \beta_{\rm rel}\gamma_{\rm L}\epsilon \tag{2.27}$$

with $\beta_{\rm rel} = v/c$ and $\gamma_{\rm L}$ the relativistic Lorentz factor. For high particle energies where $\beta_{\rm rel} \approx 1$ the normalized emittance is approximated by $\epsilon_{\rm n} \approx \gamma_{\rm L}\epsilon$

2.5 Tune and resonances

With the introduction of the beta function $\beta(s) = u^2(s)$, the phase $\Psi(s)$ of the particle motion in Eq. (2.19) becomes

$$\Psi(s) = \int_0^s \frac{1}{\beta(\tilde{s})}\mathrm{d}\tilde{s} \tag{2.28}$$

The difference of the phases $\Psi(s)$ at two points $s = s_1$ and $s = s_2$ is called the phase advance

$$\mu = \Psi(s_2) - \Psi(s_1) \tag{2.29}$$

The phase advance of a full revolution in a circular accelerator divided by 2π, is called the tune Q and gives the number of transverse oscillations per turn.

$$Q = \frac{1}{2\pi}\int_0^L \frac{\mathrm{d}s}{\beta(s)} = \frac{1}{2\pi}\oint \frac{\mathrm{d}s}{\beta(s)} \tag{2.30}$$

As there is always particle motion in both transverse planes x and y, an accelerator has a pair of tunes Q_x and Q_y called the working point. It is important to note that small imperfections in the machine can cause resonances when encountered by particles repeatedly at the same phase. To avoid beam instabilities, the tune must thus be chosen to avoid resonances
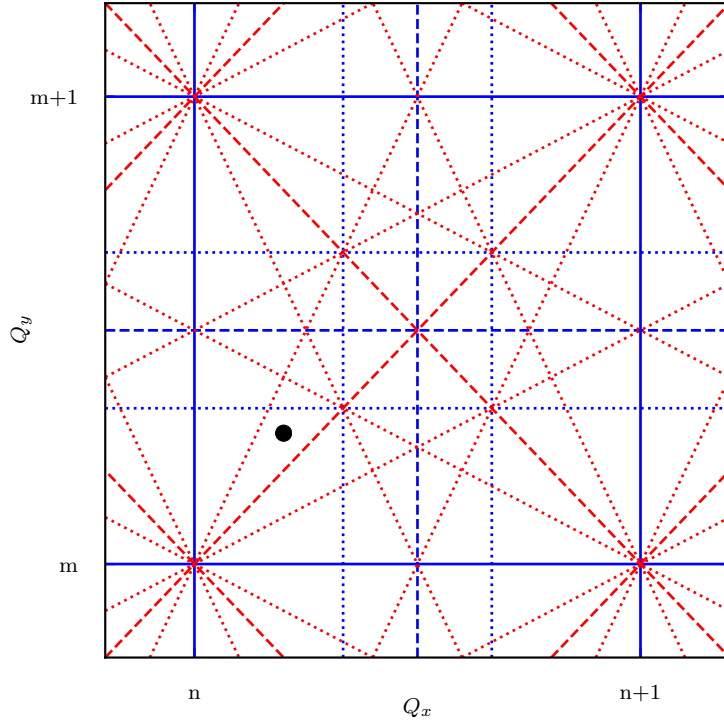
$$m \cdot Q_{x,y} = p \tag{2.31}$$

Figure 2.4: Tune diagram with single plane resonances (blue) and coupling resonances (red) up to the third order. A possible choice for the working point is marked by the black dot.

with m and p being integers. In the presence of coupling, i.e. when horizontal and vertical particle motion are not independent, additional resonance occur when the horizontal and vertical tunes satisfy the condition

$$m \cdot Q_x + n \cdot Q_y = p \tag{2.32}$$

with m, n and p being integers. As particles must survive hundreds of thousands of turns in the machine, high order resonances can become relevant, so the working point must be chosen carefully. Figure 2.4 illustrates a possible working point avoiding resonances up to the third order.

2.6 Dispersion function

Previously, the equation of motion Eq. (2.4) was solved for the special case of particles with design energy. To describe the behaviour of off-momentum particles, the trajectory $D(s)$ for particles with $\frac{\Delta p}{p} = 1$ is introduced. $D(s)$ is called the dispersion function. Since the right hand side of Eq. (2.4)

$$x'' + \left(\frac{1}{R^2} - k \right) x = \frac{1}{R} \frac{\Delta p}{p}$$

is only non-zero in dipoles ($1/R \neq 0$), the quadrupole term is ignored for now ($k = 0$).

$$D''(s) + \frac{1}{R^2} D(s) = \frac{1}{R} \tag{2.33}$$

The homogeneous part of this differential equation can be solved the same way Eq. (2.14) was solved. Additionally a particular solution of the inhomogeneous equation is required. As the right hand side of Eq. (2.33) is constant, $D_{\text{inhom}} = R$ is an obvious solution. Inserting the initial conditions $D(0) = D_0$ and $D'(0) = D'_0$ yields

$$D(s) = D_0 \cos \frac{s}{R} + D'_0 R \sin \frac{s}{R} + R \left(1 - \cos \frac{s}{R} \right) \tag{2.34}$$

$$D'(s) = -\frac{D_0}{R} \sin \frac{s}{R} + D'_0 \cos \frac{s}{R} + \sin \frac{s}{R}. \tag{2.35}$$

A particle with momentum deviation $\frac{\Delta p}{p}$ has the trajectory

$$x_{\text{tot}}(s) = x(s) + D(s) \frac{\Delta p}{p} \tag{2.36}$$

where $x(s)$ is the betatron motion (see Eq. (2.21)) around the dispersion orbit $D(s)\frac{\Delta p}{p}$. In other elements where $(1/R = 0)$ Eq. (2.4) does not differ from the equation of motion of on-momentum particles Eq. (2.5) and the dispersion orbit transforms like a normal transverse offset. This is due to the fact that Eq. (2.4) is a linear approximation of the particle motion for small x and small $\frac{\Delta p}{p}$. The first order chromatic effects of quadrupoles are described in the next section.

2.7 Chromaticity and sextupoles

So far, the focusing of quadrupoles has been treated as constant. However, similar to the dispersion in dipoles, off-momentum particles will be affected differently. The momentum dependent focusing is given by

$$k(p) = \frac{q}{p} \cdot g = \frac{q}{p_0 + \Delta p} \cdot g \tag{2.37}$$

with g the quadrupole gradient $\mathrm{d}B_y/\mathrm{d}x$. The Taylor expansion of Eq. (2.37) to the first order gives us

$$k(p) \approx \frac{q}{p_0} \left(1 - \frac{\Delta p}{p_0} \right) \cdot g = k_0 - \Delta k \tag{2.38}$$

with $\Delta k = \frac{\Delta p}{p} k$. This momentum dependent quadrupole error Δk causes a tune shift of

$$\mathrm{d}Q = \frac{\Delta p}{p} \frac{1}{4\pi} k_0 \beta(s) \mathrm{d}s. \tag{2.39}$$

The total tune shift ΔQ is obtained by integrating over the whole ring in order to include the effect of all quadrupoles. The related quantity

$$\xi = \frac{\Delta Q}{\Delta p/p} = \frac{1}{4\pi} \oint k(s) \beta(s) \, \mathrm{d}s \tag{2.40}$$

is called the natural chromaticity. From this equation, we can see that the chromaticity of an accelerator is usually negative as the largest β occur in focusing quadrupoles (negative k) whereas the defocusing quadrupoles (positive k) create local minima in the β functions. As the chromatic contributions of the different quadrupoles do not cancel each other, a dedicated correction is usually necessary.
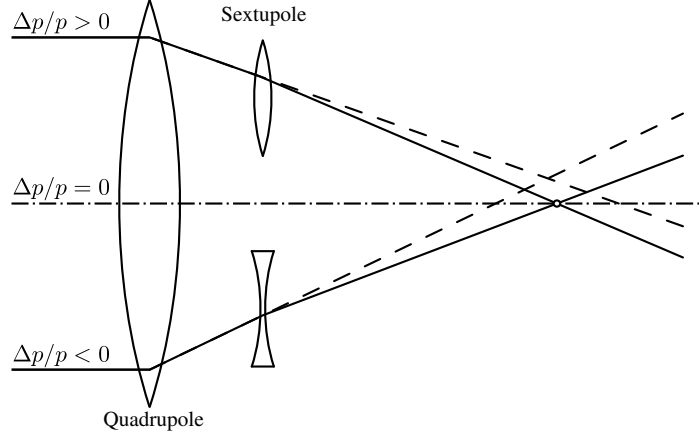
Figure 2.5: Chromaticity correction with a sextupole in a dispersive section.

To correct the chromaticity, the momentum dependent focusing must be compensated. For this purpose a sextupole is placed at a position with a momentum dependent orbit excursion (i.e. dispersion)

$$x_\mathrm{D} = D(s)\frac{\Delta p}{p}. \tag{2.41}$$

The field of a sextupole is

$$\begin{aligned} B_x &= g' \cdot x \cdot y \\ B_y &= \frac{1}{2}g' \cdot \left(x^2 - y^2\right) \end{aligned} \tag{2.42}$$

with $g' = \frac{\mathrm{d}^2 B_y}{\mathrm{d}x^2}$. From this, the gradient of the sextupole can be obtained.

$$g(x,y) = \frac{\partial B_y}{\partial x} = \frac{\partial B_x}{\partial y} = g' \cdot x. \tag{2.43}$$

Thus the sextupole acts as a focusing element with the focusing strength depending on the transverse offset

$$\Delta k_\mathrm{sext} = \frac{e}{p}g(x,y) = \frac{e}{p}g'x = mx. \tag{2.44}$$

Since the sextupole is placed in a dispersive section, the transverse offset $x = x_\mathrm{D}$ is momentum dependent, resulting in the momentum dependent focusing term

$$\Delta k_\mathrm{sext} = mD(s)\frac{\Delta p}{p} \tag{2.45}$$

that can be used for chromaticity correction as outlined in Fig. 2.5. The total chromaticity is then given by

$$\xi_\mathrm{tot} = \frac{1}{4\pi} \oint \left[m(s)D(s) + k(s)\right]\beta(s)\,\mathrm{d}s. \tag{2.46}$$

15

2.8 Feed down effects

Feed down effects occur when the beam travels through a multipole with a transverse offset from the magnetic axis, be it due to magnet misalignments or orbit bumps, e.g. for the crossing angles. According to Eq. (2.2) an ideal $2n$-pole has a field of the form

$$B_y = c_n x^n \tag{2.47}$$

with c_n given by the magnet strength. If the beam has a transverse offset x_off the field becomes a polynomial in x

$$B_y = c_n \left(x - x_\text{off}\right)^n = c_n x^n + c_{n-1} x^{n-1} + c_{n-2} x^{n-2} + ... \tag{2.48}$$

with

$$c_{n-1} = n c_n x_\text{off} \tag{2.49}$$

$$c_{n-2} = \frac{(n-1)\,n}{2} c_n x_\text{off}^2 \tag{2.50}$$

$$c_{n-a} = \frac{n!}{a!(n-a)!} c_n x_\text{off}^a \tag{2.51}$$

Consequently, the beam experiences all lower order field components, e.g. an off-center sextupole acts like a combination of a centered sextupole, a centered quadrupole and a dipole with the associated consequences for β functions, tune and closed orbit. The chromaticity correction is an example of the intentional use of the feed down effect from a sextupole. However, feed down effects from magnet misalignments or higher order field errors distort the beam optics and require correction.

2.9 Coupling

In an ideal lattice, the transverse motion can be described by the 4×4 block diagonal matrix M_4D as

$$\begin{pmatrix} x \\ x' \\ y \\ y' \end{pmatrix} = \begin{pmatrix} m_{x11} & m_{x12} & 0 & 0 \\ m_{x21} & m_{x22} & 0 & 0 \\ 0 & 0 & m_{y11} & m_{y12} \\ 0 & 0 & m_{y21} & m_{y22} \end{pmatrix} \cdot \begin{pmatrix} x_0 \\ x_0' \\ y_0 \\ y_0' \end{pmatrix} = M_\text{4D} \cdot \begin{pmatrix} x_0 \\ x_0' \\ y_0 \\ y_0' \end{pmatrix} \tag{2.52}$$

with m_{xij} and m_{yij} the i, j element of the 2×2 transfer matrices in the horizontal and vertical planes. In the presence of solenoid fields or skew quadrupole components, introduced e.g. by angular misalignments of quadrupoles or by orbit excursions in higher order multipoles, the horizontal and vertical motion are coupled and the transverse motion is described by

$$M_\text{4D} = \begin{pmatrix} M_x & p \\ q & M_y \end{pmatrix} \tag{2.53}$$

with non-zero 2×2 matrices p and q. Coupling causes resonances as discussed earlier. Unlike other resonances, the difference resonance $(m \cdot Q_x - n \cdot Q_y = p)$ does not cause beam loss but causes the horizontal tune Q_x and vertical tune Q_y to exchange values.

The optics program MAD-X used in this thesis applies the Edwards-Teng parameterization of coupling [19], using the coefficients of the R matrix that satisfies

$$VM_{\text{4D}}V^{-1} = \begin{pmatrix} A & 0 \\ 0 & B \end{pmatrix} \qquad (2.54)$$

with

$$V = \frac{1}{\sqrt{1 + \det R}} \begin{pmatrix} I & R \\ -R & I \end{pmatrix}. \qquad (2.55)$$

In this notation, the horizontal and vertical motion are uncoupled if all elements of R are zero.

2.10   Beam stay clear

Various forms of non-linear particle dynamics can lead to chaotic behaviour of particles which causes an increasing transverse oscillation amplitude causing a particle beam to continuously lose particles. To protect the cold, superconducting magnets from quenches induced by energy deposition from these particles, hadron colliders like the LHC feature collimation systems. Primary collimator jaws create an aperture bottleneck in order scrape off unstable particles with large amplitudes. Most of the protons hitting the collimators are not absorbed but are either scattered elastically or create hadronic showers. These secondary particles are then absorbed by secondary collimators located behind the primary jaws and featuring a slightly larger aperture. Finally tertiary collimators are used locally, e.g. at aperture bottlenecks like the final focus system, to protect magnets from remaining secondary or tertiary particles. This defines the collimation hierarchy, requiring the magnets to have larger apertures than the tertiary collimators protecting them.

However, since the particle beam, as well as the halo of secondary particles, is constantly focused and defocused, the absolute aperture is not the best way to describe aperture bottlenecks. Instead, the local aperture is expressed in terms of beam size to define the so-called beam stay clear (BSC). The exact definition of the beam stay clear is illustrated in Fig. 2.6. The center of the beam is displaced from the closed orbit, i.e. the design orbit plus the orbit excursion from closed orbit bumps, by the orbit uncertainty. Around this center, the largest beam ellipse that fits into the aperture is calculated. Of all the ellipses found for different displacements due to the orbit uncertainty, the smallest one is used to define the beam stay clear N_{bsc} in units of σ_{beam}. In the LHC a beam stay clear of $12\,\sigma$ is specified for the magnets in order to respect the collimation hierarchy. For FCC-hh, a beam stay clear between $12\,\sigma$ and $21\,\sigma$ is considered reasonable with the current baseline at $15.5\,\sigma$.
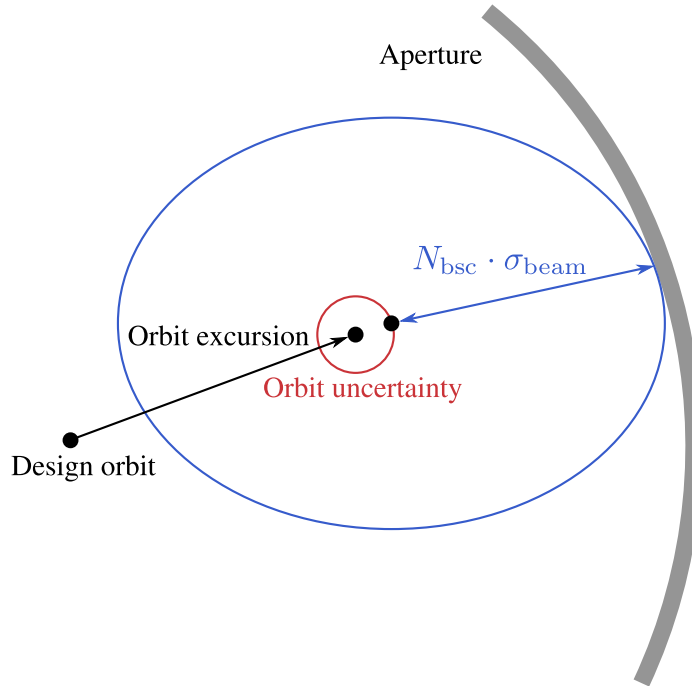
Figure 2.6: Calculation of the beam stay clear N_{bsc}.

2.11 Dynamic aperture

The description of transverse beam dynamics has so far been limited to linear elements like dipoles and quadrupoles. Higher order fields exert non-linear forces onto the particles with the result that the particle motion cannot be described anymore by harmonic oscillations around the design orbit. This is particularly a problem for particles with large amplitudes that can start chaotic behaviour. It is not possible to treat this problem analytically, instead a numerical method, the particle tracking, is used. Starting from initial coordinates, the particle trajectory is calculated element by element with the non-linear fields exerting amplitude dependent kicks. This is done for a large number of turns to infer the long term behaviour of the particle. In the LHC 10^5 to 10^6 turns are usually tracked to get reliable estimates of the dynamic aperture [20]. If the amplitude of the particle exceeds a certain value, it is considered lost. Scanning a range of initial coordinates with this tracking can define an effective aperture that separates the stable from the unstable particles, the Dynamic Aperture (DA).

2.12 Luminosity

The rate of events in a particle collider is given by

$$\frac{\mathrm{d}N}{\mathrm{d}t} = \sigma_{\mathrm{p}} \cdot \mathcal{L}. \tag{2.56}$$

Here, σ_{p} is the proton-proton cross section, a figure determined by the underlying physical processes of the collision. $\mathcal{L}$ is the luminosity, the figure-of-merit that

describes the collider performance. The total number of events is thus

$$N = \sigma_{\mathrm{p}} \int \mathcal{L} \mathrm{d}t = \sigma_{\mathrm{p}} \mathcal{L}_{\mathrm{int}} \tag{2.57}$$

with $\mathcal{L}_{\mathrm{int}}$ the integrated luminosity. For equal beams, i.e. $\sigma_{1x} = \sigma_{2x}$ and $\sigma_{1y} = \sigma_{2y}$ with Gaussian bunch profiles, the luminosity is

$$\mathcal{L} = \frac{n_{\mathrm{b}} N_{\mathrm{b}1} N_{\mathrm{b}2} f_{\mathrm{rev}}}{4\pi \sigma_x \sigma_y} \tag{2.58}$$

The revolution frequency f_{rev} as well as the number of bunches per beam n_{b} are mainly determined by the circumference of the collider. In the case of hadron colliders, the bunch populations of the colliding beams $N_{\mathrm{b}1}$ and $N_{\mathrm{b}2}$ are usually equal and limited by the first elements of the injector chain, the particle source and the following linear accelerator. For round beams with equal transverse beam sizes at the IP

$$\sigma_x^* = \sigma_y^* = \sqrt{\frac{\beta^* \epsilon_{\mathrm{n}}}{\gamma_{\mathrm{L}}}} \tag{2.59}$$

with β^* the β function at the IP we get

$$\mathcal{L} = \frac{n_{\mathrm{b}} N_{\mathrm{b}1} N_{\mathrm{b}2} f_{\mathrm{rev}} \gamma_{\mathrm{L}}}{4\pi \beta^* \epsilon_{\mathrm{n}}} \tag{2.60}$$

From the beam optics point of view, the only parameter for optimization in Eq. (2.60) is β^*. Subsequently, to maximize the luminosity β^* must be as small as possible. As an example, the LHC reaches a β^* down to $0.4\,\mathrm{m}$ and the HL-LHC upgrade is supposed to reduce β^* further to $0.15\,\mathrm{m}$. This leads to the so-called 'mini beta' principle. To better understand the properties of this principle it is best to fix β^* at the IP and analyze the evolution of the β function from there. As β^* is the local (usually also the global) minimum, its derivative, the Twiss parameter α^*, must be zero. Consequently, the IP is a symmetry point and only one side of the interaction region needs to be studied. The IP must be surrounded by a detector to measure the physical processes of the collisions. Thus the surrounding area of the IP cannot be filled with accelerator elements to avoid interference with the detector. In high energy hadron colliders, the detectors can have a length of up to $40\,\mathrm{m}$ as they have to fully stop the debris particles in order to measure their energy. For the beam optics, this requires a long drift space of the length L^* between the IP and the first focusing magnets. The transfer matrix of a drift space with length L was determined as

$$M_{\mathrm{drift}} = \begin{pmatrix} 1 & L \\ 0 & 1 \end{pmatrix}, \tag{2.61}$$

see Eq. (2.12). With $L = L^*$ and keeping in mind that $\alpha^* = 0$, Eq. (2.25) gives the relation for the β function

$$\beta(L^*) = \beta^* + \frac{L^{*2}}{\beta^*}$$

$$\approx \frac{L^{*2}}{\beta^*} \tag{2.62}$$

The smaller β^* the larger the β functions at the end of the drift become. Also L^* has a significant impact. Subsequently, the β functions in the final focus system
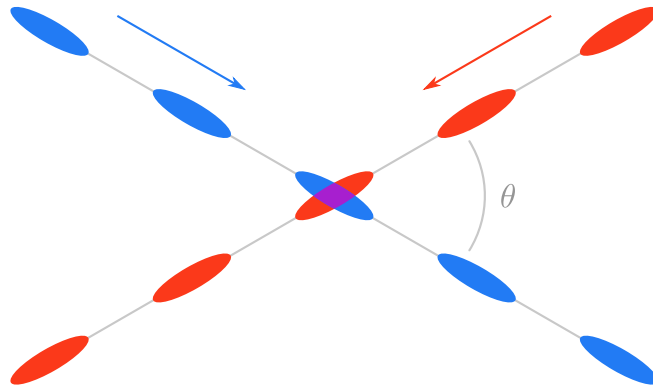
Figure 2.7: Luminosity reduction due to the crossing angle. The luminous region is limited to the overlap area (purple) of the bunches.

following the detector region drift usually are the highest in the whole machine. As an example, in the LHC, they reach values as high as $4500\,\mathrm{m}$ compared to around $170\,\mathrm{m}$ in the arcs. As both horizontal and vertical plane need focusing, this final focus system contains at least two quadrupoles. In the LHC three quadrupoles are used in order to have similar maximum values of the β functions in both planes. This is necessary as the large peaks of the β functions correspond to a large beam size which is limited by the magnet apertures. Thus aperture restrictions in the final focus system can set a limit for the maximum β function. According to Eq. (2.62) this limits the minimum β^* and subsequently the luminosity. Another issue arising from the large beam sizes is the chromaticity. From Eq. (2.40) it is immediately clear that the combination of large β and strong focusing will generate a large contribution to the chromaticity that requires strong sextupoles for correction. These strong non-linear elements will in turn affect the stability of particles with large amplitudes as discussed later.

There are several other factors that can reduce the luminosity. One is the crossing angle ϕ that reduces the overlap of the bunches, as is depicted in Fig. 2.7. The associated reduction factor for the luminosity is

$$F = \frac{1}{\sqrt{1 + \left(\frac{\sigma_s}{\sigma_x} \tan \frac{\phi}{2}\right)^2}} \tag{2.63}$$

for crossing in x. A mitigation measure for the crossing angle is the "crab crossing" scheme outlined in Fig. 2.8. The colliding bunches get a time dependent transverse kick from an RF cavity, causing them to rotate to restore effective head-on collisions. In FCC-hh the reduction factor from the crossing angle will become relevant and crab cavities will be required to compensate. However, due to the early stage of the design, they are not included in this thesis.
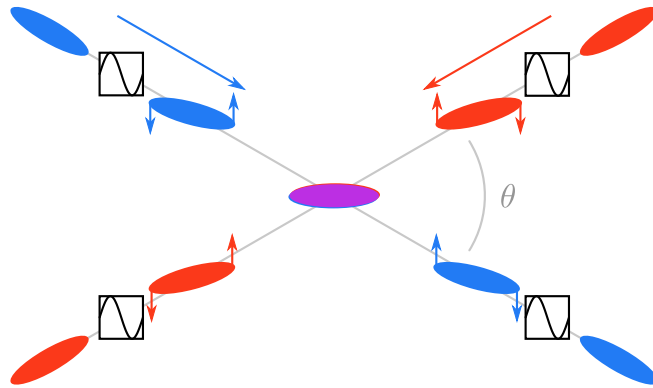
Figure 2.8: Principle of the crossing angle compensation by "crab crossing".

2.13   Beam-beam effects

When the counter-rotating bunches cross in the IP, the particles that do not collide still experience the strong electric field of the charge of the other beam. The field causes a kick that is linear for small amplitudes, acting like an additional lens. The resulting beam-beam tune shift is proportional to the luminosity and can cause particles to cross resonance lines and become instable. Usually, the maximum possible beam-beam tune shift is determined via particle tracking studies, with consequences for the maximum viable luminosity.

Furthermore the counter-rotating bunches also interact with each other around the IP where they share the same beam pipe as illustrated in Fig. 2.9. This is the long range beam-beam effect. The corresponding tune shift is inversely proportional to the normalized beam separation (beam distance divided by beam size). In the triplet region, the beam size is primarily determined by the beam divergence at the IP. Consequently a normalized beam separation of $N_{\mathrm{bb}} \cdot \sigma_x$ can be achieved by setting the crossing angle to $N_{\mathrm{bb}} \cdot \sigma_{x'}$.
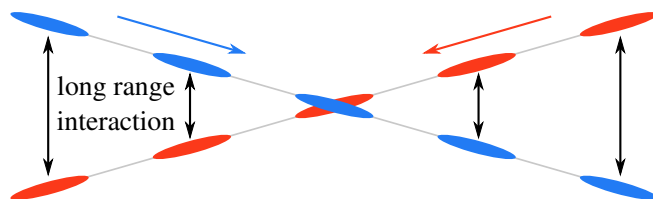

Figure 2.9: Long range beam-beam interactions.

2.14   Beam optics codes

The Methodical Accelerator Design (MAD) scripting language [21] is a general-purpose tool for charged-particle optics design developed and maintained at CERN. It is one of the standard tools to describe particle accelerators, simulate beam dynamics and optimize beam optics. A full documentation of the current version MAD-X can be found on the website [21].

In the framework of this thesis, MAD-X was used to define the sequences of elements of the optical lattices, calculate the optical parameters and obtain the linear optics. MAD-X features numerical optimization routines varying element parameters like, e.g. quadrupole strengths, to match local and global machine properties to predefined values (matching). Furthermore, it is possible to generate SixTrack input files from sequences loaded in MAD-X.

SixTrack [22] is a 6D single particle tracking code used for tracking studies for the LHC and HL-LHC. While MAD-X also provides its own tracking algorithm as well as an extension to run the Polymorphic Tracking Code (PTC), SixTrack has shown to be faster [23], making it the first choice for long term tracking studies of large machines like FCC-hh.

Chapter 3

Scaling from LHC and HL-LHC

3.1 LHC Interaction Region

With the LHC exceeding its design peak luminosity [24] at 13 TeV center-of-mass energy and the HL-LHC in a well advanced design phase [16], it is a good strategy for the FCC study to take advantage of the work and experience that have been put into these projects by using their lattices and adopting them to the challenges of FCC-hh. Both LHC and HL-LHC interaction region lattices for the high luminosity experiments ATLAS and CMS are similar in their underlying layout. The LHC interaction region lattice is shown in Fig. 3.1. Starting from the interaction point, a drift space of $L^* = 23\,\text{m}$ is reserved for the experiments. The only devices placed in this region are a beam position monitor and an absorber -Target Absorber Secondaries (TAS)- that protects the final focus system from debris of the particle collisions. In the case of ATLAS, the TAS is located between the big wheels of the muon spectrometer (Fig. 3.1 of [25]). For CMS, the TAS is outside the detector.

The magnets of the interaction region are numbered starting with the one closest to the IP. For example, Q4 corresponds to the fourth quadrupole in either direction. It should be noted that some magnets consist of two elements to reduce the individual lengths and weights. Still, they are powered by a single power supply and function as a single unit. In the LHC interaction region, this concerns the quadrupoles Q2 in the triplet (see Fig. 3.1) and Q7 as well as the separation dipole D1. In the case of HL-LHC, this also applies to Q1 and Q3.

At $s = 23\,\text{m}$ the first quadrupole Q1 of the final focus triplet (Q1 to Q3) starts. The triplet has an overall length of 31 m in the LHC case and 42 m in HL-LHC, including drift spaces between the quadrupoles. A corrector package consisting of skew quadrupoles and higher order multipoles is installed. The triplet consists of
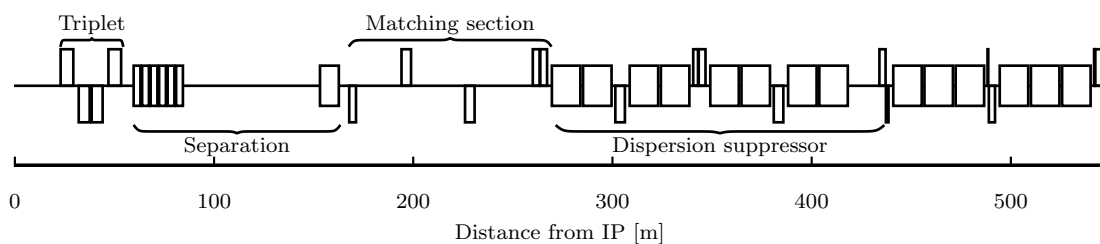

Figure 3.1: Layout of the LHC interaction region.

single aperture magnets that host both beams. The triplets on both sides of the IP are powered antisymmetrically. This has the advantage that the triplet region is optically identical for both beams. Crossing angles are created by orbit correctors located in and behind the triplet and behind the separation and recombination section. The crossing angle is in the vertical plane for ATLAS and in the horizontal plane for CMS. Behind the triplet, a shared aperture dipole D1 separates the two beams. After a drift of about 57 m, the double bore dipole D2 bends the separated beams onto parallel orbits again. The four quadrupoles Q4-Q7 form the so-called matching section, which is used to provide a smooth transition of the lattice functions from the interaction region to the regular arc. Due to the strong focusing required at Q7, it consists of two quadrupoles which are powered in series. The straight section has a total length of 537.8 m. The dispersion suppressor (DS) design was constrained by the LEP tunnel geometry [26, 27]. It consists of two FODO cells with the dipoles having the sole purpose of guiding the orbit on the reference trajectory of the LEP tunnel while the individually powered DS quadrupoles Q8-Q10 are used to match the dispersion function between arc and straight section. The end of the straight section has a non-zero dispersion due to the separation and recombination dipoles D1 and D2. In order to provide enough degrees of freedom to match all required beam parameters from the IP to the arcs, not only the matching section quadrupoles, but also the DS quadrupoles Q8-Q10 and the first three trim quadrupoles of the first arc FODO cell QT11-QT13 are used for the matching procedure. This is necessary to match the parameters β_x, α_x, μ_x, β_y, α_y, μ_y, D_x, D_x', while keeping the β functions behind the matching section on a level comparable to the arc sections. In the arcs, all magnets of one family (e.g. main dipoles, focusing quadrupoles, defocussing quadrupoles) for both beams are powered in series by a single power converter per arc. The resulting limited flexibility for optics correction is compensated by individually powered trim quadrupoles.

3.2   Scaling laws

Due to the increased energy, it is not possible to just copy the LHC or HL-LHC IR: the increased beam rigidity would require a proportional increase in the magnetic field. Unfortunately, there is no prospect for such an increase in current developments in magnet technology. Instead, a reasonable approach is to scale the IR length in order to cope with the decreased focusing (i.e. increased focal length) of the quadrupole magnets. In this section, the scaling of the normalized quadrupole gradient k and the β functions with respect to the length scaling factor α_s are derived.

3.2.1   Normalized quadrupole gradient

In thin lens approximation, the normalized quadrupole strength is equal to

$$k = \frac{1}{L_Q f},$$
(3.1)

with L_Q the quadrupole length and f the focal length, both of which are proportional to α_s. The scaled quadrupole length $L_Q' = \alpha_s \cdot L_Q$ increases the integrated quadrupole strength while an increased focal length $f' = \alpha_s \cdot f$ reduces the required integrated

quadrupole strength, so the normalized gradient scales like

$$k' = \frac{1}{L'_Q f'} = \frac{1}{\alpha_s^2 L_Q f} = \frac{k}{\alpha_s^2}, \tag{3.2}$$

where the prime denotes the scaled parameters.

3.2.2 Longitudinal scaling of the β function

It is worth to remember that Eq. (2.20) describes the behaviour of the β function with $u = \sqrt{\beta(s)}$

$$\frac{d^2 u}{ds^2} - \frac{1}{u^3} - ku = 0. \tag{3.3}$$

Under length scaling, ds' is proportional to α_s. Inserting this and Eq. (3.2) into Eq.(3.3) yields

$$\frac{d^2 u'}{ds'^2} - \frac{1}{u'^3} - k'_1 u' = \frac{1}{\alpha_s^2} \frac{d^2 u'}{ds^2} - \frac{1}{u'^3} - \frac{1}{\alpha_s^2} ku' = 0. \tag{3.4}$$

Inserting the ansatz

$$u' = \sqrt{\alpha_s} u \tag{3.5}$$

into Eq. (3.4) reproduces Eq. (3.3), i.e. the scaled beam optics are similar to the original optics. We can therefore conclude that

$$\beta' = \alpha_s \beta \tag{3.6}$$

3.3 Scaling strategies

With the general scaling laws established, we have to determine a length scaling factor α_s, that will provide viable optics at an increased beam energy of 50 TeV. There are different strategies, depending on the goal of the scaling, like a constant beam stay clear or constant quadrupole apertures.

3.3.1 Constant beam stay clear

The shortest possible interaction region length can be achieved by scaling for a constant beam stay clear [28]. The normalized quadrupole coefficient is given by

$$k = \frac{e}{p} \frac{\partial B_y}{\partial x}, \tag{3.7}$$

with e the elementary charge, p the particle momentum and $\partial B_y / \partial x$ the quadrupole gradient. In a simplified quadrupole model, the gradient $\partial B_y / \partial x$ can be described as

$$\frac{\partial B_y}{\partial x} = \frac{B_{max}}{r}, \tag{3.8}$$

with r the coil aperture radius and B_{max} the magnetic field at the coil aperture, which is determined by the used magnet technology. The coil aperture radius can be described as $r = N \cdot \sigma_x$ with $\sigma_x = \sqrt{\beta \epsilon_n / \gamma_L}$ being the beam size and N a number

representing both the normalized beam separation plus the beam stay clear required to obey the collimation hierarchy [16]. For the unscaled lattice, we can write

$$k = \frac{e}{p} \frac{B_{\mathrm{max}}}{N \sqrt{\beta \epsilon_{\mathrm{n}} / \gamma_{\mathrm{L}}}}. \tag{3.9}$$

Both, the particle momentum and the Lorentz factor γ_{L} scale with the energy increase.

$$p' = \frac{50 \, \mathrm{TeV}}{7 \, \mathrm{TeV}} \cdot p \tag{3.10}$$

$$\gamma_{\mathrm{L}}' = \frac{50 \, \mathrm{TeV}}{7 \, \mathrm{TeV}} \cdot \gamma_{\mathrm{L}} \tag{3.11}$$

This is compensated by increasing the IR length, so k' and β' increase according to the scaling laws in Eqs. (3.2) and (3.6). As a first guess, assuming a constant beam separation, a constant N preserves the beam stay clear of the unscaled lattice. The other parameters in Eq. (3.9) are also constant so we get

$$k' = \frac{e}{p'} \frac{B_{\mathrm{max}}}{N \sqrt{\beta' \epsilon_{\mathrm{n}} / \gamma_{\mathrm{L}}'}}. \tag{3.12}$$

According to Eq. (3.2) the ratio of the normalized gradients can be identified as the square of the length scaling factor α_{s}, thus dividing Eqs. (3.9) and (3.12) yields

$$\alpha_{\mathrm{s}}^2 = \frac{k}{k'} = \frac{p'}{p} \frac{\sqrt{\beta'}}{\sqrt{\beta}} \frac{\sqrt{\gamma_{\mathrm{L}}}}{\sqrt{\gamma_{\mathrm{L}}'}}. \tag{3.13}$$

Inserting Eqs. (3.6), (3.10) and (3.11) into Eq. (3.13) results in a length scaling factor of

$$\alpha_{\mathrm{s}} = \left(\frac{50 \, \mathrm{TeV}}{7 \, \mathrm{TeV}} \right)^{1/3} \approx 2 \tag{3.14}$$

that will preserve the beam stay clear when the particle energy is increased. This scaling accounts neither for different normalized emittances, nor for the increase of normalized separation needed due the higher number of long range beam-beam interactions.

3.3.2 Constant gradients and apertures

A constant beam stay clear is not the only valid option. Due to technical constraints and impedance issues, the collimation system is scaled in order to achieve collimator gaps similar to the LHC [29, 30]. As the beam stay clear requirement for the interaction region is determined by the collimation system via the collimation hierarchy, it makes sense to use a scaling factor for the IR lattice that also preserves magnet apertures and gradients. Instead of using the emittance reduction at higher energies to allow for small magnet apertures, it is possible to keep the gradient $\partial B_y / \partial x$ in Eq. (3.7) - and thus the coil aperture according to Eq. (3.8) - constant and only apply length scaling according to the reduced focal strengths. From Eqs. (3.2) and (3.7), we can deduce

$$\frac{k}{k'} = \frac{p'}{p} = \alpha_{\mathrm{s}}^2 \tag{3.15}$$

so the scaling factor is $\alpha_s = \sqrt{\frac{50\,\text{TeV}}{7\,\text{TeV}}} \approx 2.67$. A major advantage of this scaling is the constant gradient, allowing the reuse of existing magnet technology. As the β functions in the triplet also scale with α_s while the emittance decreases with $1/\gamma_L \propto \frac{7\,\text{TeV}}{50\,\text{TeV}} = \alpha_s^2$, the beam stay clear of the scaled lattice should increase with $\sqrt{1/\alpha_s} \approx 1.64$.

3.3.3 Minimum β^* under length scaling

An alternative to scaling with the beam energy is to start from a lattice with and scale it in length at constant energy in order to reduce the minimum β function at the IP $\beta^*_{\min}$ and to increase the luminosity.

In the scope of this work, $\beta^*_{\min}$ was assumed to be limited by the apertures of the triplet magnets. These apertures are affected by the length scaling factor α_s. To investigate the scaling of the β^* reach with α_s, we first have to determine the relation of β^* and the β function in the triplet. The direct approach using the transfer matrices of the magnets and drifts will become very difficult to handle for three quadrupoles, so we choose a more phenomenological approach: According to Eq. (2.26) the transfer matrix from the IP to any other point s_t in the triplet is given by

$$M = \begin{pmatrix} \sqrt{\frac{\beta}{\beta^*}}\left(\cos\Psi + \alpha^*\sin\Psi\right) & \sqrt{\beta\beta^*}\sin\Psi \\ \frac{(\alpha^*-\alpha)\cos\Psi - (1+\alpha^*\alpha)\sin\Psi}{\sqrt{\beta\beta^*}} & \sqrt{\frac{\beta^*}{\beta}}\left(\cos\Psi - \alpha\sin\Psi\right) \end{pmatrix} \qquad (3.16)$$

when β^*, $\beta = \beta(s_t)$ and phase advance Ψ are known. Specifically the matrix elements $m_{11}(s_t)$ and $m_{12}(s_t)$ that define the beam size are of interest here. The phase advance is calculated by

$$\Psi(s_t) = \int_0^{s_t} \frac{1}{\beta(s)}\,\mathrm{d}s. \qquad (3.17)$$

Starting from the IP, this can be divided into

$$\Psi(s_t) = \int_0^{L^*} \frac{1}{\beta^* + \frac{s^2}{\beta^*}}\,\mathrm{d}s + \int_{L^*}^{s_t} \frac{1}{\beta(s)}\,\mathrm{d}s. \qquad (3.18)$$

Evaluating the first part gives

$$\Psi(s_t) = \arctan\left(\frac{L^*}{\beta^*}\right) + \int_{L^*}^{s_t} \frac{1}{\beta(s)}\,\mathrm{d}s \qquad (3.19)$$

For any realistic IR lattice, $L^* \gg \beta^*$, giving $\arctan\left(\frac{L^*}{\beta^*}\right) \approx \frac{\pi}{2}$. Also, in the triplet the β function reaches values up to $80\,\text{km}$ in the case of FCC-hh so the second term of Eq. (3.19) is negligible. The phase advance from the IP to any point in the triplet is therefore $\Psi \approx \frac{\pi}{2}$. With this and $\alpha^* = 0$, the matrix element $m_{11}(s_t)$ vanishes while $m_{12}(s_t) \approx \sqrt{\beta\beta^*}$. Thus

$$\beta(s_t) \approx m_{12}^2(s_t)\frac{1}{\beta^*}. \qquad (3.20)$$

Next, the scaling of the quadrupole aperture is examined. With the normalized gradient definition in Eq. (3.7) and the aperture-gradient model given by Eq. (3.8), we can describe the coil aperture radius with

$$r = \frac{e}{p} \frac{B_{\mathrm{max}}}{k} \tag{3.21}$$

which scales with α_{s}^2, since k scales with $1/\alpha_{\mathrm{s}}^2$ according to Eq. (3.2). Layers that reduce the free aperture, like the liquid helium gap (LHe), Kapton insulator, cold bore, beam screen, beam screen insulator and shielding are assumed to be constant. Together with the closed orbit uncertainty, they are concentrated in the constant aperture reduction r_{etc}, so $r - r_{\mathrm{etc}}$ corresponds to the free aperture. It should be noted that in reality, the cold bore thickness scales with the coil aperture. This is a minor effect and can be easily incorporated in the following calculations.

Lastly, we need to scale the aperture requirement. We assume a constant beam stay clear requirement N_{bsc}. The crossing angle requirement due to beam-beam effects N_{bb} in units of beam sizes σ_x depends on the number of long range beam-beam interactions N_{lr} which is proportional to the distance between IP and separation dipole D1, consequently $N_{\mathrm{lr}} \propto \alpha_{\mathrm{s}}$. According to [31], the long range beam-beam tune shift scales approximately with

$$\Delta Q_{\mathrm{lr}} \propto \frac{N_{\mathrm{lr}}}{N_{\mathrm{bb}}^2}. \tag{3.22}$$

With $N_{\mathrm{lr}} \propto \alpha_{\mathrm{s}}$ we get a constant tune shift ΔQ_{lr} for $N_{\mathrm{bb}} \propto \sqrt{\alpha_{\mathrm{s}}}$. Under normal scaling, both β and β^* are proportional to the length scaling factor α_{s} (see Sec. 3.2.2). Furthermore, we have shown that the matrix element $m_{12}(s_{\mathrm{t}}) \approx \sqrt{\beta\beta^*}$ in the triplet, thus $m_{12}(s_{\mathrm{t}}) \propto \alpha_{\mathrm{s}}$, which must hold true independent of β^*. Consequently, if β^* is kept constant, the beam size at any given point in the triplet scales with $\sigma_x \propto \sqrt{\beta} \propto \alpha_{\mathrm{s}}$.

At the aperture bottleneck the free magnet aperture $r - r_{\mathrm{etc}}$ and the aperture requirements of the beam should be the same, so we can write

$$r - r_{\mathrm{etc}} = \left(N_{\mathrm{bsc}} + \frac{N_{\mathrm{bb}}}{2} \right) \sigma_x. \tag{3.23}$$

Using the substitution for r in Eq. (3.21) and including all the scaling behaviors derived above yields

$$\frac{eB_{\mathrm{max}}}{pk}\alpha_{\mathrm{s}}^2 - r_{\mathrm{etc}} = \left(N_{\mathrm{bsc}} + \frac{N_{\mathrm{bb}}}{2}\sqrt{\alpha_{\mathrm{s}}} \right) \sigma_x \alpha_{\mathrm{s}}. \tag{3.24}$$

We can see that α_{s} must be

$$\alpha_{\mathrm{s}} > \sqrt{\frac{pk}{eB_{\mathrm{max}}} \cdot r_{\mathrm{etc}}} \tag{3.25}$$

in order to guarantee a free aperture $r > r_{\mathrm{etc}}$. By replacing the beam size at the aperture bottleneck $\sigma_x(s_{\mathrm{bn}}) = \sqrt{\epsilon\beta(s_{\mathrm{bn}})} \approx \sqrt{\frac{\epsilon \cdot m_{12}^2(s_{\mathrm{bn}})}{\beta^*}}$, Eq. (3.24) can be transformed to

$$\beta^* = \frac{\left(N_{\mathrm{bsc}} + \frac{N_{\mathrm{bb}}}{2}\sqrt{\alpha_{\mathrm{s}}} \right)^2 \cdot \epsilon \cdot m_{12}(s_{\mathrm{bn}}) \cdot \alpha_{\mathrm{s}}^2}{\left(\frac{eB_{\mathrm{max}}}{pk}\alpha_{\mathrm{s}}^2 - r_{\mathrm{etc}} \right)^2}. \tag{3.26}$$

Note that the non-normalized emittance ϵ is used, since the energy is constant in this scaling. The matrix element $m_{12}(s_{\mathrm{bn}})$ can be obtained by inserting the known values of the unscaled lattice, including β^*_{min}, and a scaling factor $\alpha_{\mathrm{s}} = 1$. The position of the aperture bottleneck is implicitly given by equating aperture and aperture requirement in Eq. (3.24) and by assuming the bottleneck will remain at the same (scaled) position in the triplet. With this constant, the lattice can be scaled, giving the achievable β^* for any scaling factor. For very large α_{s}, Eq. (3.26) can be reduced to

$$\beta^* \approx \frac{\frac{N_{\mathrm{bb}}}{2}\epsilon m_{12}(s_{\mathrm{bn}})}{\frac{eB_{\mathrm{max}}}{pk}} \cdot \frac{1}{\alpha_{\mathrm{s}}}. \tag{3.27}$$

This means, theoretically any β^* reachable for a sufficiently large scaling factor.

This scaling approach to minimizing β^* is complementary to a previous study using constant gradient point to parallel focusing [32] to explore the maximum β function, total length and chromaticity of a final focus system.

Chapter 4

Lattice options

In this chapter, the different lattice options for the FCC-hh interaction region resulting from different scaling strategies will be presented. The different lattice options are given by their L^* as an identifier. Important parameters of the different lattices are summarized in Table 4.1.

Table 4.1: Parameters of the lattice options.

	LHC	HL-LHC	FCC-hh			
L^*[m]	23	23	36	45	46	61.5
Normalized transverse emittance ϵ_{n} [µm]	3.75	2.5		2.2		
Quadrupole length $L_{\mathrm{Q1/Q3}}$[m]	6.37	7.685	20	31.81	12.74	20.54
Quadrupole length $L_{\mathrm{Q2a/b}}$[m]	5.50	6.577	17.5	26.37	11.0	17.58
Quadrupole coil aperture diameter [mm]	70	150[1]	100/115[2]	205/248	62	140
Quadrupole gradient [T/m]	215	140[1]	220/190	107/89	365	150
Normalized separation [σ]	9.4	12.5	12	15.2	12	14

[1] 140 mm aperture with 150 T/m gradient in the optics variant SLHC V3.1b
[2] Two values indicate two magnet types

4.1 Scaled LHC interaction region with $L^* = 46\,\mathrm{m}$

The first lattice option is obtained from scaling with constant beam stay clear as derived in Section 3.3.1. Applying the corresponding scaling factor $\alpha_{\mathrm{s}} = 2$ to the LHC lattice results in an L^* of 46 m. The total length of the straight section is 1075.6 m, shorter than the 1.4 km specified in the preliminary baseline parameter report [15]. The separation section was modified to provide a beam separation of 300 mm. Scaling from the minimum $\beta^* = 0.4\,\mathrm{m}$ accomplishable in the LHC [33] results in a minimum β^* of 0.8 m in the scaled lattice. The corresponding optics are plotted in Fig. 4.1.

Apart from a thicker beam pipe in Q1, the LHC triplet has no dedicated shielding inside the quadrupoles to protect them from collision debris coming from the IP. In
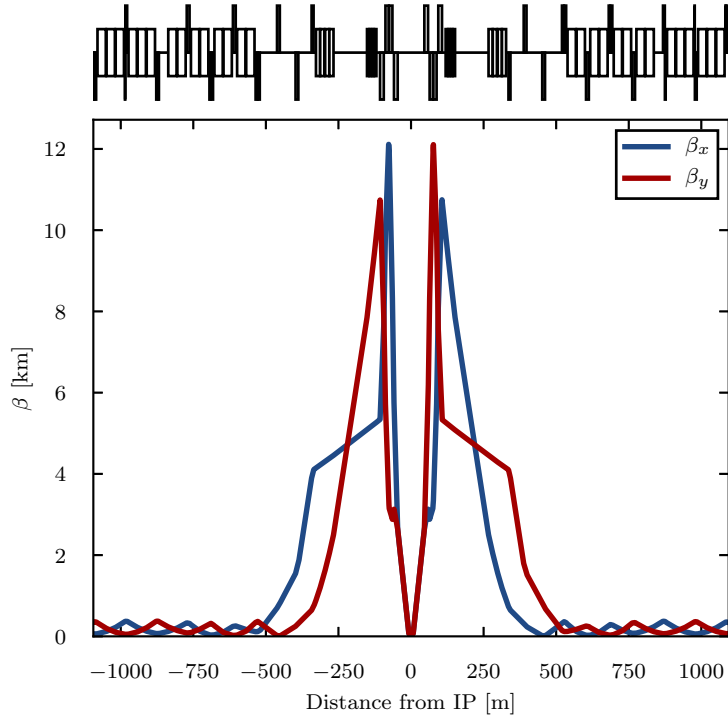
31

Figure 4.1: β functions of the scaled LHC lattice with $L^* = 46\,\text{m}$ for $\beta^* = 0.8\,\text{m}$. At the top, the lattice elements are depicted. The centered blocks are dipoles and the blocks above and below the center line are horizontally focusing and defocusing quadrupoles. The β function in the dispersion suppressors are scaled as well and will be adapted to the arc lattice.

FCC-hh, this will become a problem, as the radiation load is expected to increase by two to three orders of magnitude. To study the impact of the radiation, FLUKA [34, 35] simulations (with DPMJET-III as event generator [36, 37]) of the final focus triplet were conducted by the FCC-hh FLUKA team [1, 4]. In this first radiation simulation, a coil aperture diameter of 62 mm was used. The free aperture radius was further reduced by 0.5 mm for the Kapton insulator, 1.5 mm spacing for the Liquid Helium (LHe) and a 2 mm thick cold bore, each modeled as a simple layer. The beam screen and clearance were accounted for by additional 2 mm in the calculation of the beam stay clear, but were not modeled for the FLUKA simulation. The aperture diameter of the TAS was set to 15 mm. With this set of parameters, the triplet is completely in the shadow of the TAS. The beam stay clear with these parameters is $12\,\sigma$ with a beam separation of $12\,\sigma$ corresponding to 86 µrad crossing angle.

Figure 4.2 shows the results of the FLUKA simulation, both in terms of peak power density and peak dose. As discussed earlier, a high power density can cause quenches of the superconducting magnets and is driven by the instantaneous luminosity. The peak dose is associated with the degradation of insulator material and depends on the integrated luminosity. The highest power density in the FCC lattice occurs at the end of Q1 with about $230\,\text{mW/cm}^3$. This is about 70 times more than the maximum power density in the LHC triplet (about $3\,\text{mW/cm}^3$). Depending on the used superconducting technology, the assumed quench limit for the coils is about $40\,\text{mW/cm}^3$ (Nb_3Sn) or $13\,\text{mW/cm}^3$ (NbTi) [16]. Thus the power density is 6-20
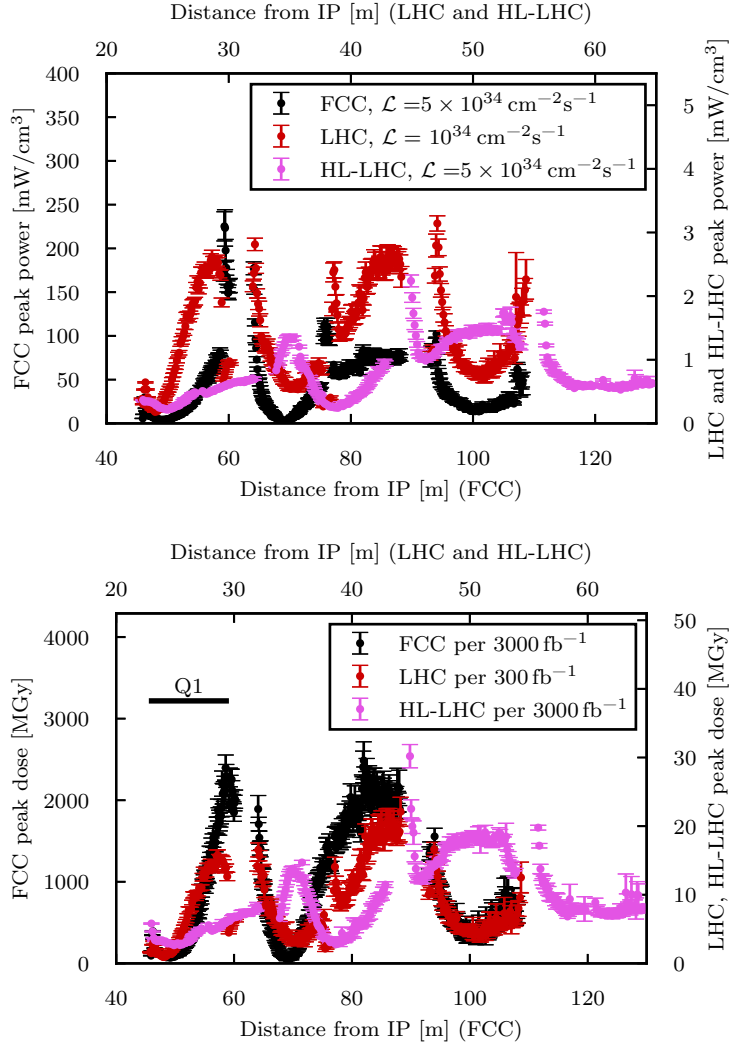
Figure 4.2: Peak power densities (top) and peak doses (bottom) for the first lattice compared with LHC and HL-LHC for horizontal crossing. The horizontal axes were chosen to overlap similar magnets in the LHC and FCC lattices. The crossing angles were 285 μrad for LHC, 590 μrad for HL-LHC and 86 μrad for FCC. Data from [4].

times higher than the quench limit. Furthermore, at design level the power density should be lower than the quench limit by a safety factor of 3 [38]. Looking at the peak dose, the highest values also occur at the end of Q1. With around 2400 MGy per 3000 fb^{-1}, the radiation load is almost two orders of magnitude higher than what is currently considered the lifetime limit of 30 MGy [16, 39].

It is obvious that these enormous discrepancies between expected load and feasible operational limit, both in terms of peak power and peak dose, need to be addressed. A straight forward option to reduce the radiation load is shielding placed inside the quadrupoles, as it is foreseen for HL-LHC. In this case the triplet magnets have an aperture diameter of 150 mm and shielding of 16 mm (6 mm) thickness in Q1 (Q2/Q3). Placing similar amounts in the triplet magnets of the scaled lattice would reduce the free aperture diameter in Q1 to 22 mm and to 42 mm in Q2 and Q3. This would greatly limit the reachable β^* and thereby the instantaneous lu-

minosity of the collider. With the limitation in Q1, not even the baseline goal of $\beta^* = 1.1$ m would be possible. Furthermore, the same amount of shielding in FCC will be less effective than in HL-LHC due to the higher energy of the debris and the resulting longer penetration depth. The triplet has to be adapted to this challenge. The aperture of the triplet magnets needs to be increased from this first design to allow for the necessary amount of shielding. Consequently, the gradient must be decreased according to Eq. (3.8). This can be done by increasing the triplet length to keep the focal length constant or increasing the focal length and thereby L^*. As both measures also increase the beam size in the triplet, the net gain has to be studied. Either way it is clear that the radiation mitigation measures will be the driving factors of the triplet design.

4.2 Scaled HL-LHC triplet with $L^* = 36\,\mathrm{m}$

In this section, the effect of an increased triplet length is explored. For this purpose, the HL-LHC lattice (specifically the optics variant SLHC V3.1b [16]), having a triplet already $\approx 20\,\%$ longer than the LHC, was scaled by the factor 2 according to the scaling derived in Section 3.3.1. After this scaling, the triplet magnets were lengthened by an additional $30\,\%$ in order to further decrease the gradients, increase the apertures and subsequently accommodate more shielding. However, a longer triplet results in larger peak β functions. To limit their increase, L^* was reduced to $36\,\mathrm{m}$ which requires stronger focusing and therefore counteracts the gradient reduction due to the longer triplet. Still a net gain is expected. The L^* is close to the upper limit of early detector design studies, suggesting a detector half length between 25 and $40\,\mathrm{m}$ [40]. Thus it can be considered realistic.

Since the lengthening of the final focus triplet and the reduction of L^* changed the optics considerably, rematching was necessary. Unlike the LHC and HL-LHC triplets, which were partly involved for matching the optical functions from the IP to the arcs, the FCC triplet matching focused only on optimizing the beam stay clear in order to optimally use the available free aperture in this first step. The first matching constraint to be met by the optimization was $\beta_{x,\mathrm{max}} = \beta_{y,\mathrm{max}}$. The maximum β function in one plane occurs in Q2 and in the other plane in Q3. Due to the imposed antisymmetry of the interaction region, the first matching constraint makes sure the aperture limitation on both sides of the IP is the same due to equal beam sizes and apertures. Consequently, only one side of the IP is needed for this optimization. This also holds true when applying a crossing angle, as the induced separation is given in numbers of beam sizes and barely deviates from that value within the triplet. As no arc optics were available at the time of this study, the β functions around Q4 were matched to be below $\frac{\beta_{\mathrm{max}}}{4}$ and the α functions to be positive.

For first radiation studies, the coil aperture diameter of the triplet magnets was set to $100\,\mathrm{mm}$. The crossing angle was set to $140\,\mathrm{\mu rad}$ corresponding to a beam separation of $12\,\sigma$ at $\beta^* = 0.3\,\mathrm{m}$. This value is expected to be feasible because it corresponds to the scaled β^*_{min} of the HL-LHC this lattice is based on. A vertical crossing scheme was chosen as it is the worst scenario in terms of total energy deposition. The more abundant positive collision debris particles are subject to an earlier capture compared to horizontal crossing, since they enter with a vertical offset in the first quadrupole, where they are further defocused in this plane. In the
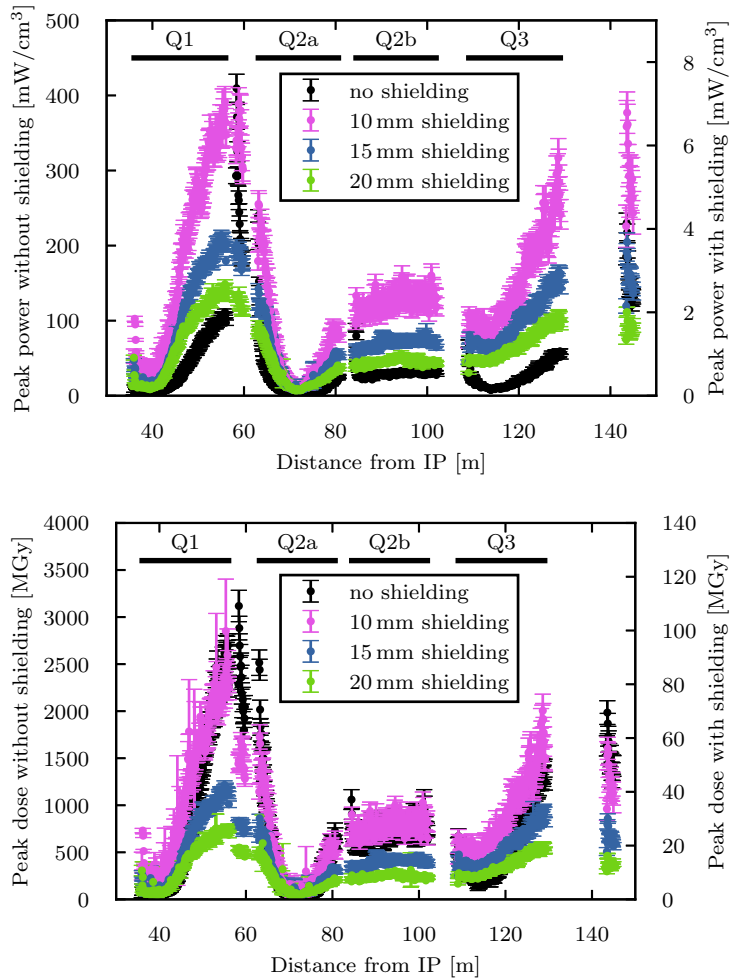
Figure 4.3: Peak power densities (top) and peak doses per $3000\,\mathrm{fb}^{-1}$ (bottom) along the triplet for the $L^* = 36\,\mathrm{m}$ lattice for different shielding thicknesses at $140\,\mathrm{\mu rad}$ vertical crossing angle and assuming $100\,\mathrm{mm}$ coil aperture. Data from [4].

FLUKA model, the free aperture was reduced by the cold bore, the Kapton insulator and spacing for liquid helium (see Table 4.2) as well as various shielding thicknesses. The TAS was placed $2\,\mathrm{m}$ before the triplet to leave space for cryostat and vacuum equipment. The shielding was modeled as a continuous layer of INERMET180, a tungsten heavy alloy. Figure 4.3 shows the distributions of the peak power densities and peak doses resulting from the simulation, with different shielding thicknesses ranging from 0 to $20\,\mathrm{mm}$. The results show that a shielding thickness of at least $15\,\mathrm{mm}$ is necessary in order to get a peak dose in the order of $30\,\mathrm{MGy}$ for $3000\,\mathrm{fb}^{-1}$, the expected region of technical feasibility. For this amount of shielding, the peak power density is below the quench limits of both Nb_3Sn and $NbTi$, including the safety factor of 3. This first specific figure allows to define the available aperture including all required layers and to calculate the beam stay clear. This is necessary to optimize the usage of the available aperture and study the minimum β^* of the lattice.

The matching constraint used earlier, $\beta_{x,\mathrm{max}} = \beta_{y,\mathrm{max}}$, only results in an optimized triplet if stronger focusing (i.e. smaller β_{max}) in one plane would result in a

Table 4.2: Parameters used for the beam stay clear calculation

B_{max}	11 T
Crossing angle θ	$12\,\sigma_{\mathrm{x'}}$
Closed orbit uncertainty	2 mm
Beta beating	20 %
Layer thickness	
- Shielding	15 mm
- Liquid helium	1.5 mm
- Kapton insulator	0.5 mm
- Cold bore	2 mm
- Beam screen	2.05 mm
- Beam screen insulation	2 mm

more divergent beam (larger β_{max}) in the other plane. To account for the possibility that both peak β functions could still be reduced, the beam stay clear itself was also matched to the required value of e.g. $12\,\sigma$. When this value was met, the matching was repeated with a smaller β^*, until the matching did not converge to a solution anymore, indicating the minimum β^* possible with this lattice and the given beam stay clear requirement was reached. The beam stay clear for matching was calculated similarly to the APERTURE module of MAD-X [21]: the coil aperture radius was calculated according to Eqs. (3.7) and (3.8). From the coil aperture, the closed orbit uncertainty, the shielding thickness and various other layer thicknesses were subtracted (see Table 4.2) to get the available free aperture. This was again divided by the maximum beam size determined by β_{max} to get the beam stay clear.

So far, the quadrupole aperture was assumed to be constant in the whole triplet. The maximum value was defined by the strongest gradient required. When probing the minimum β^*, Q1 happened to be about 20 % stronger than Q2 and Q3. However, the peak β functions creating the aperture bottlenecks were located in Q2 and Q3 (see Fig. 4.4). Their lower gradients allow to increase their coil apertures without exceeding the technical limits, thus increasing the overall beam stay clear. Consequently, a smaller minimum β^* can be expected when individual apertures in Q1 and Q2/Q3 are used.

In Fig. 4.5 the minimum β^* as a function of the required beam stay clear is plotted for both uniform apertures (all coil apertures are 100 mm in diameter defined by the strongest gradient in Q1) and for individual apertures (Q2 and Q3 coil apertures are 115 mm in diameter defined by their strongest gradient, Q1 is still at 100 mm). As expected, the minimum β^* is considerably better for individual apertures. For uniform apertures, the "ultimate" goal of 0.3 m is barely reached. For individual apertures, the β^* reaches $\beta^* = 0.18$ m. Alternatively, the "ultimate" goal can be reached even for beam stay clear requirements of $17\,\sigma$. Furthermore, even with individual apertures, there is still space left in Q1 for more shielding. Up to 24 mm shielding thickness is possible in Q1 without reducing the overall beam stay clear limited in Q2 and Q3.

To estimate the gain from more shielding in Q1, the results of the FLUKA simulations with 20 mm in Fig. 4.3 can be taken. It should be noted that in the model used in FLUKA, the shielding thickness is kept constant along the triplet, although 20 mm of shielding in Q2 and Q3 would limit the beam stay clear. To get a
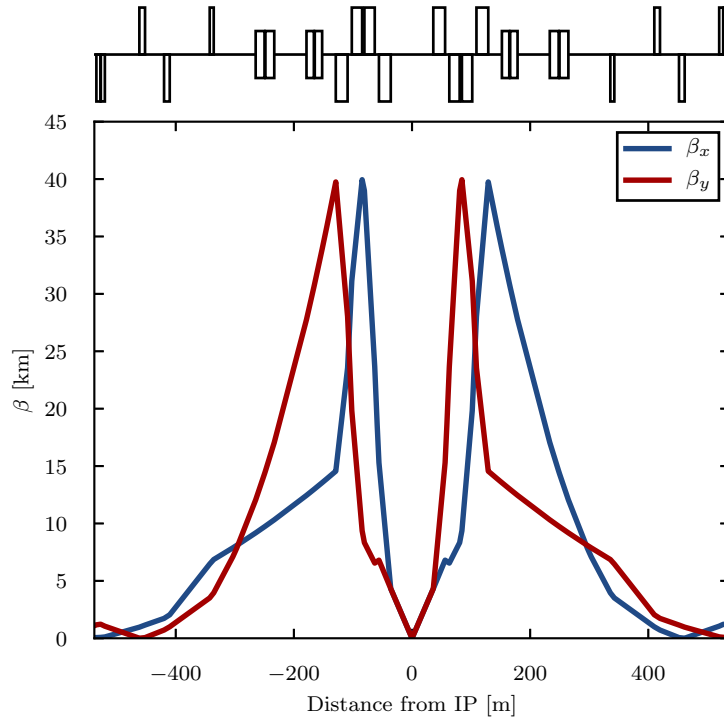
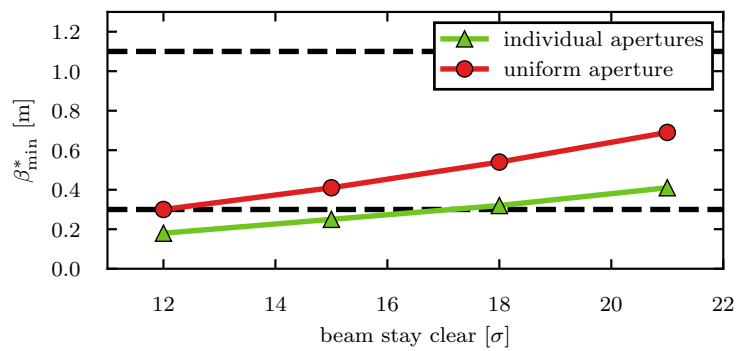**Figure 4.4:** Interaction region with $L^* = 36$ m and $\beta^* = 0.3$ m.

Figure 4.5: Minimum β^* of the $L^* = 36$ m lattice for beam star clear requirements of 12-21 σ. The baseline goal of $\beta^* = 1.1$ m poses no problem from the aperture point of view. The "ultimate" goal of $\beta^* = 0.3$ m can barely be reached with uniform apertures. With individual apertures, the baseline can be reached or exceeded within a beam stay clear of up to $\approx 17 \, \sigma$.

realistic estimate, the peak doses for 20 mm in Q1 and for 15 mm from Q2 onwards should be regarded. With this in mind, the maximum peak dose for $3000\,\text{fb}^{-1}$ is in Q3 and reaches about 30 MGy, a value considered feasible with current technology. In case of individual apertures, we can expect the peak doses at the beginning of Q2 and the end of Q3 to drop as the coils are more retracted and exposed to less radiation[1]. With individual apertures, the maximum peak dose will thus be at the end of Q1 with about 27 MGy. In this case the magnets should be able to withstand the integrated luminosity of $3000\,\text{fb}^{-1}$. However, for "ultimate" parameters, one high luminosity run is expected to average $1000\,\text{fb}^{-1}$/year over a five-year period [15]. Thus the magnets must be able to withstand an integrated luminosity of at least $5000\,\text{fb}^{-1}$ to allow running the full period without replacing them. Even this can only be considered the absolute minimum goal. Studies of the irradiation of the LHC triplet after only $300\,\text{fb}^{-1}$ at $L = 10^{34}\,\text{cm}^{-2}\text{s}^{-1}$ estimate a 4 to 6 months cool-down time before the ambient doses in the triplet area are low enough to allow work on the magnet exchange [41]. With $5000\,\text{fb}^{-1}$ per operational cycle and an instantaneous luminosity of $L = 5 \times 10^{34}\,\text{cm}^{-2}\text{s}^{-1}$, the necessary cool-down times will become considerably longer for FCC-hh. Together with 6 to 8 months of work required for the magnet exchange, this becomes incompatible with the foreseen shut-down time of 1.5 years as for the LHC [15]. A more realistic goal for the survivable integrated luminosity is therefore the equivalent of several high luminosity runs or ideally the whole foreseen scenario of $17\,500\,\text{fb}^{-1}$. As a consequence, the triplet needs further optimization in terms of radiation load, preferably without concessions in performance.

4.3 Scaled HL-LHC triplet with $L^* = 61\,\text{m}$

The lengthening of the triplet leading to the $L^* = 36\,\text{m}$ lattice significantly increased the coil apertures from 62 mm to 100 - 115 mm. This allowed for a smaller $\beta^*_{\min}$ while still leaving space for shielding. However, by using the second scaling strategy with constant gradients and apertures proposed in Section 3.3.2, the HL-LHC magnet design could be reused for FCC-hh, featuring even larger apertures than the previous lattice. Various advantages are expected from this coil aperture increase: As the coils are more retracted, the radiation load should decrease, making similar or less shielding necessary to survive the same integrated luminosity. With the same amount of shielding, the relative reduction of the free aperture will be less, due to the larger coil apertures. Thus a smaller $\beta^*_{\min}$ can be expected. Alternatively, for the same $\beta^*_{\min}$, thicker shielding could be accommodated, allowing to survive a higher integrated luminosity.

Applying the corresponding scaling factor $\alpha_\text{s} = \sqrt{\frac{50\,\text{TeV}}{7\,\text{TeV}}} \approx 2.67$ to the HL-LHC lattice (optics version SHLC V3.1b) leads to $L^* = 61.5\,\text{m}$. Different to the last case the triplet length was not further increased after the scaling. Due to the larger distance between the IP and the separation dipoles, the crossing angle had to be increased to $14\,\sigma_{x'}$. This resulted in a larger orbit bump and consequently increased the normalized separation, keeping the effect of long range beam-beam interactions constant.

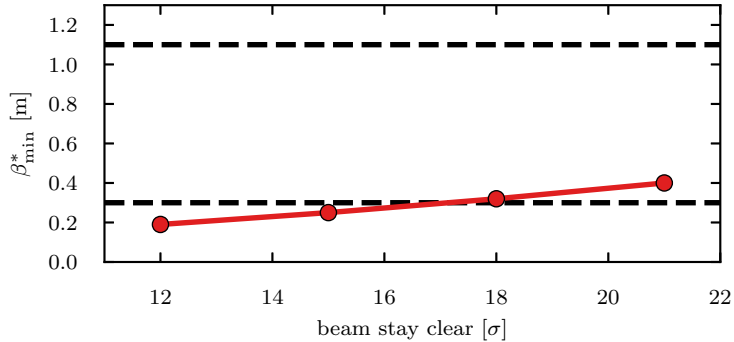[1]This can later be seen in the results of the Q1 split in Chapter 5

Figure 4.6: β^* reach of the $L^* = 61$ m lattice for beam stay clear requirements of 12-21 σ. The reachable β^* is very similar to the one of the $L^* = 36$ m lattice with individual apertures. Note that the triplet magnets in the $L^* = 61$ m all have similar gradients, so all apertures are the same.

The β^* reach of the new lattice was calculated as described previously. The scaling with constant gradient $\partial B_y/\partial x = 150$ T/m and constant apertures $2r = 140$ mm corresponds to $B_{max} = 10.5$ T instead of 11 T used in the previous lattice. The resulting β^*_{min} are plotted in Fig. 4.6. Unlike in the $L^* = 36$ m lattice, the matching of the triplet at $L^* = 61$ m for a maximum beam stay clear resulted in very similar quadrupole gradients for the whole triplet, so an option with individual apertures offers minuscule advantages. Comparing Fig. 4.6 and Fig. 4.5 reveals that the minimum β^* reachable in both lattices is almost the same. Although the relative impact of the shielding on the free aperture is smaller due to a larger coil aperture, the increased normalized separation increases the orbit excursion and thereby reduces the beam stay clear. The maximum β functions in the triplet and the associated expected gain in β^*_{min} are thereby limited. The different B_{max} only has a negligible impact.

Although the scaling leading to $L^* = 61$ m did not improve the minimum β^*, it is worth studying the impact on the energy deposition. Figure 4.7 shows radiation load for the new lattice alongside the load for the $L^* = 36$ m lattice. The peak doses in the most problematic areas were reduced by about 20 % at constant shielding thickness. The main reasons for this are the larger coil apertures as well as the reduced gradients, limiting the particle losses in the defocusing planes. A counteracting effect comes from the larger crossing angle but the overall effect is a reduced load.
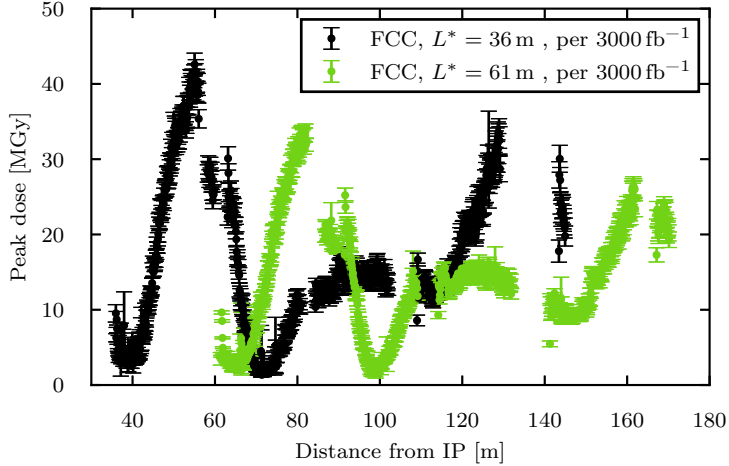
Figure 4.7: Comparison of the peak doses per $3000\,\mathrm{fb}^{-1}$ for the $L^* = 36\,\mathrm{m}$ and the $L^* = 61\,\mathrm{m}$ lattices for vertical crossing and with $15\,\mathrm{mm}$ shielding. Data from [4].

4.4   Minimum β^* in the presence of thick shielding

Although L^* increased significantly with $\alpha_\mathrm{s} = \sqrt{\frac{50\,\mathrm{TeV}}{7\,\mathrm{TeV}}}$ in the previous case, the lengths of the triplet magnets are almost the same as in the $L^* = 36\,\mathrm{m}$ lattice due to the $30\,\%$ length increase performed on the $L^* = 36\,\mathrm{m}$ lattice. The impact of changing the triplet length versus changing L^* is therefore worth studying. However, changing the ratio of the triplet lengths and L^* will require rematching in order to have optimized optics, making analytical descriptions of the beam stay clear of the optimized lattice non-trivial. Instead the length scaling approach to minimize β^* deduced in Section 3.3.3 can be used to qualitatively describe β^* reach vs. L^* and triplet length in the presence of considerable amounts of shielding.

For this purpose, the scaling of β^* described in Eq. (3.26) is applied to the lattices studied above on top of the first scaling. Figure 4.8 shows the resulting β^* reach when the formula is applied to the $L^* = 36\,\mathrm{m}$ lattice (top) and the $L^* = 61\,\mathrm{m}$ lattice (bottom). The markers show the cases where the analytically scaled β^* reach was verified by MAD-X aperture calculations. The region with $\alpha_\mathrm{s} > 1$ is of most interest as β^*_min decreases with $1/\alpha_\mathrm{s}$. In this region, the plots show that both scaled lattices feature almost the same minimum β^* at the same scaling factors. Furthermore, both lattices have almost the same lengths of the triplet magnets for any scaling factor (difference $2.5\,\%$). Consequently, only L^* is significantly differing with the scaling factor. This suggests, that L^* alone has a rather small impact. The main contribution for the smaller minimum β^* at larger scaling factors seems to be caused by the triplet length as can be seen by comparing the β^* reach in both scalings at equal L^*. For example, for an L^* of $60\,\mathrm{m}$ the minimum β^* at $12\,\sigma$ beam stay clear is $0.04\,\mathrm{m}$ in the upper plot of Fig. 4.8 but only $0.21\,\mathrm{m}$ in the lower plot. The significant differences here are the lengths of the triplet magnets.

These observations suggest a clear strategy to maximize the β^* reach with significant amounts of shielding reducing the free aperture of the final focus magnets: to choose the smallest L^* that does not restrict the detector design and to increase triplet length until dynamic aperture or chromaticity become obstacles. Following
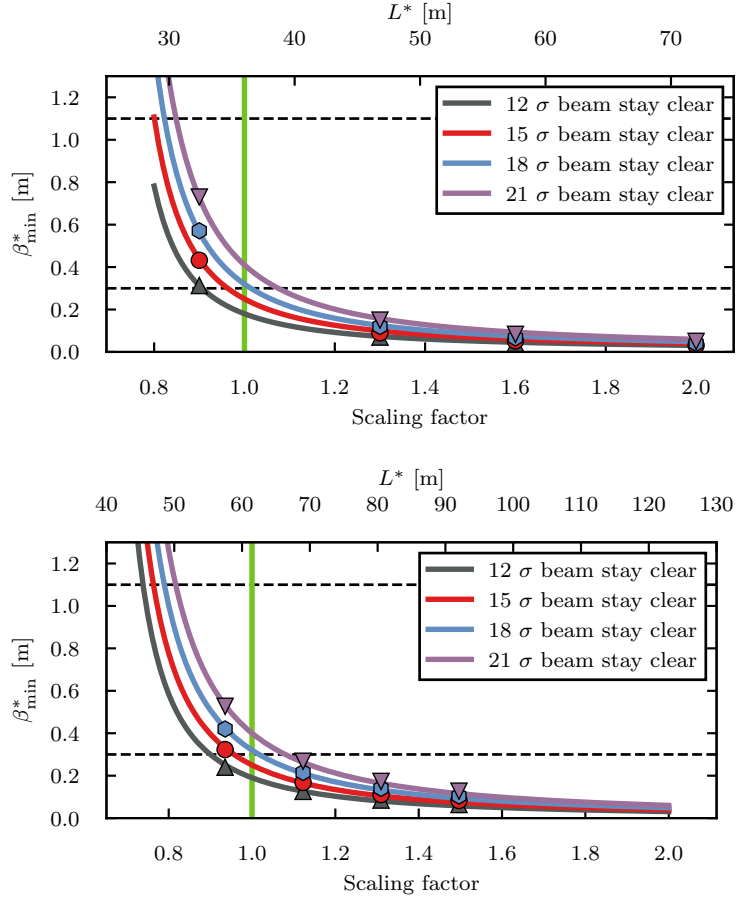
Figure 4.8: Minimum β^* for the $L^* = 36$ m lattice (top) and $L^* = 61.5$ m (bottom) lattice analytically scaled in length, scaling factor and resulting L^* (top horizontal axis). Markers show $\beta^*_{\min}$ values obtained with MAD-X aperture calculations. The green vertical lines indicate the non-scaled value.

this design strategy as well as new requirements from the detector baseline design [42], a new lattice with $L^* = 45$ m was developed, which will be discussed in the following section.

4.5 Baseline FCC-hh interaction region with $L^* = 45$ m

In accordance with the design strategy derived above, the new L^* was chosen to comply with the constraints imposed by the detector. A feature of the new detector design is the introduction of a horizontal forward spectrometer dipole with an integrated field of 10 Tm [42] that must be compensated by a corrector dipole. Figure 4.9 shows a sketch of one side of the new detector layout dictating the choice of L^*. At a distance of $s = 14.8$ m to 21 m from the IP, a 10 Tm dipole acts as a forward spectrometer. The forward detector has a conical beam pipe with an opening angle of 2.5 mrad resulting in a beam pipe aperture diameter of 16 cm at the end of the forward muon spectrometer at $s = 32$ m. From there, a short cone brings the beam pipe diameter down to the TAS diameter of 50 mm. The cavern
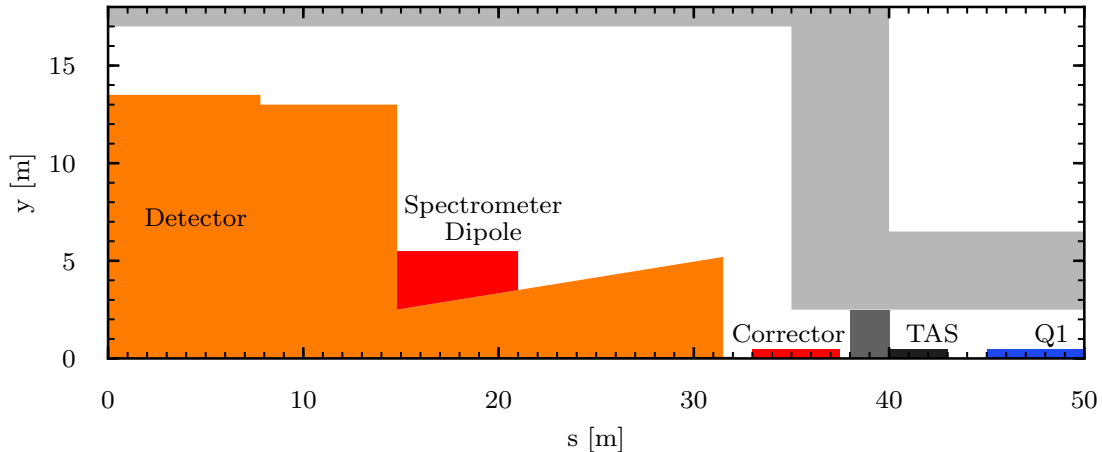
Figure 4.9: Detector and interaction region layout leading to the $L^* = 45\,\text{m}$ lattice. The IP is located at $(0, 0)$.

ends at $s = 35\,\text{m}$. The space of $3\,\text{m}$ between forward muon spectrometer and tunnel is needed to open up the detector and cannot be filled with immovable equipment. Hadrons hitting the TAS create secondary particles that the detector needs to be shielded from. In the LHC, ATLAS is protected by the two forward shielding assemblies, each consisting of more than 400 tonnes of iron and steel on a bridge section as well as a nose shielding of 117 tonnes of iron per side. CMS is protected by partly movable forward shielding weighting about 260 tonnes per side in addition to support structures of the similar mass. To avoid mechanical challenges and limit costs, the TAS of FCC-hh is supposed to be housed in the tunnel, behind a shielding wall of $2\,\text{m}$ thickness. The TAS is a $3\,\text{m}$ long cylindrical copper collimator. Between TAS and Q1, $2\,\text{m}$ of space are required for the end of the cryostat and vacuum equipment. The compensator dipole is supposed to correct the orbit offset created by the forward spectrometer. To get the best compensation, the corrector should be placed as close to the spectrometer as possible. Placing it between detector and shielding wall is therefore more effective than between TAS and Q1. Estimations from the $L^* = 61\,\text{m}$ lattice suggest that a $-7\,\text{Tm}$ corrector dipole, working together with the final focus triplet and the crossing angle orbit correctors, is sufficient and can be realized within a length of $4.7\,\text{m}$ using a normal conducting magnet. Normal conducting technology was chosen due to its robustness in the highly radiative environment [43]. In addition, no cryostat is needed, easing the removal of the magnet for detector maintenance. Placed before the shielding wall, the orbit corrector must not be hit by collision debris, in order to avoid background in the detector. Thus, a large aperture is required. The conical beam pipe of the forward detector ends with an aperture of $16\,\text{cm}$, so the compensator dipole aperture should be larger than this. $17\,\text{cm}$ was considered enough to avoid radiation being intercepted and scattered back to the detector. Taking the lengths of the detector, the corrector dipole, TAS and shielding wall together and allowing for some margin for connections and vacuum equipment, a minimum L^* of $45\,\text{m}$ is considered realistic.

In order to reduce the minimum β^*, the triplet magnets were lengthened by $50\,\%$ to a length of $31\,\text{m}$ for Q1 and Q3 and $26\,\text{m}$ for Q2a and Q2b. The relative length increase refers to both the $L^* = 36\,\text{m}$ lattice and the $L^* = 61\,\text{m}$ lattice, as they

Table 4.3: Crossing schemes with similar long range beam-beam effect.

Internal half crossing angle	experimental angle	external angle
110 µrad	−18 µrad	92 µrad
89 µrad	0 µrad	89 µrad
71 µrad	18 µrad	89 µrad
85 µrad (vertical)	± 18 µrad	85 µrad (vertical) ± 18 µrad (horizontal)

feature almost the same triplet length.

Due to the longer triplet, the distance between IP and separation dipole D1 increased. Consequently, more long range beam-beam encounters occur in the shared beam pipe. To keep the long range beam-beam tune shift ΔQ_lr constant, the normalized separation N_bb induced by the crossing angle must be increased. From Eq. (3.22)

$$\Delta Q_\mathrm{lr} \propto \frac{N_\mathrm{lr}}{N_\mathrm{bb}^2}.$$

and $N_\mathrm{lr} \propto \Delta s_{\mathrm{IP} \to \mathrm{D1}}$, we can deduce that N_bb must scale with the square root of the length increase. In the $L^* = 45\,\mathrm{m}$ lattice, this yields $N_\mathrm{bb} = 15.2\,\sigma$, corresponding to a half crossing angle of 89 µrad for the "ultimate" parameters with $\beta^* = 0.3\,\mathrm{m}$. This value needs to be adapted to the spectrometer and orbit corrector since they interfere with the separation: For a beam energy of 50 TeV, the integrated bending field of $B \cdot L = 10\,\mathrm{Tm}$ of the spectrometer corresponds to a bending angle of 60 µrad, the integrated field of $-7\,\mathrm{Tm}$ of the orbit corrector to -42 µrad, leaving an additional angle of 60 µrad -42 µrad = 18 µrad in the horizontal plane, called the "experimental angle". The experimental angle is to be added or subtracted to the internal crossing angle, i.e. the crossing angle at the IP. The resulting external crossing angle after the corrector dipole will either result in an unnecessarily large aperture need or in an increased long range beam-beam effect beam-beam tune shift. To avoid these consequences, the internal crossing angle needs to be scaled to keep the beam-beam effect constant. Crossing schemes with similar strengths of the beam-beam effect are listed in Table 4.3.

The considerable increase of the triplet magnet lengths led to aperture diameters of 205 mm in Q1 and 248 mm in Q2 and Q3. The option to use individual apertures was used to maximize the β^* reach as already discussed in Section 4.2. As expected from the scaling studies, the increase of triplet magnet lengths by 50 % increased the β^* reach: Fig. 4.10 shows the available beam stay clear for various ambitious β^* settings. When accepting a minimum beam stay clear of $12\,\sigma$, β^* can be pushed down to 0.05 m. This corresponds to the lowest β^* configuration with advantages for the luminosity production rate [44]. Alternatively, for the "ultimate" $\beta^* = 0.3\,\mathrm{m}$, the beam stay clear reaches $42\,\sigma$, a value much larger than necessary for collimation. The free aperture can be used for additional shielding to reduce the radiation load further. As stated above, the ideal goal is to survive an integrated luminosity of $17\,500\,\mathrm{fb}^{-1}$.

The increase of the beam stay clear from $17\,\sigma$ in the other L^* options for $\beta^* = 0.3\,\mathrm{m}$ to $42\,\sigma$ is disproportionately larger than expected from the 50 % length increase of the quadrupoles (assuming L^* has a minor impact on the beam stay clear). This is mainly due to the larger aperture and the subsequent smaller relative reduction
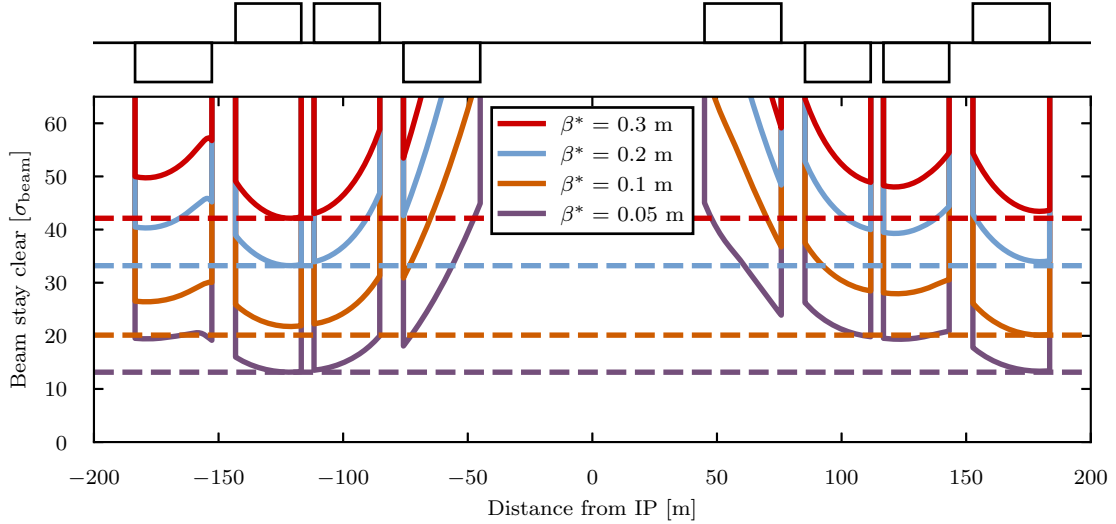
Figure 4.10: Beam stay clear of the $L^* = 45\,\mathrm{m}$ lattice for different values of β^*. Allowing a beam stay clear of only $12\,\sigma$, the aperture allows a β^* down to $0.05\,\mathrm{m}$. Alternatively, the "ultimate" baseline goal of $\beta^* = 0.3\,\mathrm{m}$ leaves a beam stay clear of $42\,\sigma$, allowing thicker shielding. The beam stay clear was calculated with $15\,\mathrm{mm}$ of shielding in every magnet.

of the free aperture by shielding and other layers (see Table 4.2).

In Fig. 4.11 the $\beta^*_{\min}$ scalings of both the $L^* = 36\,\mathrm{m}$ and $L^* = 61\,\mathrm{m}$ lattices are plotted again for a beam stay clear of $12\,\sigma$. For the $L^* = 45\,\mathrm{m}$ lattice, the minimum β^* is shown for a scaling factor of 1.5 which corresponds to the longitudinal scaling of the triplet length (from both lattices) but not for L^*. The good agreement with the β^* scaling of both lattices confirms the observation that the minimum β^* (or alternatively, the beam stay clear) is determined by the triplet length but not by L^*.

The radiation load in the new lattice will be influenced by the spectrometer dipole. In order to compare the $L^* = 45\,\mathrm{m}$ scenario with the previous lattices, the spectrometer was switched off for the first studies. The upper plot in Fig. 4.12 shows the resulting peak doses for horizontal crossing, the lower plot for vertical crossing. Comparing the maximum values at the end of Q1 with the previous results in Fig. 4.7 shows a reduction of the peak dose by $44\,\%$ with respect to the $L^* = 36\,\mathrm{m}$ lattice and $26\,\%$ with respect to the $L^* = 61\,\mathrm{m}$ lattice. This is again caused by a larger coil aperture and a lower gradient. With a peak dose of $20\,\mathrm{MGy}$ per $3000\,\mathrm{fb}^{-1}$ for horizontal crossing, this is close to the minimum goal of $30\,\mathrm{MGy}$ per $5000\,\mathrm{fb}^{-1}$. The plots also show the dose distributions with the experimental spectrometer and its compensator switched on. The first studied case corresponds to an internal half crossing angle of $110\,\mathrm{\mu rad}$ and an experimental angle of $-18\,\mathrm{\mu rad}$ (see Table 4.3). This was considered the worst case scenario in terms of dose, because here debris particles have the largest initial transverse momentum and largest offset when entering Q1. As expected, the load in Q1 increased significantly. Apart from the larger crossing angle, this is mainly due to the increased capture of negative pions that are deflected further outwards by the combined effects of spectrometer and corrector dipole, as well as by the field in Q1 [45]. The inverted spectrometer option
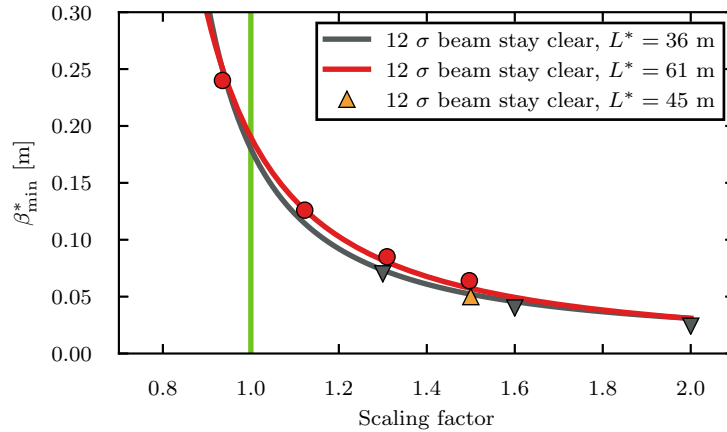
Figure 4.11: Scaling of the minimum β^* for a beam stay clear of $12\,\sigma$ from Fig. 4.8. For the $L^* = 45$ m lattice the scaling factor refers to the triplet length only.
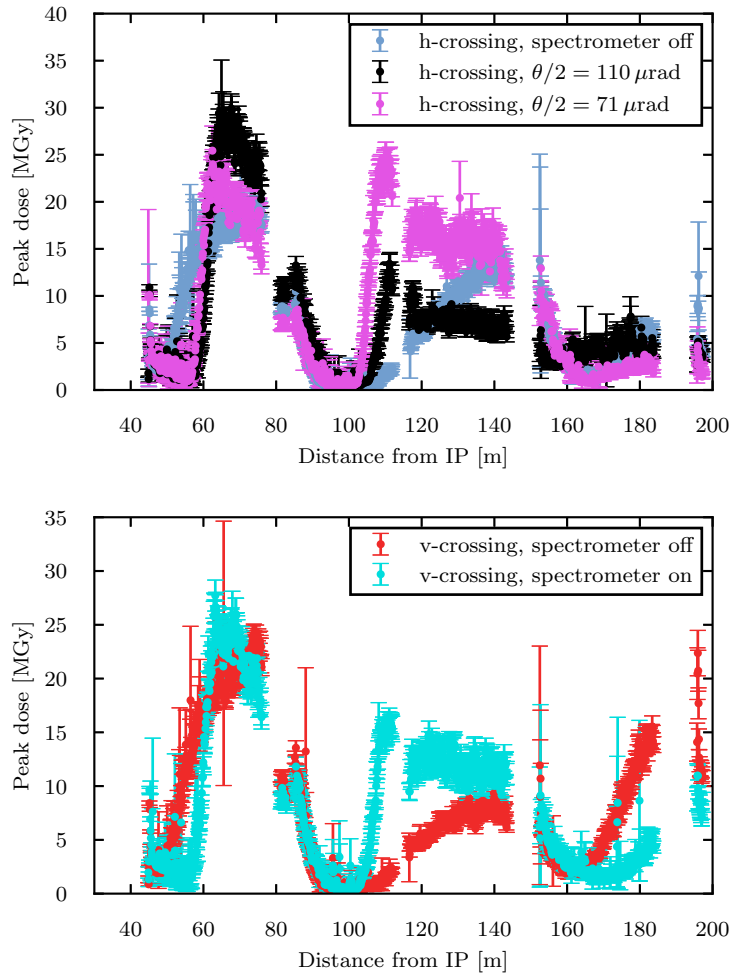

Figure 4.12: Peak dose distributions per $3000\,\mathrm{fb}^{-1}$ for the $L^* = 45$ m scenario with and without spectrometer. The strong early deflection of the debris due to the spectrometer leads to a significant peak dose increase, most notably in Q1. Data from [4].
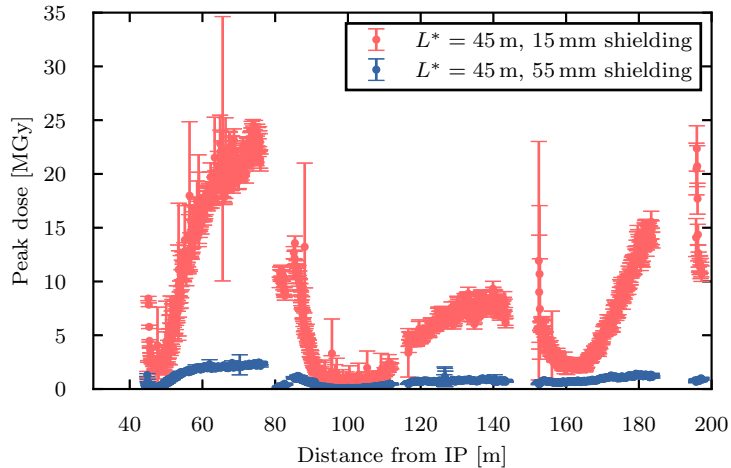
Figure 4.13: Peak dose distributions $L^* = 45\,\mathrm{m}$ for vertical crossing with a shielding thickness of $55\,\mathrm{mm}$ for an integrated luminosity of $3000\,\mathrm{fb}^{-1}$. The massive increase in shielding reduced the dose by a factor of 10. Data from [4].

for horizontal crossing corresponds to the internal half crossing angle of $71\,\mathrm{\mu rad}$ and $18\,\mathrm{\mu rad}$ experimental angle. As expected, the load in the triplet is smaller for this spectrometer orientation as the initial horizontal offset of the debris is smaller. For the vertical crossing, the orientation of the horizontal spectrometer has no impact on the longitudinal dose distribution, since it does not influence the crossing angle. However the azimuthal distribution of the load is affected significantly, opening up opportunities for crossing angle gymnastics for radiation mitigation as described in [45].

As an exploratory study towards a sustainable integrated luminosity of $17\,500\,\mathrm{fb}^{-1}$, the shielding inside the triplet magnets was increased to $55\,\mathrm{mm}$ thickness. With this amount of shielding the beam stay clear reduced to $15.5\,\sigma$ at a minimum β^* of $0.2\,\mathrm{m}$. While this is still lower than the "ultimate" parameter, it considerably limits the luminosity that the long triplet could offer beyond that. The resulting peak doses are plotted in Fig. 4.13. Compared to the case with $15\,\mathrm{mm}$ of shielding, the maximum peak dose was reduced by a factor of 10. This means, if the available aperture offered by the length increase is used for shielding, the triplet could already survive the full integrated lifetime luminosity while offering some limited margin in β^* or beam stay clear.

Chapter 5

Radiation mitigation by splitting Q1

As discussed above, the required cool-down times for the irradiated magnets make the survival of the whole FCC-hh lifetime (equivalent to $17\,500\,\mathrm{fb}^{-1}$) desirable. Apart from the $L^* = 45\,\mathrm{m}$ option with very thick shielding, all lattices presented so far exceeded even the minimum goal of a maximum peak dose of $30\,\mathrm{MGy}$ per operational cycle of $5000\,\mathrm{fb}^{-1}$ (corresponding to $18\,\mathrm{MGy}$ per $3000\,\mathrm{fb}^{-1}$). Those high integrated luminosities will require optimization in the radiation protection. Various methods have been proposed, including more radiation resistant materials in the magnets as well as optimized running scenarios in which the radiation is distributed over different areas. As the highest peak dose has always appeared around the end of Q1, another option is to distribute the radiation load more evenly over the length of the magnet. This can be done by splitting Q1 into two different quadrupoles with individual apertures and subsequently individual gradients. Due to the parameterization presented in this chapter, the feedback of this method on the beam optics is minimized. Unlike a simple increase of the shielding thickness, the beam stay clear is not reduced by the Q1 split. The basic principle of this method makes it applicable independently of L^* and triplet length.

5.1   Method and parameterization

The goal of the split Q1 is to reduce the radiation load in the first triplet magnet with minor impact on the optics. The overall effect of Q1 on the optical functions should therefore stay the same. Therefore, the total integrated quadrupole strength will be kept constant:

$$\int_{\mathrm{Q1}} k \, \mathrm{d}s = const. \tag{5.1}$$

Furthermore, the length L of Q1 is kept constant. This way, the geometry remains constant and the change of the β functions in the triplet will be kept minimal. The lengths of Q1a and Q1b are defined by the ratio λ:

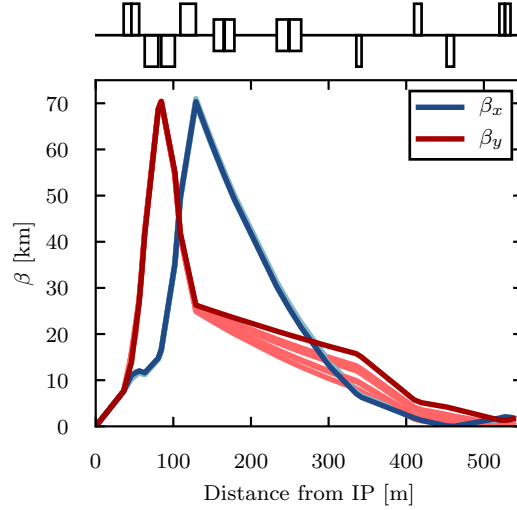$$L_{\mathrm{Q1a}} = \lambda \cdot L_{\mathrm{Q1b}} \tag{5.2}$$

Figure 5.1: Change of the optics from unsplit (dark) to split (light) Q1 for $r_\mathrm{g} = 1.2$ and 1.5, each with $\lambda = 0.3, 1.0, 3.0$. No rematching was performed.

Since $L_\mathrm{Q1a} + L_\mathrm{Q1b} = L$, we can deduce

$$L_\mathrm{Q1a} = L \cdot \frac{\lambda}{1 + \lambda} \tag{5.3}$$

$$L_\mathrm{Q1b} = \frac{L}{1 + \lambda} \ . \tag{5.4}$$

In order to have different apertures, the gradients must be different. We introduce the ratio of the gradients r_g with

$$k_\mathrm{Q1a} = r_\mathrm{g} \cdot k_\mathrm{Q1b}, \tag{5.5}$$

so the gradient of Q1a is r_g times stronger than the gradient of Q1b. The unsplit case corresponds to $r_\mathrm{g} = 1$. Since the integrated strength should be constant, we can deduce

$$k_\mathrm{Q1a} \cdot L_\mathrm{Q1a} + k_\mathrm{Q1b} \cdot L_\mathrm{Q1b} = k \cdot L \ . \tag{5.6}$$

Inserting Eqs. (5.2) and (5.5) in (5.6) yields

$$k_\mathrm{Q1a} = k \frac{1 + \lambda}{\frac{1}{r_\mathrm{g}} + \lambda} \tag{5.7}$$

$$k_\mathrm{Q1b} = k \frac{1 + \lambda}{1 + r_\mathrm{g}\lambda} \ . \tag{5.8}$$

Thus, in a given lattice with given k and L two degrees of freedom remain for the radiation load minimization: r_g and λ. For optics adjustments, the parameter k is used.

In Fig. 5.1, the variations of the β functions for different values of r_g and λ are shown. As intended, they do not change remarkably within the triplet, even without rematching. Again we use the aperture-gradient model of Eq. (3.21):

$$r = \frac{e}{p} \frac{B_\mathrm{max}}{k}$$

48

For this study, B_{max} was set to $11\,\mathrm{T}$. Inserting Eqs. (5.7) and (5.8) into Eq. (3.21) yields

$$r_{\mathrm{Q1a}} \;=\; r_{\mathrm{Q1}}\frac{\frac{1}{r_{\mathrm{g}}}+\lambda}{1+\lambda} \tag{5.9}$$

$$r_{\mathrm{Q1b}} \;=\; r_{\mathrm{Q1}}\frac{1+r_{\mathrm{g}}\lambda}{1+\lambda}\;, \tag{5.10}$$

where r_{Q1} is the coil aperture of the unsplit Q1. For the goal of reducing the radiation load in Q1b, r_{g} will be larger than 1 as this decreases the gradient of Q1b and allows for a larger aperture.

To minimize the radiation load, it is best to insert as much shielding as possible without reducing the minimum beam stay clear. On the assumption that the beam size only changes negligibly, an increase in coil aperture in Q1b allows to increase the shielding thickness by the same amount. Similarly, in Q1a the shielding has to be reduced when the coil aperture is shrinking. It should be noted that in the unsplit case, the shielding thickness is constant along Q1 and determined by the beam stay clear at the end. This means, at the entrance of Q1, the shielding is not as thick as it could be without compromising the beam stay clear, as illustrated in Fig. 5.2. For an unsplit Q1, this is irrelevant as the highest dose occurs at the end, so additional shielding at the entrance would have no benefit. For the Q1 split, Q1a will receive larger doses, so the shielding will be chosen as thick as possible. Consequently, when directly comparing the split and the unsplit case, the shielding thickness of Q1a can in fact increase.
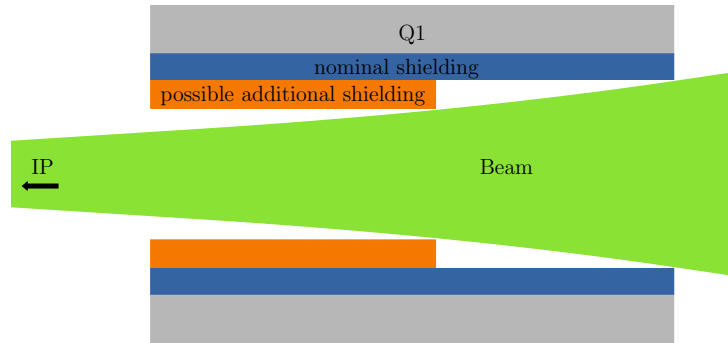

Figure 5.2: Illustration of the possible shielding thickness at the entrance of Q1 (orange) compared to the actual shielding thickness (blue) in the unsplit case.

5.2 Effects of splitting Q1

In Fig. 5.3 the peak dose of the unsplit Q1 is illustrated by a black line. The dotted red and green lines qualitatively show the expected dose for a split Q1: for a stronger gradient in Q1a caused by a larger r_{g}, the coil aperture will become smaller, thus increasing the dose. Since the gradient is larger, debris particles are defocused stronger than before, giving an additional effect on the radiation load that increases with the distance from the IP. Due to the smaller coil aperture, the

shielding thickness that can be placed in Q1a will become smaller when increasing r_g, resulting in an even larger radiation load in the magnet coils. However, as discussed above, the shielding could in principle be thicker closer to the IP compared to the unsplit case. Placing the most possible shielding in Q1a may therefore counteract the increased radiation dose at first.
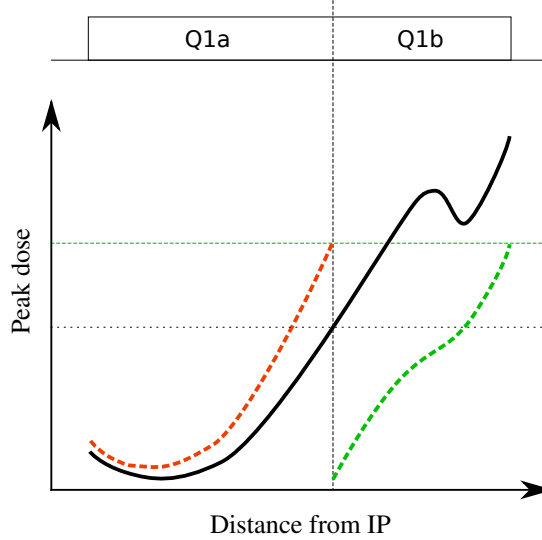

Figure 5.3: Qualitative sketch of the peak dose in the Q1. The horizontal axis extends over the length of Q1(a/b) shown at the top. The black line describes the peak dose for an unsplit Q1. The expected changes for splitting Q1 are shown by the dashed red and green lines.

In Q1b the gradient is decreased, giving a larger possible coil aperture. The retracted coils will be exposed to less radiation. The entrance of Q1b should be completely protected by the shielding in Q1a while the exit is more exposed to debris particles deflected outwards by the quadrupole field. Since the beam size is intended to be kept roughly the same as in the unsplit Q1, the larger coil aperture also leaves space for thicker shielding, decreasing the dose further.

A counteracting effect comes from the stronger defocusing in Q1a, resulting in debris particles already bent further outwards after exiting Q1a. While the effect of this earlier defocusing on the beam size is kept small, its effect on debris particles with considerably lower momentum will be stronger.

5.3 Effects of the free parameters

First, the effect of the gradient ratio r_g on the radiation load will be studied. For $r_g = 1$ we have the initial situation of an unsplit Q1. A lower ratio is undesirable since it will reduce the aperture at the end of Q1, the point that already features the highest radiation load. As discussed before, increasing r_g will increase the peak dose in Q1a and reduce the one in Q1b. The optimum r_g is reached at the point where the highest doses in both magnets are the same, meaning both magnets can sustain the same integrated luminosity (green dotted horizontal line in Fig. 5.3). As discussed earlier, the radiation load in Q1a can only increase. Thus, the load at the end of Q1a for $r_g = 1$ (black dotted horizontal line in Fig. 5.3) is a lower

limit for the achievable maximum peak dose. From this point of view, it is clear that Q1a should be rather short, i.e. λ should be rather small. This, however, limits the aperture gain achievable in Q1b due to r_{g} (see Eq. (5.10)). Thus we can expect the optimum split position to be rather in the center of Q1 (λ around 1) than towards the ends (i.e. large or small λ). With this in mind, a good strategy for the optimization of the peak dose is to choose a set of values for λ around 1 and optimize r_{g}.

5.4 Simulation and results

To explore the effect of splitting Q1, the FCC-hh interaction region lattice with $L^* = 36\,\mathrm{m}$ was used. For the first simulations of the radiation load, λ was set to 1. In order to get a realistic design, a gap of $0.64\,\mathrm{m}$ between Q1a and Q1b was introduced. To compensate the slight change in focusing, the triplet was rematched. As a result, the relative change of k of Q1 was less than 10^{-4}, while the strengths of Q2a/b and Q3 stayed constant. Thus, the radiation optimization has a negligible impact on the beam optics, the minimum beam-stay-clear was unchanged as it was intended by the parameterization.

Figure 5.4 shows the peak doses obtained with FLUKA for the lattice with split Q1 for the cases $r_{\mathrm{g}} = 1.1$ (V1) and $r_{\mathrm{g}} = 1.2$ (V2). Moreover, the unsplit case with a coil aperture of 100 mm is shown, considering two shielding thickness options: 15 mm and 20 mm. There is a good agreement of the resulting doses in Q1a and Q1b with the qualitative predictions in Fig. 5.3. The dose in Q1a did not increase much, because the shielding in this region actually increased as discussed earlier. For V2, the maximum peak doses in Q1a and Q1b are the same, thus the optimum was found. The optimization in r_{g} only took two iterations. As the maximum peak dose is now at the beginning of Q2a and the end of Q3, further optimization in λ was omitted. The maximum peak dose in Q1 was decreased from about $27\,\mathrm{MGy}$ (unsplit, $20\,\mathrm{mm}$ shielding) to about $18\,\mathrm{MGy}$, which is a reduction of $\approx 33\,\%$. This was achieved with a shielding thickness of $21\,\mathrm{mm}$ / $24\,\mathrm{mm}$ and a coil aperture of $92\,\mathrm{mm}$ / $110\,\mathrm{mm}$ in Q1a and Q1b respectively. In the rest of the triplet the assumed shielding thickness and coil aperture are $15\,\mathrm{mm}$ and $115\,\mathrm{mm}$. Assuming an acceptable dose of $30\,\mathrm{MGy}$, the integrated luminosity that Q1 could survive increased to $5000\,\mathrm{fb}^{-1}$. This corresponds to the minimum goal for a five-year operation cycle at ultimate parameters [15] allowing to run the full period without replacing Q1.

In order to take full advantage of the dose reduction in Q1, the radiation load in the rest of the triplet needs to be decreased to similar levels. An optimized operational scenario that runs with horizontal crossing $50\,\%$ of the time and with downward/upward vertical crossing $25\,\%$ of the time each, can distribute the radiation azimuthally. This approach has shown to be able to reduce the peak doses in the rest of the triplet to about $30\,\mathrm{MGy}$ per $4500\,\mathrm{fb}^{-1}$ in the $L^* = 36\,\mathrm{m}$ lattice [45], coming close to the targeted values. In the presence of a horizontal spectrometer, as in the case in the $L^* = 45\,\mathrm{m}$ lattice, the effectiveness of the crossing angle variation is limited. Instead, alternating the spectrometer polarity is expected to have similar effects [45].

As mentioned before, surviving $5000\,\mathrm{fb}^{-1}$ can only be considered the minimum goal, the number of survivable high luminosity runs will potentially determine the
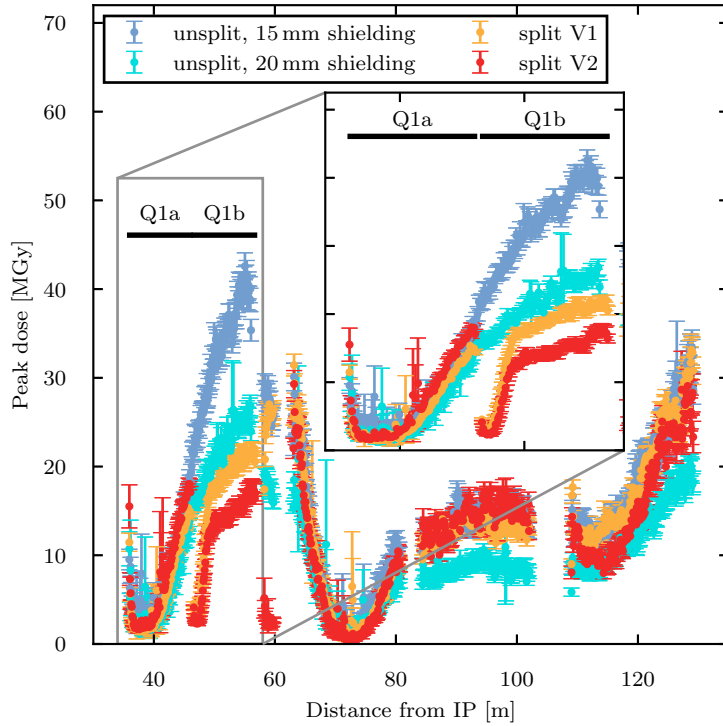
Figure 5.4: Peak doses of the triplet with unsplit and split Q1. For an optimized Q1 split (V2), the maximum peak dose is reduced by about 33% with respect to the unsplit 20 mm shielding case. Data from [4].

long term performance of FCC-hh. Further improvements of the radiation protection are required to push the survivable luminosity towards $17\,500\,\mathrm{fb}^{-1}$, the lifetime goal of FCC-hh, and avoid prolonged shut-downs for magnet exchanges entirely.

Chapter 6

Arc integration

In the previous chapter a strategy to maximize the luminosity by decreasing β^*_{min} was derived that requires to increase the triplet lengths until limited by Dynamic Aperture (DA) or chromaticity. These two properties must now be studied in order to find the limit for the maximum triplet length. As the chromaticity limit depends on the correction in the arcs and DA requires tracking studies, the interaction region must be integrated in the whole ring lattice.

So far, the considerations on the β^* reach only focused on the final focus system and its aperture. For these studies, the β functions around the first quadrupole of the matching section Q4 were matched to be below β_{max} and the α functions to be positive. While this is a reasonable guess based on the optics on LHC and HL-LHC, it is still necessary to match the optical functions of the triplet to those of the arcs. Similar to LHC and HL-LHC, a matching section consisting of four quadrupoles, as well as three quadrupoles of the dispersion suppressor and three trim quadrupoles of the first arc cell are used. It is necessary to match β_x, β_y, α_x, α_y, μ_x, μ_y, as well as D_x and D'_x created by the separation and recombination dipoles D1 and D2 between the triplet and Q4. At the same time, the dispersion suppressors feature full bend dipoles identical to the arc dipoles, like in the LHC. Including the beam screen, the free aperture diameter is thus limited to 30 mm. To avoid aperture bottlenecks, a maximum β function of 700 m was set as a limit from the last quadrupole of the matching section Q7 on. This will keep enough margin to account for mechanical tolerances.

Like the LHC and HL-LHC optics, left and right sides of FCC-hh triplet region are antisymmetric, meaning same powering with opposite polarity for the quadrupole left and right from the IP. This results in identical optical solutions for both beams simultaneously. While the arc dispersion has the same sign left and right, the dispersion introduced by the separation and recombination dipoles D1 and D2 breaks the left-right symmetry of the IR as it has opposite signs on either side. Thus both sides of the IR need to be matched. The shared aperture triplet is exempt and remains perfectly antisymmetric to keep the solution viable for both beams.

6.1 Matching procedure

The matching of the IR optics to the arc optics is done like for LHC and HL-LHC using a matching section consisting of the four quadrupoles Q4-Q7, the first three quadrupoles of the dispersion suppressor Q8-Q10 and three trim quadrupoles in

the first arc cell (QT11-QT13) on each side. In order to guarantee correct optics at the IP and to facilitate faster convergence of the matching algorithm, the IR was not matched as a whole from the left side to the right, but instead in two independent steps from the IP to the right arc and from the IP to the left arc. As the triplet was optimized for best aperture use in section 4.2, the triplet magnets were not used for the arc integration. Consequently, the triplet optics stayed the same and the antisymmetry of their β functions was preserved by the two separate matchings. After matching the right side, the resulting quadrupole strengths with inverted polarity were used as a starting point for the matching of left side. This is a reasonable guess due to the antisymmetry of both the triplet optics and the arc optics with respect to the IP. However, the asymmetric dispersion values introduced by the separation and recombination dipoles D1 and D2 (see e.g. Fig. 6.1) still make rematching necessary.

The β and α functions as well as D_x and D'_x at the end of the dispersion suppressor are given by the periodic solution of the arc FODO cells. The phase advance on the left side was chosen to be $\Delta\mu_x = 9/4\pi$ and $\Delta\mu_y = 3\pi$ from the IP to the first arc sextupole (and vice versa on the right side), like in the Achromatic Telescopic Squeezing (ATS) scheme foreseen for HL-LHC (see. [46]). While the telescopic squeeze is not planned to be used in FCC-hh, the phase advance, together with a phase advance of $\pi/2$ in the arc FODO cells, allows the use of a similar spurious dispersion correction scheme. When the beams are colliding with a crossing angle, they enter the triplet magnets with a transverse offset from the magnetic axes and experience a dipolar component from the feed down effect. This results in an additional dispersion, called the spurious dispersion. While the spurious dispersion is small and not corrected in the LHC, the stronger focusing in the HL-LHC triplet creates significantly larger dispersion, making a correction necessary. Likewise, in FCC-hh the dispersion beating reached amplitudes of $D_x = 20\,\mathrm{m}$ compared to $2.4\,\mathrm{m}$ peak dispersion in the arcs, calling for correction as well. The crossing angle is a parameter that must be easy to change during operation, so a matching with the quadrupoles in the matching section and DS is impractical as they will change the beam optics as well. Instead, two options for a dedicated correction scheme are currently considered: HL-LHC-like or SSC-like. The spurious dispersion correction scheme in the HL-LHC applies orbit correctors in the short arcs adjacent to the IP. They create orbit bump that result in further dispersion from feed down effects from the arc quadrupoles. The orbit bump is then adjusted to cancel out the spurious dispersion from the triplet. An alternative approach has been developed at the Superconducting Super Collider (SSC) [47]: quadrupole pairs (for horizontal spurious dispersion) and skew quadrupole pairs (for vertical spurious dispersion) with opposite polarity are used to match the respective spurious dispersion to the horizontal dispersion in the arcs without affecting the betatron motion. The necessary phase advance from IP to the quadrupole pairs for effective cancellation is compatible with the phase advance of the ATS scheme of HL-LHC. Thus, both dispersion correction schemes can be implemented in the same lattice.

6.2   Collision optics

The collision optics are optimized for luminosity production at top energy. First, the baseline parameter set with $\beta^* = 1.1\,\mathrm{m}$ and the "ultimate" parameters with

$\beta^* = 0.3$ m are considered. Both options have been matched to the arcs for the $L^* = 36$ m, 45 m and 61 m lattices. In order to converge to an optical solution fast, the phase advance constraints have been omitted in this first matching iteration. For the $L^* = 36$ m lattice with "ultimate" setting of $\beta^* = 0.3$ m the resulting optics are shown in Fig. 6.1c. For this lattice the optical functions could be matched for a straight section length (distance from left Q7 to right Q7) of 1070 m without problems.

It is important to see how much further the optics can be pushed beyond the "ultimate" β^*. From Fig. 4.5 we can see that the triplet apertures of the $L^* = 36$ m lattice can accommodate a β^* of about 0.2 m while leaving $12\,\sigma$ beam stay clear. The matching section is flexible enough to match this β^* to the arcs. The corresponding optics are shown in Fig. 6.1d.

(a) Left side, $\beta^* = 0.3$ m.

(b) Right side, $\beta^* = 0.3$ m.

(c) Whole interaction region with $\beta^* = 0.3$ m.

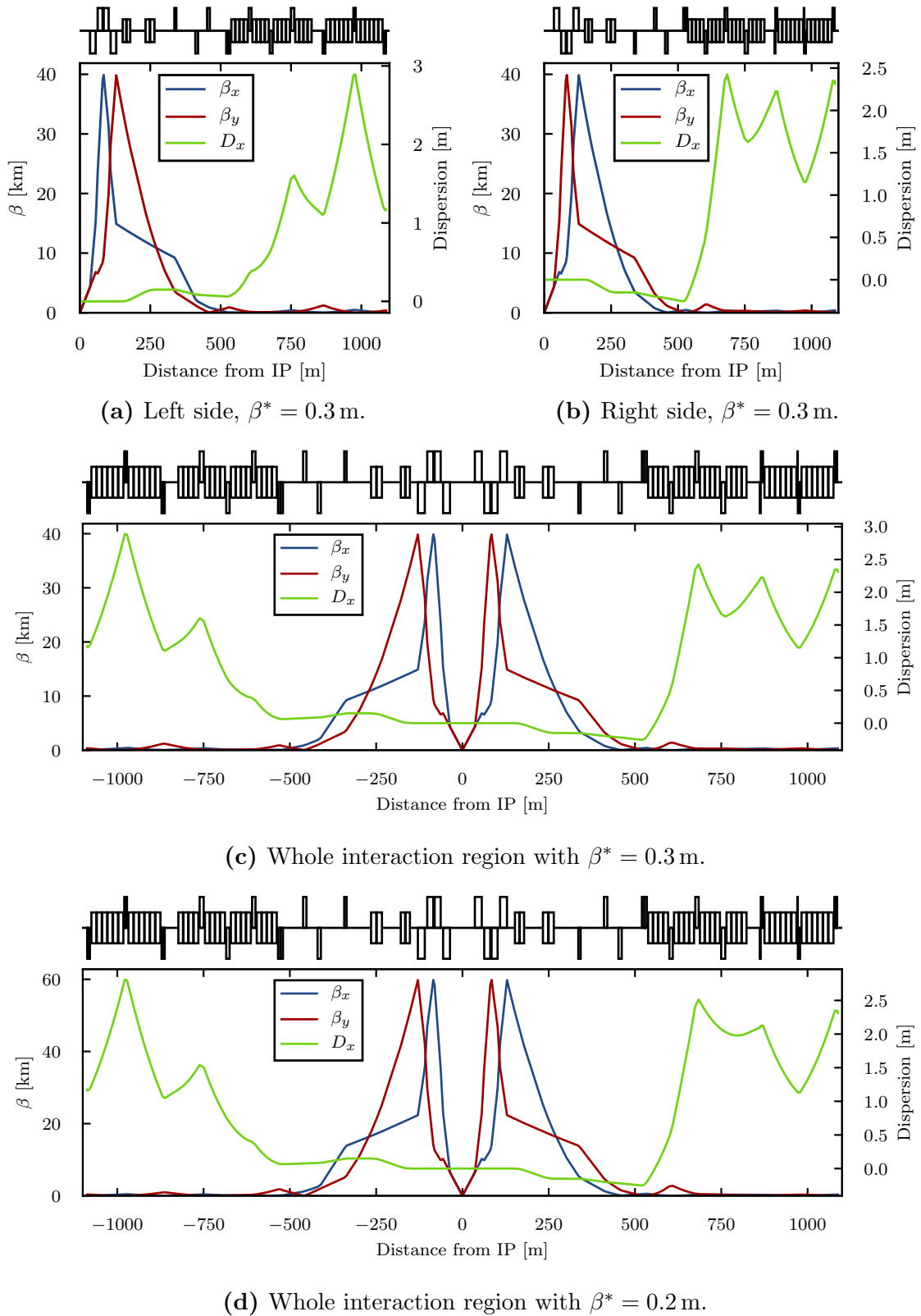**(d)** Whole interaction region with $\beta^* = 0.2$ m.

Figure 6.1: Interaction region of the $L^* = 36$ m lattice with $\beta^* = 0.3$ m and 0.2 m matched to the arcs. The dispersion created by the separation dipoles 180 m from the IP causes asymmetric optics in the matching sections and dispersion suppressors.

6.3 Injection optics

At injection energy, different optics are required in the interaction region. The reason is that the transverse emittance ϵ of a proton beam depends on the energy.

$$\epsilon \propto \frac{1}{\gamma_{\mathrm{L}}} \tag{6.1}$$

with γ_{L} the relativistic Lorentz factor. For any given optics, the beam size is therefore significantly larger at injection energy than at collision energy. As the triplet already is the aperture bottleneck at collision energy, it is clear that the maximum beta functions must be reduced for injection. This can be achieved by increasing β^*. According to the Liouville theorem, a beam with a larger beam size is less divergent, which results in smaller beam sizes in the triplet. This has already been shown in Eq. (3.20), where

$$\beta(s_{\mathrm{triplet}}) \propto \frac{1}{\beta^*}. \tag{6.2}$$

The baseline option for the injector [15, 48] is the reuse of the present LHC equipped with faster ramping power converters operating the main dipoles at 3.6 T to provide an injection energy of 3.3 TeV. As the LHC is complex and expensive to operate, other, more reliable injector options are a superferric booster in the same tunnel as FCC, also injecting at 3.3 TeV, or a superconducting injector in the SPS tunnel, the current injector for LHC. The latter could only provide protons with an injection energy of 1.5 TeV, limited by the bending radius and the strengths of the dipole magnets. For the injection optics derived in this work, the 3.3 TeV options are assumed, with a dedicated section on the implications of 1.5 TeV injection energy.

As a first guess for the injection optics, the quadrupole strengths k of the triplet magnets were set to be constant. This is consistent with the HL-LHC squeeze, where the triplet gradients are kept constant within a few percent in order to limit hysteresis effects and thus field errors in the triplet [49], that have a significant impact on the dynamic aperture at collision optics for LHC [50, 51].

To get reasonable injection optics, β^* was increased stepwise, the triplet rematched accordingly until the beam stay clear was sufficient. This resulted in $\beta^* = 4.6\,\mathrm{m}$ for a beam stay clear of $15\,\sigma$. The corresponding optics are shown in Fig. 6.2.

With the introduction of collision and injection optics a new constraint comes up. The unipolar power supplies for the quadrupoles in the matching section (i.e. Q4-Q10) in the LHC can provide a minimum output current of $2\,\%$ of their nominal current [26, Section 10.3]. Assuming the same technology for FCC-hh, this means the lowest and highest gradient for any magnet must differ by a maximum factor of 50. It further means that the magnets cannot change their focusing property from focusing to defocusing or vice versa over the squeeze. The trim quadrupoles QT11-QT13 are equipped with bipolar power supplies but feature a lower maximum gradient. The quadrupole gradients for the different optics are plotted in Fig. 6.3 against the corresponding β^*. The ramp is modeled as a simple gradient increase with the energy at the largest β^*. While most gradient ranges are fine, we can see that the left Q6 is too weak at the collision settings $\beta^* = 0.3\,\mathrm{m}$ and $\beta^* = 0.2\,\mathrm{m}$. Another observation is the fact that Q7 and Q8 have very high gradients, despite the fact that Q7 is already made up of two subsequent quadrupoles. The high gradients
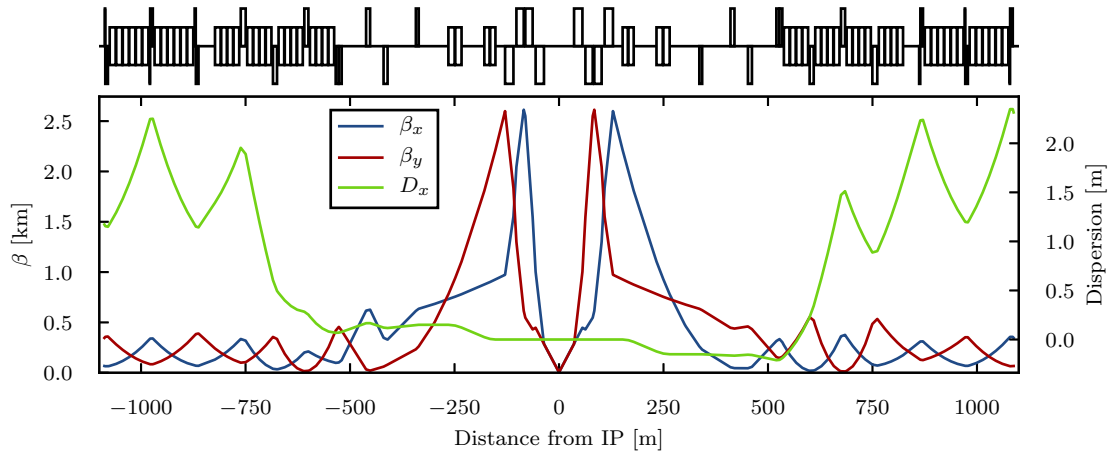
Figure 6.2: Interaction region of the $L^* = 36\,\text{m}$ lattice with $\beta^* = 4.6\,\text{m}$.

in Q7 and low gradients in Q6 are known to be limiting factors in the LHC and HL-LHC that have similar IR layouts [46, 49].

The currently assumed gradient limits are $400\,\text{T/m}$ for the main quadrupoles [52] and $150\,\text{T/m}$ for the trim quadrupoles. These limits are exceeded not only by Q7 and Q8 but also by the trim quadrupoles QT12 and QT13. However, this is not considered a problem because unlike the arc FODO cells, the matching section and the dispersion suppressor have relaxed spacial constraints (see e.g. the drift space in front of Q11 in the DS). This means that lengths and -if necessary- position of the magnets can be adjusted in later design iterations to get gradients below the limit.

In order to limit the gradient range of Q6, rematching of the optics is necessary. This was done for both low-β^* optics where Q6 is too weak. For these optics, the gradient of Q6 was set to the minimum possible value and kept constant while the other magnets were rematched. As the weak Q6 only has a small effect on the optics, matching was possible.

In the process of rematching to get a gradient range of a factor lower than 50 for Q6, the phase advance constraints were changed from the ad-hoc values resulting from the first matched optics to values compatible with the ATS optics scheme in HL-LHC [46] as described earlier. This is necessary to correct the spurious dispersion coming from the crossing angles and the subsequent orbit excursion in the triplet. Furthermore, in order to investigate injection optics with even more relaxed beam stay clear, a β^* of $6.0\,\text{m}$ was matched (see Fig. 6.4), providing a beam stay clear of $18\,\sigma$. The resulting gradients are shown in Fig. 6.5. The gradients for all magnets are now below a factor of 50. Furthermore, the maximum strengths of Q7, Q8 could be lowered, coming closer the the $400\,\text{T/m}$ limit, thus reducing the need for increased lengths. QT12 and QT13 on the other hand still are very strong, requiring a considerable length increase. This lead to a change of the lattice of the dispersion suppressors, where the lengths of the trim quadrupoles were increased by a factor of 4, bringing the maximum gradients below the limit.

While the gradients and gradient ranges shown in Fig. 6.4 are feasible with the changes mentioned above, it should be noted that individually build power supplies for every magnet are costly. To limit the costs, a real machine will feature a number of magnet types combined with a number of power supply types. The limited number
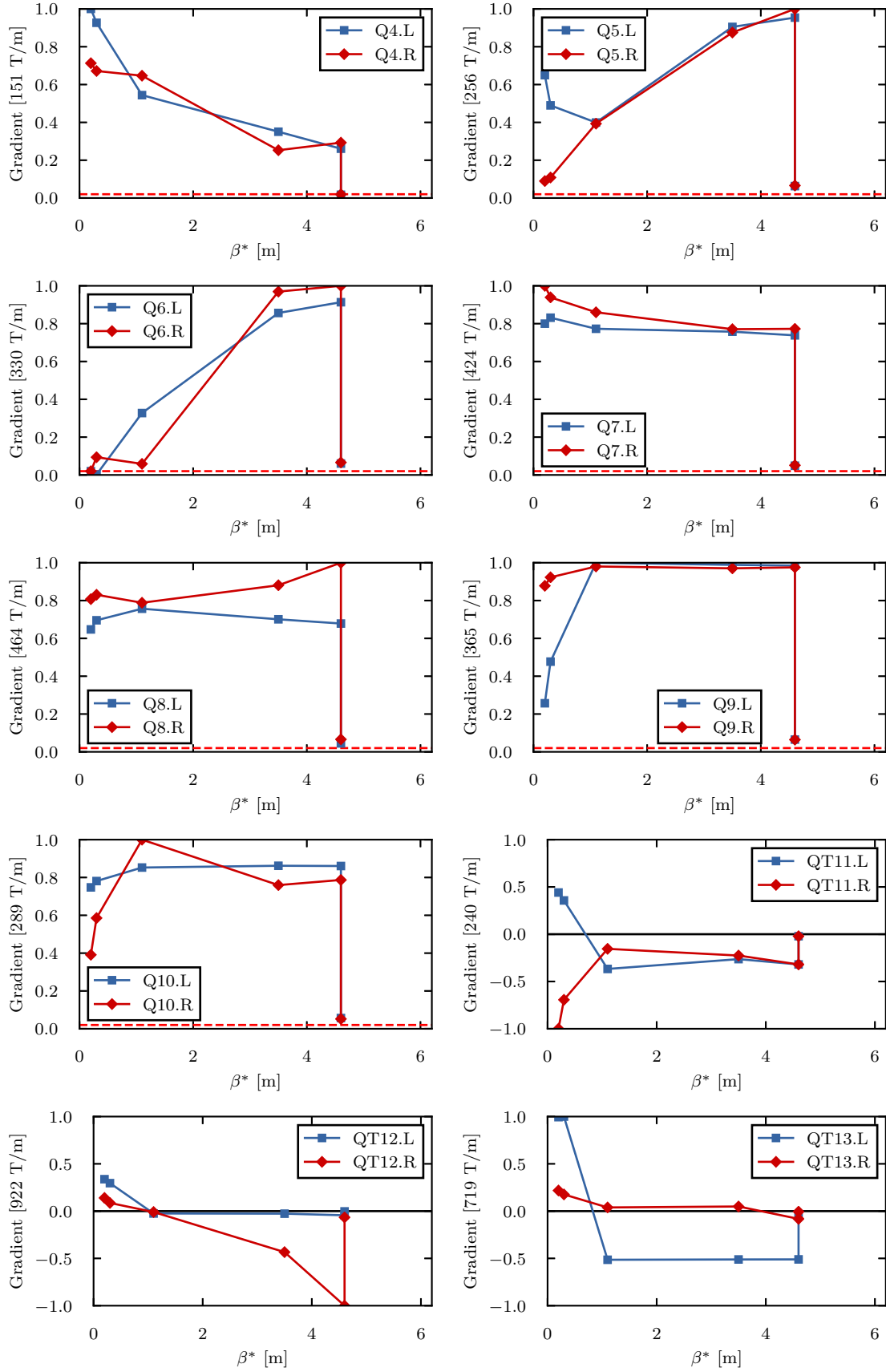
Figure 6.3: Variation of the matching quadrupole gradients in the $L^* = 36\,\text{m}$ lattice during transition from injection to collision optics. The gradient increase at $\beta^* = 4.6\,\text{m}$ represents the ramp. The red dashed line indicates the lower gradient limit of $2\,\%$ of the maximum gradient.
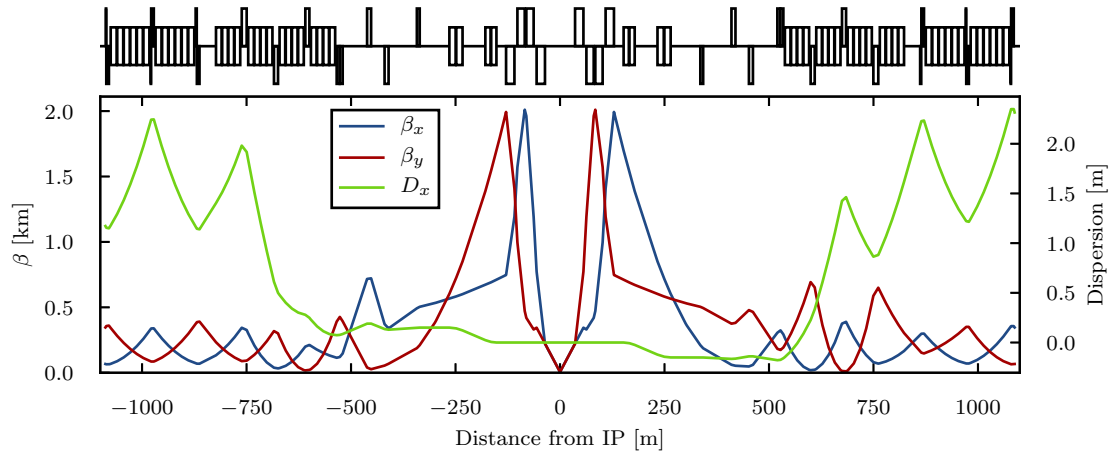
Figure 6.4: Interaction region of the $L^* = 36\,\text{m}$ lattice with $\beta^* = 6.0\,\text{m}$.

of possible combinations, resulting in a limited number of nominal gradient limits of the different quadrupoles, will make a larger gradient range necessary in order to make the squeeze shown in Fig. 6.4 possible.

The corresponding gradients for the $L^* = 45\,\text{m}$ and $L^* = 61\,\text{m}$ lattices are shown in Fig. A.1 and A.2 in the appendix. They show no new issues with the ranges except for Q6 in the $L^* = 61\,\text{m}$ lattice that gets too weak at low β^*. A work-around for this configuration, the combined ramp, will be explained later.
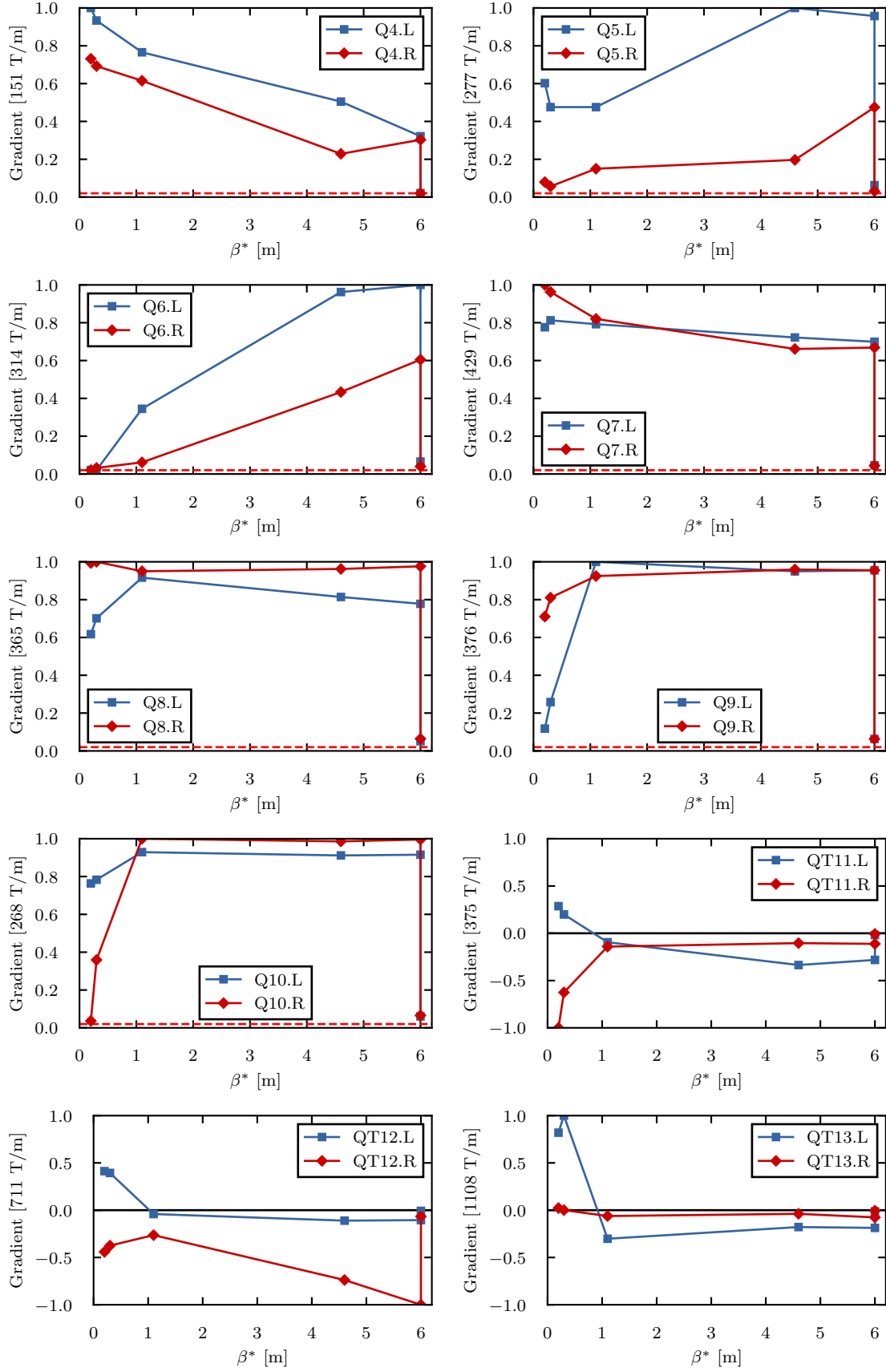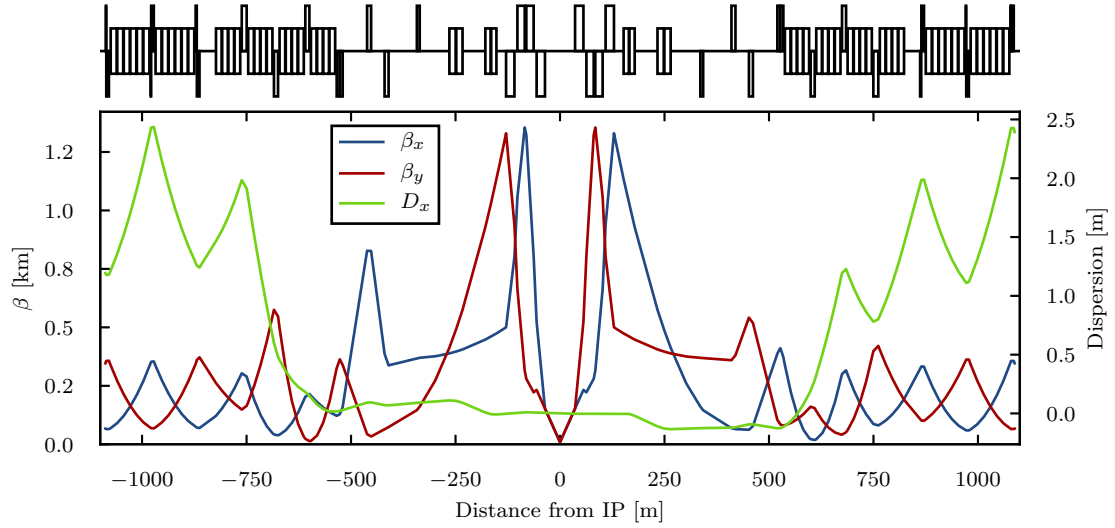
Figure 6.5: Variation of the matching quadrupole gradients in the $L^* = 36\,\mathrm{m}$ lattice during transition from injection to collision optics. The ramp is modeled as a simple gradient increase at $\beta^* = 6\,\mathrm{m}$.

6.4   1.5 TeV as injection energy

The previous injection optics were chosen in order to provide a certain beam stay clear at 3.3 TeV injection energy. For the option of 1.5 TeV injection energy, the β^* has to be adapted accordingly. A β^* of 9.0 m was found to provide a beam stay clear of 16 σ in the triplet region. The corresponding optics are shown in Fig. 6.6a. Compared to Fig. 6.2 and 6.4 we can see that secondary peaks in the β functions at Q6 grow with larger β^*. For $\beta^* = 9.0$ m, it is already higher than 50 % of the peak in the triplets. With the significantly smaller apertures in the magnets from Q4 onwards, these β peaks can create new aperture bottlenecks. In Fig. 6.6b the beam stay clear of the whole interaction region is plotted for $\beta^* = 9.0$ m. We can see that the aperture bottleneck of the straight section is indeed at Q5, Q6 and Q7 now, with a beam stay clear of about 14.3 σ. This is slightly below the preliminary goal of 15 σ. It should be noted that from Q4 onwards, a racetrack shaped aperture model similar to the the LHC beam screen is used, resulting in different weights of the horizontal and vertical β functions on the beam stay clear. An increased magnet length of these quadrupoles could increase the aperture there. However, we can see that the actual minimum beam stay clear is in the left dispersion suppressor in Q9 and its surrounding dipoles. These magnets are supposed to be identical to the arc magnets. To solve the aperture problem here, either new magnet types for both quadrupoles and dipoles have to be designed specifically for the dispersion suppressors, or the aperture of the whole arc would have to be increased. Both options feature disproportional costs and are therefore undesirable. On the other hand, at 1.5 TeV injection energy, even the arcs provide less than 15 σ beam stay clear, so the apertures of the arc magnets will have to be increased or the collimation system will have to be adjusted. Independent of that development, any β peak in the dispersion suppressors that is significantly above the level of the arc FODO cells will create a bottleneck. An option to avoid these peaks would be relaxed phase advance constraints, e.g. keeping the phase advance over the whole IR (arc to arc) constant without a constraint on the phase advance to the IP, as it is being planed for large β^* in HL-LHC [49]. The viability of this option with respect to the chromaticity and spurious dispersion correction schemes must be studied. Furthermore it is possible to consider weakening the constraints of constant triplet strengths, especially in the light of a combined ramp.

Another problem of the 1.5 TeV injection energy option is again the gradient range. Going from 1.5 TeV injection energy to 50 TeV collision energy, already requires a factor of 33 for the energy ramp, leaving little margin for the squeeze. Consequently, we see that the gradients shown in Fig. 6.7 are going through a range of up to a factor of 500 for Q4 and about 100 for Q5 while the other quadrupoles are below or at least close (Q7) to the limit of 50. Even if the beam stay clear requirement for 1.5 TeV injection energy is significantly reduced (e.g. due to the aperture issues in the arcs) and the β^* at injection can be decreased, the gradient range in Q4 is still in the order of 100 (see dotted line for Q4 ramp at $\beta^* = 6.0$ m in Fig. 6.7).

Apart from better power supplies with larger ranges together with magnets with better field quantity, there are possible workarounds for this problem. For magnets that are strongest at injection optics, as is the case for Q5 in Fig. 6.7, it is possible to mitigate the problem by a combined ramp scheme as it is outlined in Fig. 6.8.

(a) Optical functions.
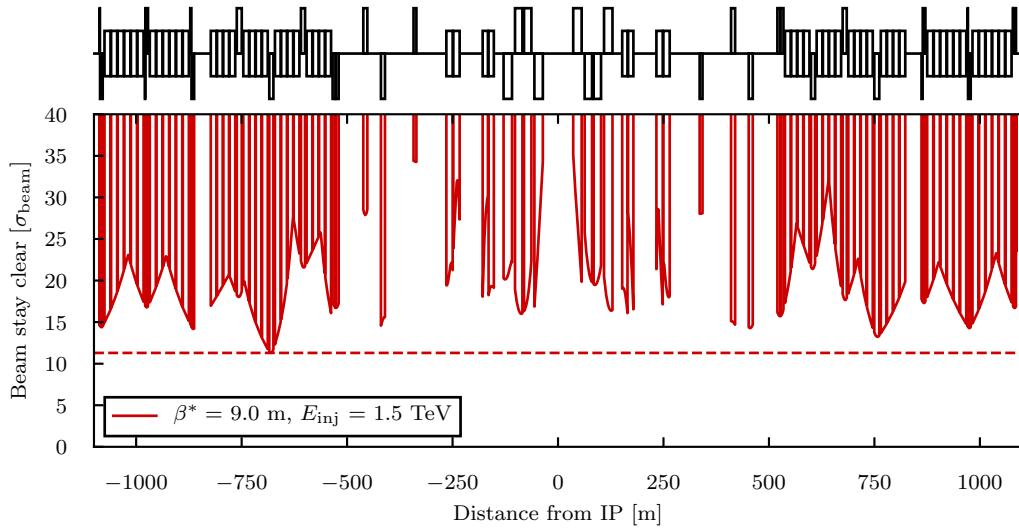
(b) Beam stay clear at 1.5 TeV.

Figure 6.6: Interaction region of the $L^* = 36\,\text{m}$ lattice with $\beta^* = 9000\,\text{m}$.
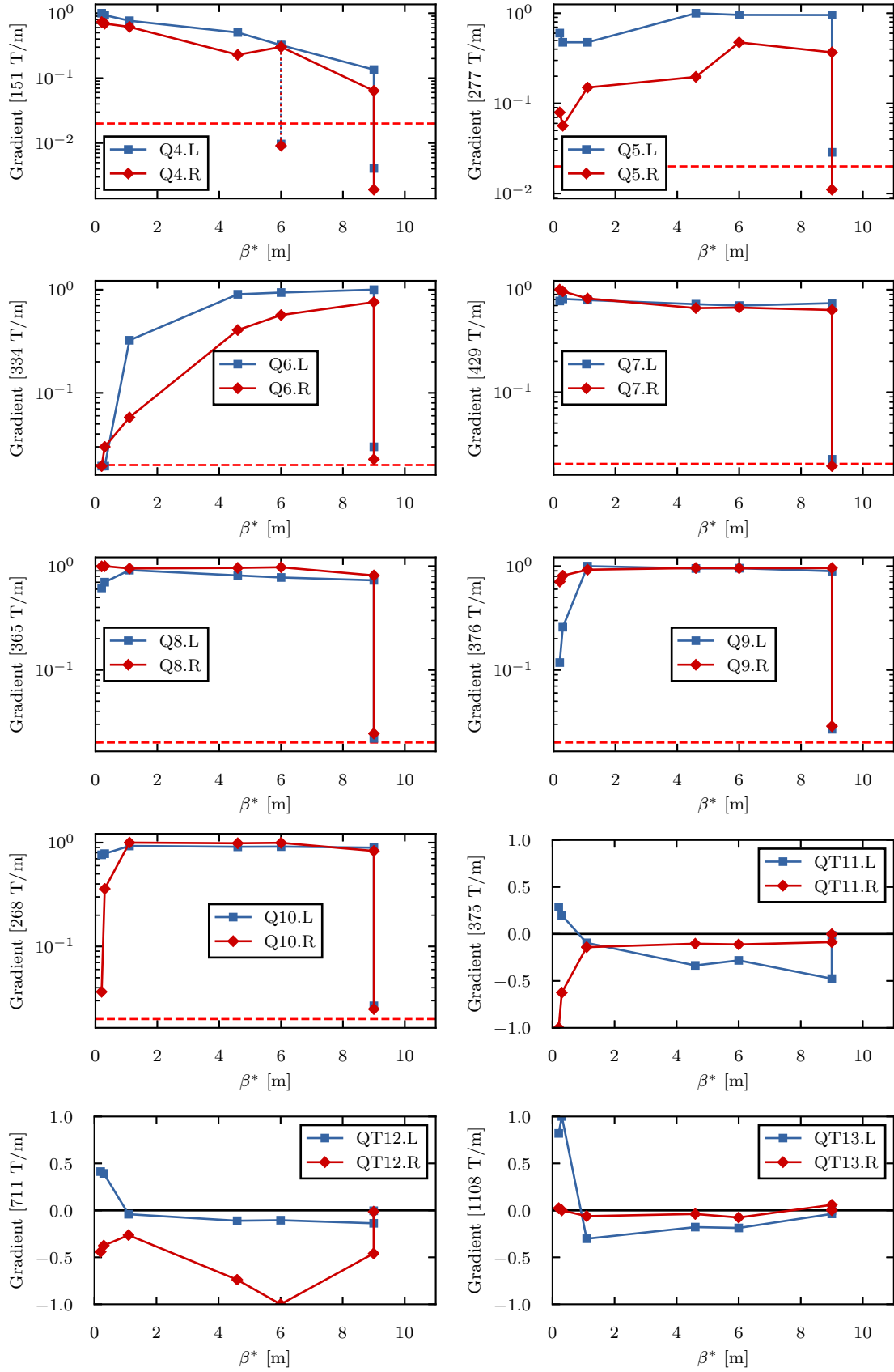
Figure 6.7: Variation of the matching quadrupole gradients in the $L^* = 36$ m lattice during transition from injection to collision optics. The ramp is modeled as a simple gradient increase at $\beta^* = 9.0$ m. The injection energy assumed here is 1.5 TeV.

Instead of the squeeze following the full ramp, partial ramps and partial squeezes can be combined so neither gradient limit nor aperture limit are exceeded. This can be further enhanced to simultaneously ramp and squeeze. The feasibility of such a combined ramp has successfully been tested and has recently become part of the the nominal ramp in the LHC [53]. A combined ramp does not help however, if the
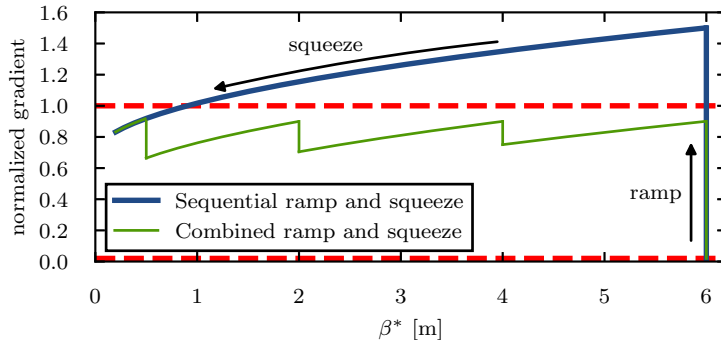

Figure 6.8: Outline of a ramp-squeeze-ramp-squeeze scheme (green) to reduce the gradient range in a single ramp and squeeze (blue) when the magnet strength is highest at injection optics.

magnet strength increases during both, ramp and squeeze, as is the case for Q4. In this case it is possible to equip the main magnet with a trim quadrupole like QT11 to QT13 that have bipolar power supplies, thereby extending the effective gradient range.

For Q5, individual power supplies or individual magnet designs for each side of the IP would also be possible, but this would limit the flexibility of the IR lattice, and is therefore not desirable.

6.5 Squeeze of the $L^* = 45$ m lattice

The increased beam stay clear of the $L^* = 45$ m lattice relaxes the requirements of the injection optics. However, the free aperture is still subject to change as the shielding thickness and minimum β^* goal are being discussed, so no final decision on the minimum β^* at injection energy can be made. For now, a β^* of 6.0 m is considered sufficient, like for the $L^* = 36$ m and $L^* = 61$ m lattices at 3.3 TeV injection energy.

In the previous sections, β^* has been squeezed down to 0.2 m, which is the minimum allowed by the aperture of the triplets in both the $L^* = 36$ m and $L^* = 61$ m lattice. In the case of the $L^* = 45$ m lattice even smaller β^* down to 0.05 m are compatible with the triplet aperture. It is now important to see if the resulting optical functions in the triplet, featuring peak β functions in the order of 250 km ($\beta^* = 0.1$ m) and 500 km ($\beta^* = 0.05$ m), can be matched to the arcs with the existing matching section. The magnet setting for $\beta^* = 0.2$ m was used as a starting point and β^* was matched to 0.1 m as an intermediate step towards 0.05 m. An optical solution is shown in Fig. 6.9. However, while the optics are matched, we can see that Q6 on both sides switched signs (Fig. 6.9 top layer), visible from Q5, Q6 and Q7 all having the same polarity and breaking up the usual FODO structure. This observation is in line with the trend of weaker gradients in Q6 at lower β^*
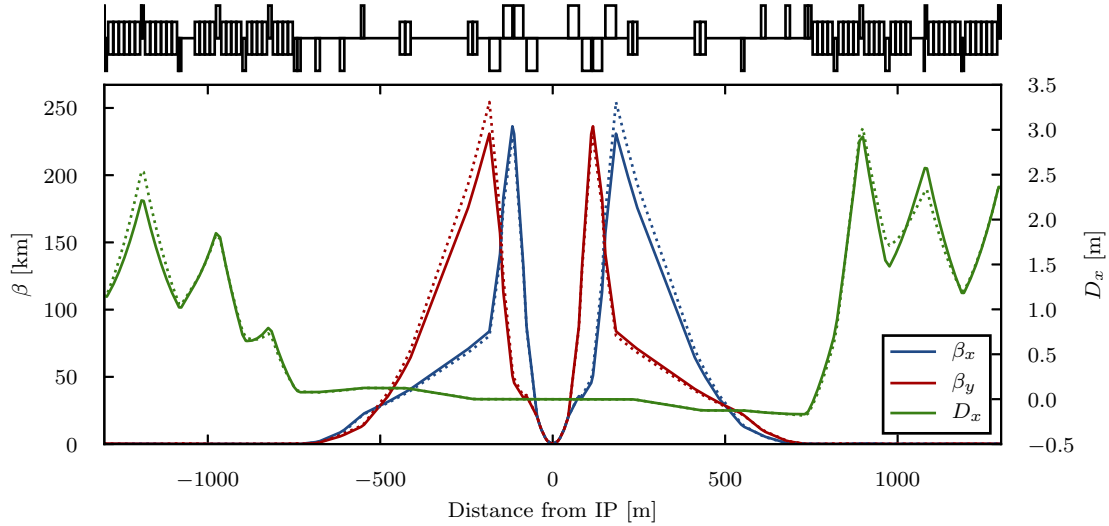
Figure 6.9: Optical functions for $\beta^* = 0.1\,\text{m}$. Initial result (solid lines) and after rematching (dotted lines).

observed earlier. In an attempt to get rid of this polarity change, gradients of Q6 were gradually changed. During rematching to compensate this change, the Q6 gradients were kept constant while the triplet quadrupole gradients were used for compensation as well. This was repeated until the matching algorithm would not converge to a solution anymore. The resulting optics are shown as dotted lines in Fig. 6.9. The peak β functions in Q3 increased significantly, reducing the beam stay clear from $21\,\sigma$ to $20\,\sigma$. While the polarity of the Q6.R on the right side could be changed back, the polarity on the left Q6 remained.

This means no optical solution for $\beta^* = 0.1\,\text{m}$ could be found that allows a full squeeze without changing the gradient polarity of at least one quadrupole. A possible work around could again be a trim quadrupole installed next to Q6 that extends the combined range to the negative. Since no optical solution without gradient polarity change was found for $\beta^* = 0.1\,\text{m}$, we can assume that this will also be the case for the absolute minimum β^* of $0.05\,\text{m}$. For the matching procedure starting from the initial $\beta^* = 0.1\,\text{m}$ solution, the polarity constraint was ignored. Still, even with arbitrary minimum and maximum gradients for Q4-QT13, no solution could be found. It will be necessary to optimize the positions of the matching quadrupoles if the $\beta^* = 0.05\,\text{m}$ has to be matched to the arcs. This optimization is also necessary in order to reduce the total length of the IR from the current $1500\,\text{m}$ to the designated $1400\,\text{m}$.

6.6 Special case: Injection optics with the forward spectrometer

The $L^* = 45\,\text{m}$ lattice is a special case as it includes the forward spectrometer of the detector. The $10\,\text{Tm}$ spectrometer dipole of the detector is supposed to not be ramped with the accelerator in order to keep the number of operational cycles of the magnet low and thereby extend its lifetime. At an injection energy of $3.3\,\text{TeV}$, the

dipole field has a severe impact as it creates a deflection of 910 µrad, about 15 times the deflection at collision energy. Even with the 7 Tm orbit corrector dipole the total deflection is still 270 µrad and the orbit offset occurring between spectrometer and corrector increases similarly. For comparison, the half crossing angle usually is in the order of 100 µrad. With the large orbit excursions from the spectrometer deflection, it is necessary to make sure that

- the beam stay clear is still enough to respect the collimation hierarchy,

- the long range beam-beam effects are equal or lower than at collision energy,

- parasitic beam crossings are avoided.

For the "ultimate" baseline goal of $\beta^* = 0.3$ m, the current $L^* = 45$ m lattice has a beam stay clear of $40\,\sigma$ with a collimation requirement of only $15.5\,\sigma$. Currently it is not clear, how this large beam stay clear is to be used. The options are much smaller β^*, increased shielding or relaxed conditions for the collimation section (i.e. larger collimator gaps, resulting in a larger beam stay clear requirement for the IR). With these uncertainties, it is a rather conservative strategy to keep the beam stay clear at injection and collision energy constant in the current lattice, i.e. aim for $40\,\sigma$ beam stay clear or more at injection.

A β^* of 6.0 m is assumed at injection energy. In Fig. 6.10a, the orbit created by the spectrometer and its correctors is plotted. The orbit excursion reaches a maximum of more than 50 mm and reduces the beam stay clear to $24\,\sigma$. It is obvious that measures have to be taken to reduce the orbit excursion. This can be achieved by superposing the spectrometer bump with a crossing angle as shown in Fig. 6.10b for a 100 µrad half crossing angle. The maximum excursion decreased significantly below 40 mm. Subsequently, the beam stay clear increased to $35\,\sigma$ which is still not enough. Furthermore, we can see that there are two parasitic crossing points around the IP that need to be avoided. While these parasitic crossings would not occur for a negative crossing angle, it is obvious that the orbit excursion would only increase, limiting the beam stay clear further. Another problem with the resulting bump arises from the separation dipoles. Superimposing the design orbit with the bump in Fig. 6.10b will lead to a parasitic crossing in or behind D1 on each side of the IP as shown in Fig. 6.11. To avoid this crossing the orbit offset must be positive on the right side and negative on the left. An alternative solution of a vertical separation will require a large vertical offset to keep the long range beam-beam effect low. This will again lead to an even smaller beam stay clear.

The first strategy to circumvent these issues is to maximize the beam stay clear of the bump. The resulting crossing angle bump with $\theta/2 = 301$ µrad is shown in Fig. 6.10c and leaves a beam stay clear of $50\,\sigma$. Again we see parasitic beam encounters around the IP. These can be avoided with a vertical bump, that also needs to be large enough to compensate the long range beam-beam effects. To estimate the long range beam-beam effects, Eq. (3.22) was used. For every long range interaction point s_i the quantity $N_{\mathrm{bb}}(s_i) = \frac{d(s_i)}{\sigma_{\mathrm{beam}}(s_i)}$, with $d(s_i)$ the distance of the two beams, was added up according to
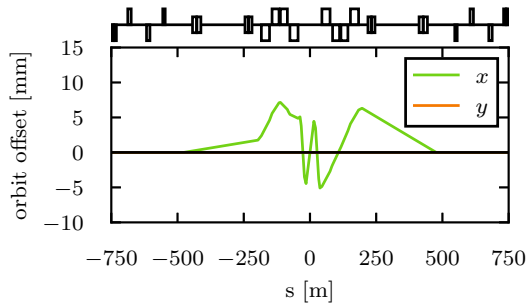
$$F_{\mathrm{lr}} = \sum_i \frac{1}{N_{\mathrm{bb}}^2(s_i)}. \tag{6.3}$$
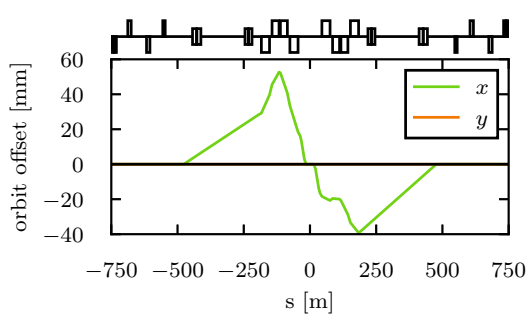
(a) Spectrometer bump only.
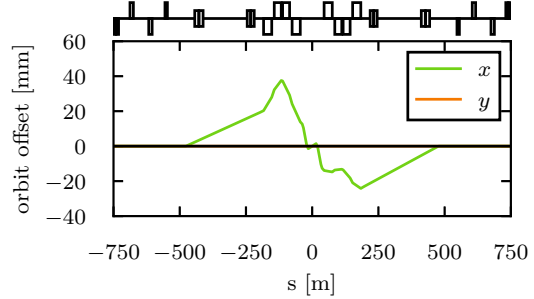
(b) Spectrometer bump with a 100 µrad crossing angle

(c) Spectrometer bump with a 301 µrad crossing angle
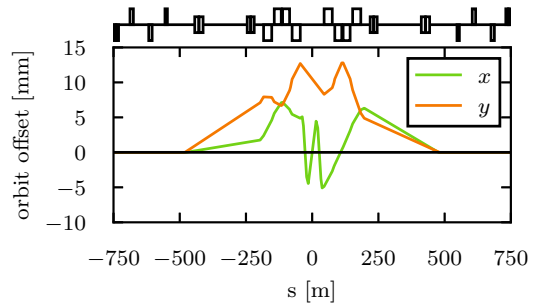
(d) Spectrometer bump with a 301 µrad crossing angle and large vertical separation.
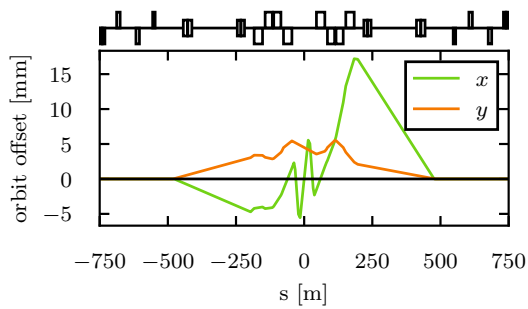
(e) Spectrometer bump with a 375 µrad crossing angle and medium vertical separation
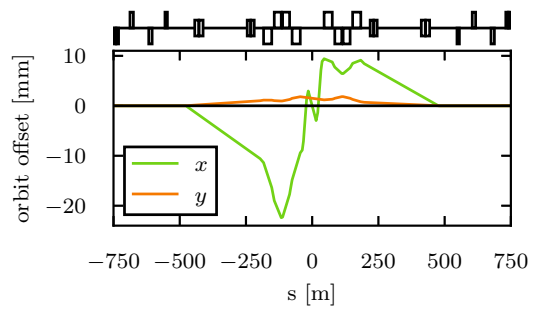
(f) Inverted spectrometer bump with a −200 µrad crossing angle and vertical separation

Figure 6.10: Different combinations of the horizontal spectrometer, horizontal crossing angle and vertical separation.

Figure 6.11: Parasitic crossing behind D1 due to the spectrometer bump in Fig. 6.10b.

First, this was done for the case of nominal crossing with $15.2\,\sigma$ normalized separation corresponding to $77.6\,\mu$rad at $3.3\,$TeV and $\beta^* = 6.0\,$m without spectrometer. Then the spectrometer was switched on and the different settings of crossing angle and vertical separation were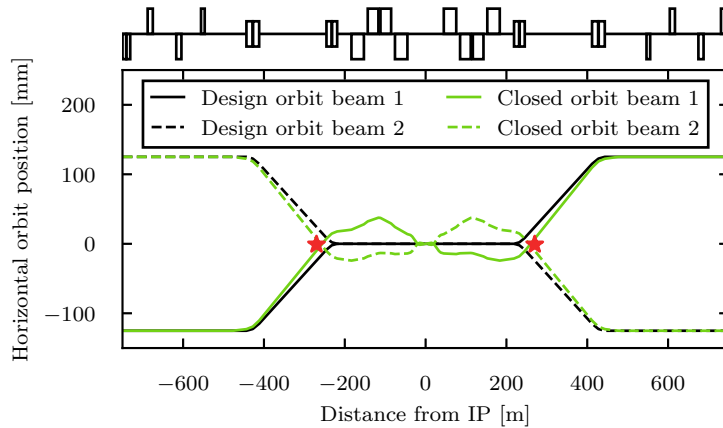 examined. For a constant long range beam-beam effect, F_{lr} stays constant (see Eq. (3.22)). The smallest vertical separation bump that satisfies this condition is shown in Fig. 6.10d. It leaves a beam stay clear of $47\,\sigma$, enough to make injection possible. It should be noted that long-range encounters in D1 were neglected when calculating F_{lr}, assuming the separation will diminish their weight in F_{lr}. However, since in Fig. 6.10d, the orbit offset in the left D1 is positive, the separation is in fact increased for a few encounters, mainly separated in the vertical plane. Thus the vertical bump will likely have to be increased slightly.

The main disadvantage of this optics is the large vertical spurious dispersion that is created from feed down effects in the triplet and needs to be compensated in the arcs. A smaller vertical separation is desirable. To keep F_{lr} constant, the superimposed horizontal crossing angle then needs to be increased further. Fig. 6.10e shows an alternative option with $\theta/2 = 375\,\mu$rad. The vertical separation is reduced by $60\,\%$ compared to the previous option. The beam stay clear of $46\,\sigma$ is again enough and this time the orbit offset is favorable in D1.

In [45], a regular inversion of the spectrometer polarity was identified as a means to distribute the radiation load and reduce the peak doses in the triplet quadrupoles. The orbit bump resulting from the inversion is basically the one seen in Fig. 6.10a reflected vertically. The obvious solution to invert the crossing angle of $\theta/2 = 375\,\mu$rad (Fig. 6.10e) as well in order to get mirrored orbit bumps is not possible because the positive orbit offset on the left and negative offset on the right, superimposed to the separation orbit will result in parasitic crossings in D1. The option to invert the solution in Fig. 6.10d should work but if the large vertical dispersion is to be avoided, the (inverted) crossing angle should be smaller. Fig. 6.10f shows an alternative solution with inverted spectrometer, $\theta/2 = -200\,\mu$rad and a small vertical separation, leaving just enough beam stay clear with $41\,\sigma$.

To give an estimate of the effect of the spurious dispersion created by the injection orbits, Fig. 6.12a shows the orbit excursions due to the correction of the spurious dispersion with an HL-LHC like scheme. The large vertical dispersion of the injection
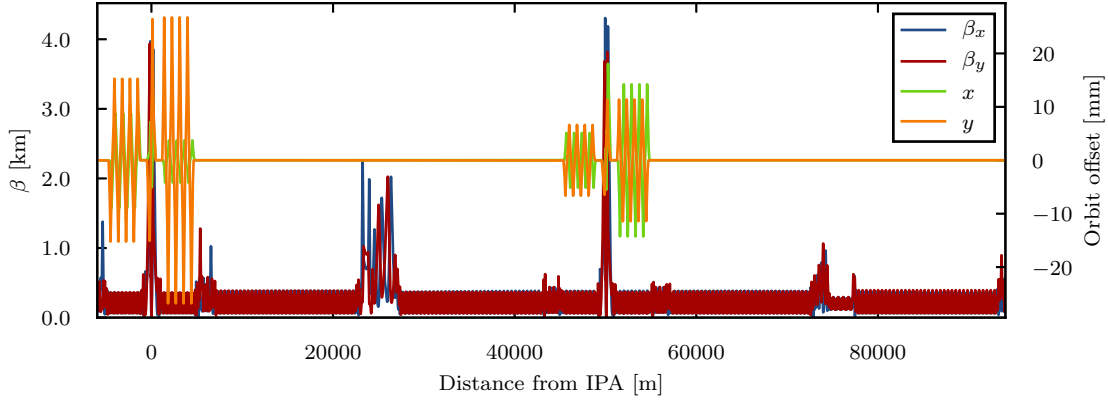
(a) Orbit excursion with the HL-LHC like dispersion correction scheme for $\theta/2 = 301\,\mu\mathrm{rad}$ and large vertical separation at IPA and $\theta/2 = 375\,\mu\mathrm{rad}$ and smaller vertical separation at IPG (around $s = 50\,\mathrm{km}$).
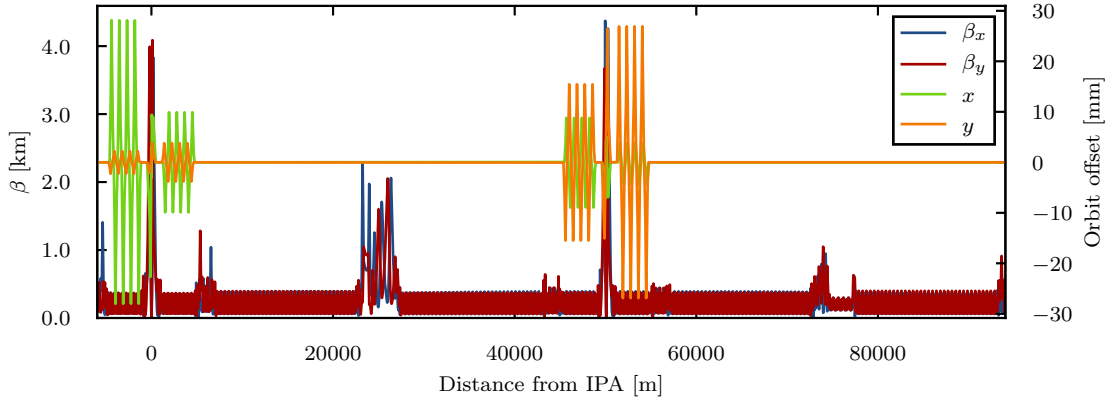
(b) Orbit excursion with the HL-LHC like dispersion correction scheme for the inverted spectrometer with $\theta/2 = -200\,\mu\mathrm{rad}$ and smaller vertical separation at IPA and $\theta/2 = -301\,\mu\mathrm{rad}$ and large vertical separation at IPG (around $s = 50\,\mathrm{km}$).

Figure 6.12: Orbit excursion in the arcs caused by the spurious dispersion correction.

orbit shown in Fig. 6.10d and applied in IPA results in a significant orbit offset in the vertical plane and only a small one in the horizontal plane. The preferable injection orbit in Fig. 6.10e applied in IPG leads to smaller maximum excursions by distributing the created dispersion in both planes. On the other hand, both injection options for the inverted spectrometer result in large orbit offsets as seen in Fig. 6.12b. Furthermore we can see that the HL-LHC like correction scheme is not applicable to FCC-hh at injection energy as the orbit excursions exceed 15 mm in the arcs, where the free aperture is only 15 mm [54].

We have seen that the unramped horizontal spectrometer requires a superimposed horizontal crossing angle in order to reduce the orbit excursion and give a reasonable beam stay clear. In all cases that met the requirements, multiple crossings occurred in the horizontal plane, that needed an additional vertical separation. If the need for a vertical crossing arises, e.g. to compensate PACMAN effects [55], the injection will need to be performed as shown in the previous paragraph, then

the transition from horizontal crossing to vertical crossing has to be done after the ramp, when the spectrometer bump is rather small.

In conclusion, for the constraint of a constant beam stay clear of $40\,\sigma$, injection orbit bumps were found that also satisfied the requirement of a constant long range beam-beam effect. If the available aperture at collision is used to decrease β^*, the minimum beam stay clear requirement will decrease accordingly and relax this constraint. Furthermore, developments in the collimation hierarchy (current bottleneck at injection is the arc with about $10\,\sigma$ beam stay clear), as well as the detector design tending towards a forward solenoid or a $5\,\mathrm{Tm}$ forward dipole will relax the picture further.

Chapter 7

First dynamic aperture studies

The design strategy deduced in Section 4.5 demands to increase the triplet length until limited by chromaticity or dynamic aperture. For this purpose, first exploratory dynamic aperture studies were conducted using the tracking code SixTrack [22]. In the LHC, the DA for the collision optics is mainly limited by field imperfections in the final focus triplet and the separation and recombination dipoles. This is due to the large β functions and the orbit offset from the crossing angle that increase the sensitivity of the beam to field errors [50, 56]. With this in mind, the smallest DA can be expected for the smallest β^*. Thus the following studies were conducted for the "ultimate" options with $\beta^* = 0.3\,\mathrm{m}$. If a reasonable DA can be achieved with these parameters, any setting with larger β^* should as well be possible.

7.1 Field error definition

In these first DA studies, the impact of field errors of the final focus triplet is investigated. The contributions of the separation and recombination dipoles are neglected, field errors are assigned to the triplet quadrupoles only. For the expression of the field errors of the FCC-hh magnets, the LHC convention [57] is used: the strengths of the field errors of a quadrupole at reference radius R_{ref} are defined by the formula

$$B_y + iB_x = 10^{-4}g \cdot R_{\mathrm{ref}} \sum_{n=1}^{\infty} (b_n + ia_n) \left(\frac{x + iy}{R_{\mathrm{ref}}} \right)^{n-1} \tag{7.1}$$

with g the quadrupole gradient. R_{ref} is usually set to approximately two thirds of the magnet aperture radius. b_n and a_n are the normalized normal and skew multipoles. They are composed of systematic $(b_{n_{\mathrm{s}}})$, uncertainty $(b_{n_{\mathrm{u}}})$ and random $(b_{n_{\mathrm{r}}})$ components as

$$b_n = b_{n_{\mathrm{s}}} + \frac{\xi_{n_{\mathrm{u}}}}{1.5}b_{n_{\mathrm{u}}} + \xi_{n_{\mathrm{r}}}b_{n_{\mathrm{r}}} \tag{7.2}$$

where $\xi_{n_{\mathrm{u}}}$ and $\xi_{n_{\mathrm{r}}}$ are Gaussian distributed random numbers truncated at $1.5\,\sigma$ and $3\,\sigma$ respectively [56]. Note that the uncertainty $b_{n_{\mathrm{u}}}$ is defined as 1.5 standard deviations of a normal distribution, thus the factor 1.5^{-1}. While the contribution of the uncertainty component $\xi_{n_{\mathrm{u}}}$ is the same for all magnets of one class, the contribution of the random component $\xi_{n_{\mathrm{r}}}$ is different for each individual magnet.

As a first guess for the triplet errors, the error tables and error definitions of the HL-LHC triplet, scaled with the aperture were used [16]. The field error components

73

Table 7.1: Field error components of Q1 and Q3 in the $L^* = 36\,\text{m}$ lattice with $R_{\text{ref}} = 33\,\text{mm}/39\,\text{mm}$.

	Systematic		Uncertainty		Random	
Normal	Injection	High Field	Injection	High Field	Injection	High Field
b_1	0.000	0.000	0.000	0.000	0.000	0.000
b_2	0.000	0.000	0.000	0.000	(10)	(10)
b_3	0.000	0.000	0.82	0.82	0.82	0.82
b_4	0.000	0.000	0.57	0.57	0.57	0.57
b_5	0.000	0.000	0.42	0.42	0.42	0.42
b_6	-20.332	-0.438	1.1	1.1	1.1	1.1
b_7	0.000	0.000	0.19	0.19	0.19	0.19
b_8	0.000	0.000	0.13	0.13	0.13	0.13
b_9	0.000	0.000	0.07	0.07	0.07	0.07
b_{10}	3.728	-0.124	0.2	0.2	0.2	0.2
b_{11}	0.000	0.000	0.26	0.26	0.26	0.26
b_{12}	0.000	0.000	0.18	0.18	0.18	0.18
b_{13}	0.000	0.000	0.009	0.009	0.009	0.009
b_{14}	0.173	-0.867	0.023	0.023	0.023	0.023
b_{15}	0.000	0.000	0.000	0.000	0.000	0.000
Skew						
a_1	0.000	0.000	0.000	0.000	0.000	0.000
a_2	-0.627	-0.627	0.000	0.000	(10)	(10)
a_3	0.000	0.000	0.65	0.65	0.65	0.65
a_4	0.000	0.000	0.65	0.65	0.65	0.65
a_5	0.000	0.000	0.43	0.43	0.43	0.43
a_6	0.044	0.044	0.31	0.31	0.31	0.31
a_7	0.000	0.000	0.19	0.19	0.19	0.19
a_8	0.000	0.000	0.11	0.11	0.11	0.11
a_9	0.000	0.000	0.08	0.08	0.08	0.08
a_{10}	0.013	0.013	0.04	0.04	0.04	0.04
a_{11}	0.000	0.000	0.026	0.026	0.026	0.026
a_{12}	0.000	0.000	0.014	0.014	0.014	0.014
a_{13}	0.000	0.000	0.01	0.01	0.01	0.01
a_{14}	-0.004	-0.004	0.005	0.005	0.005	0.005
a_{15}	0.000	0.000	0.000	0.000	0.000	0.000

Table 7.2: Field error components of Q2a and Q2b in the $L^* = 36\,\mathrm{m}$ lattice with $R_\mathrm{ref} = 39\,\mathrm{mm}$.

	Systematic		Uncertainty		Random	
Normal	Injection	High Field	Injection	High Field	Injection	High Field
b_1	0.000	0.000	0.000	0.000	0.000	0.000
b_2	0.000	0.000	0.000	0.000	(10)	(10)
b_3	0.000	0.000	0.82	0.82	0.82	0.82
b_4	0.000	0.000	0.57	0.57	0.57	0.57
b_5	0.000	0.000	0.42	0.42	0.42	0.42
b_6	-20.194	-0.409	1.1	1.1	1.1	1.1
b_7	0.000	0.000	0.19	0.19	0.19	0.19
b_8	0.000	0.000	0.13	0.13	0.13	0.13
b_9	0.000	0.000	0.07	0.07	0.07	0.07
b_{10}	3.705	-0.126	0.2	0.2	0.2	0.2
b_{11}	0.000	0.000	0.26	0.26	0.26	0.26
b_{12}	0.000	0.000	0.18	0.18	0.18	0.18
b_{13}	0.000	0.000	0.009	0.009	0.009	0.009
b_{14}	0.168	-0.867	0.023	0.023	0.023	0.023
b_{15}	0.000	0.000	0.000	0.000	0.000	0.000
Skew						
a_1	0.000	0.000	0.000	0.000	0.000	0.000
a_2	-0.716	-0.716	0.000	0.000	(10)	(10)
a_3	0.000	0.000	0.65	0.65	0.65	0.65
a_4	0.000	0.000	0.65	0.65	0.65	0.65
a_5	0.000	0.000	0.43	0.43	0.43	0.43
a_6	0.051	0.051	0.31	0.31	0.31	0.31
a_7	0.000	0.000	0.19	0.19	0.19	0.19
a_8	0.000	0.000	0.11	0.11	0.11	0.11
a_9	0.000	0.000	0.08	0.08	0.08	0.08
a_{10}	0.015	0.015	0.04	0.04	0.04	0.04
a_{11}	0.000	0.000	0.026	0.026	0.026	0.026
a_{12}	0.000	0.000	0.014	0.014	0.014	0.014
a_{13}	0.000	0.000	0.01	0.01	0.01	0.01
a_{14}	-0.005	-0.005	0.005	0.005	0.005	0.005
a_{15}	0.000	0.000	0.000	0.000	0.000	0.000

are listed in Tables 7.1 and 7.2. The systematic components for Q2 differ slightly because of the different length and the resulting different impact of the coil ends.

The reference radius R_{ref} with a value of 50 mm for the HL-LHC triplet was scaled proportionally to the coil aperture of the different IR magnets. According to Eq. (3.8), this guarantees the same B_x and B_y at the inner coil aperture for all magnets, a scaling that is deemed sufficient for now [58].

7.2 Tracking studies

The tracking parameters used for the studies presented in this work are listed in Table 7.3. They were adopted from first DA studies with main dipole field errors [59]. The DA was calculated for 60 seeds, i.e. 60 sets of randomly generated uncertainty and random components for the field errors. The amplitude was scanned in steps of $2\,\sigma$ with 30 particle pairs in between, which is considered enough for a precision of $0.5\,\sigma$ [22]. For the tracking, a thin lattice was used. This means the accelerator is modeled exclusively with drifts and kicks. In this lattice the triplet quadrupoles have been replaced by 4 thin quadrupoles each, with drifts keeping the total lengths constant. All other elements in the ring have been replaced by two thin elements. The relative momentum offset of $dp/p = 0.00027$ is adopted from LHC tracking studies. It defines the longitudinal oscillation amplitude of the tracked particles. Due to the exploratory nature of these first dynamic aperture studies, probing five angles in the x-y plane was considered sufficient.

Table 7.3: Parameters of the tracking studies.

Turns	10^5
Number of seeds	60
Normalized emittance	2.2 μm
Energy of reference particle E_0	50 TeV
Chromaticity Q'	2
Relative momentum offset dp/p	0.00027
Amplitude step size	$2\,\sigma$
Particle pairs per step	30
Angles in x-y plane	5

7.2.1 Dynamic aperture without crossing angles

For the dynamic aperture studies presented in this thesis, dipolar error components (a_1, b_1) and quadrupolar error components (a_2, b_2) were not included, as they are expected to have a minor impact on the DA after correction. Magnet misalignments were not implemented either.

For the first tracking studies with magnet field errors, the crossing angles were turned off, meaning the closed orbit was going through the center of all quadrupoles. After assigning the errors, a matching routine made sure that tunes and chromaticities were kept constant. As a consequence of the absence of quadrupole errors or feed down effects from orbit offset, only the chromaticity needed correction. No other magnets except the triplet quadrupoles were assigned errors and the chromaticity

correction sextupoles in the arcs were the only other higher order multipoles in the lattice. Their strengths as well as the maximum β functions are listed in Table 7.4.

Table 7.4: Maximum β functions and sextupole strengths for $\beta^* = 0.3\,\mathrm{m}$.

| L^* | β_{max} | Integrated sextupole strength $m \cdot l$ | |
		horizontal	vertical
$36\,\mathrm{m}$	$40\,\mathrm{km}$	$0.019\,\mathrm{m}^{-2}$	$-0.039\,\mathrm{m}^{-2}$
$45\,\mathrm{m}$	$80\,\mathrm{km}$	$0.024\,\mathrm{m}^{-2}$	$-0.047\,\mathrm{m}^{-2}$
$61\,\mathrm{m}$	$70\,\mathrm{km}$	$0.023\,\mathrm{m}^{-2}$	$-0.046\,\mathrm{m}^{-2}$

The resulting dynamic apertures are plotted in Fig. 7.1. The $L^* = 45\,\mathrm{m}$ lattice
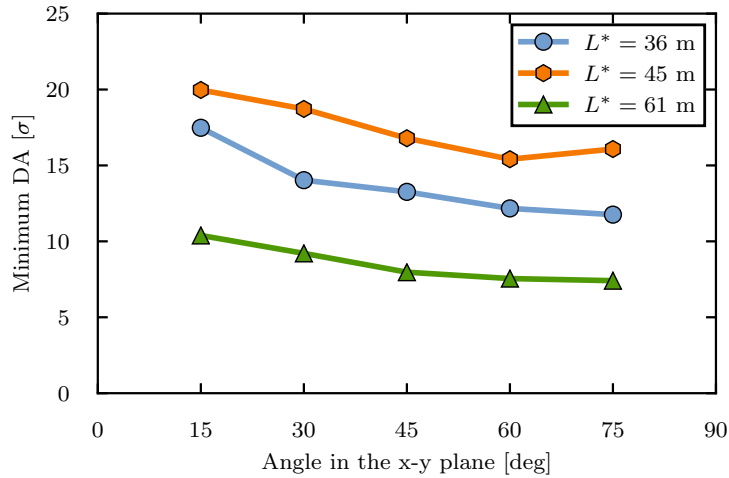
Figure 7.1: Minimum dynamic apertures for the IR lattices with $L^* = 36\,\mathrm{m}$, $45\,\mathrm{m}$, and $61\,\mathrm{m}$ with $\beta^* = 0.3\,\mathrm{m}$. The crossing angles were turned off.

shows the largest DA with values around $20\,\sigma$. This is unexpected as this lattice features the largest β functions. A possible explanation is the fact that the field errors scale with the aperture [58]. The fraction of the coil aperture occupied by the beam is the smallest in the $L^* = 45\,\mathrm{m}$ lattice where the beam stay clear for $\beta^* = 0.3\,\mathrm{m}$ is $49\,\sigma$ without crossing angles, compared to 24 to $26\,\sigma$ in the other lattices. Consequently, particles experience the smallest field errors at similar normalized amplitudes. This can easier be seen by expressing the DA in terms of coil radii, as shown in Fig. 7.2. It is calculated by

$$\mathrm{DA_{coil}} = \frac{\sigma_x \cdot \mathrm{DA}_\sigma}{r_{\mathrm{coil}}} \tag{7.3}$$

with the beam size σ_x and the inner coil aperture radius r_{coil} taken at Q2 where the largest β functions occur. While the minimum DA is not just defined by this particular place and the problem is much more complex, it illustrates why the DA of the $L^* = 45\,\mathrm{m}$ in Fig. 7.1 can be the largest although it features the highest β functions and chromaticity. Thus, at constant β^*, the larger aperture due to the longer triplet not only allows for more shielding, but also has a positive impact on the DA.
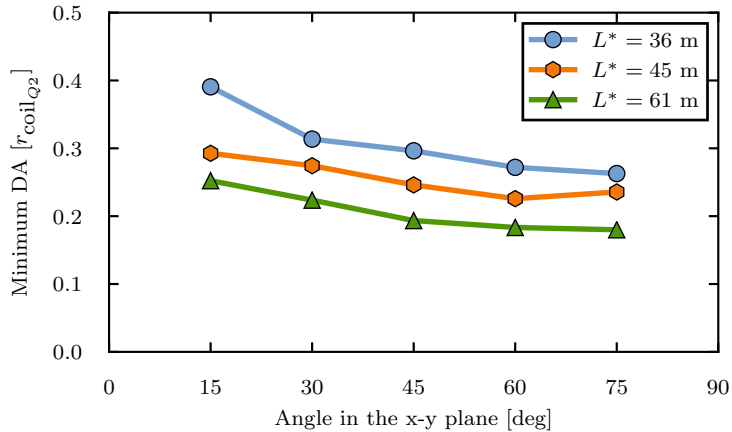
Figure 7.2: Minimum dynamic apertures for the IR lattices with $L^* = 36\,\mathrm{m}$, $45\,\mathrm{m}$, and $61\,\mathrm{m}$ with $\beta^* = 0.3\,\mathrm{m}$. The crossing angles were turned off.

The other two lattices are more comparable in terms of aperture use and the $L^* = 36\,\mathrm{m}$ lattice has a significantly higher DA than the $L^* = 61\,\mathrm{m}$ lattice, due to the lower peak β functions in the triplet. This shows that the L^* is a very important parameter for the dynamic aperture and should be chosen as small as possible, affirming the β^* minimization strategy devised in Section 4.4.

7.2.2 Dynamic aperture with crossing angles

Orbit excursions in the triplet will increase the beams sensitivity to errors. Consequently, crossing angles will worsen the picture. Indeed, the DA was reduced to zero when the crossing angles were turned on. Thus, the effects of errors that come with the orbit offset in the triplet magnets must be corrected.

The first observation was an orbit beating in the horizontal and vertical plane, even if the crossing was in the same plane for both main IPs. This is due to feed down effect coming from normal and skew multipolar components when passed off-axis, e.g. an off-center sextupole acting like a centered dipole and quadrupole.

The distortions of the crossing orbit were corrected using the same orbit correctors as for the crossing itself, but in both planes at the same time. Rematching the orbit as a circular solution showed problems with stability. For multiple seeds the TWISS algorithm of MAD-X failed to find a periodic solution, leading to the matching algorithm to fail. This is likely due to the length of the ring, giving small changes a huge leverage. To work around this problem, the orbit was matched as two lines, one for IPA and one for IPG. As a side effect, a slight residual orbit beating in the order of $1 \times 10^{-6}\,\mathrm{m}$ occurred in the ring, created by small deviations of the matching result to the constraints.

The quadrupolar feed down effects led to a mismatch of the beta function (β beating), so the tunes had to be rematched to avoid resonances. For this, the two main quadrupole families of the long arcs were used. The resulting tunes for 60 seeds of randomly assigned errors are shown in Fig. 7.3. As can be seen, the design tune is very close to the coupling resonance $Q_x - Q_y = 4$. The gap in the spread of tunes suggests that, due to coupling, horizontal and vertical tune exchanged values when approaching the design tune. Consequently, the matching algorithm could

not converge. Some of the resulting tunes are close to other resonance lines of third and tenth order. Hence, coupling correction is necessary. As a first iteration for
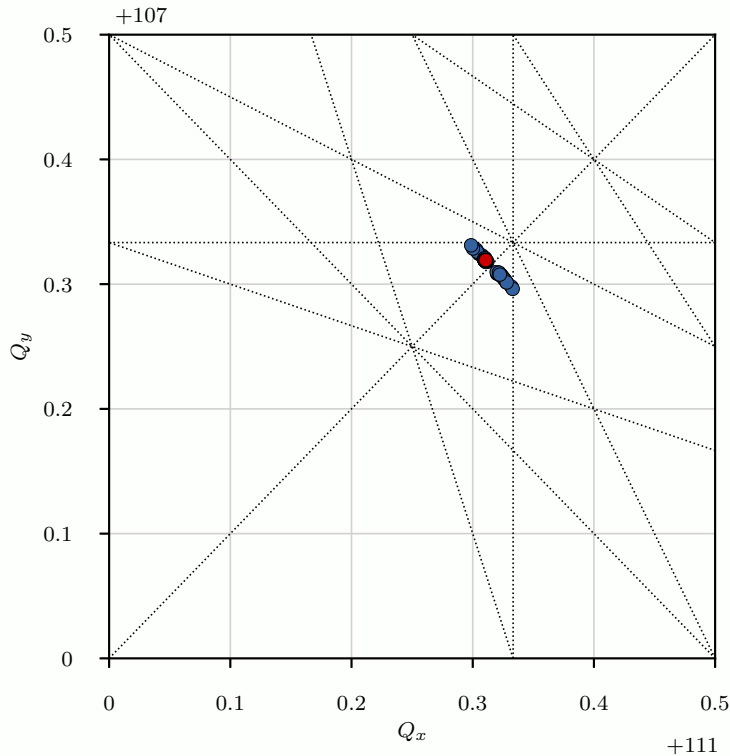

Figure 7.3: Tune spread (blue) for 60 seeds with triplet errors and crossing angles on. The arc quadrupoles of the long arcs were used in an attempt to match the tunes to the design tune (red).

the design of a coupling correction scheme, skew quadrupole correctors like those in the LHC corrector package were installed in the IR (red dotted lines in Fig. 7.4). Of course, their feed down effect created orbit beating again. Even when correcting
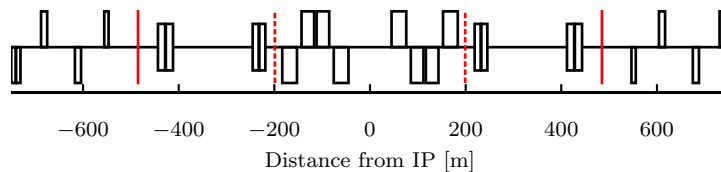

Figure 7.4: Positions of the skew quadrupole correctors: LHC corrector package like (red dotted lines) and improved position to avoid feedback on closed orbit (red solid lines).

coupling and orbit at the same time, the matching algorithm did not converge to any reasonable result. To avoid this problem, the skew quadrupole correctors were moved in front of Q4, just behind the crossing angle orbit correctors (red solid lines in Fig. 7.4). Using this position for the correctors, the four coupling matrix elements at four positions of the ring, the end of the matching sections, were matched to zero. With only four degrees of freedom but 4×4 matching constraints, the system is over-determined. Subsequently the matching algorithm did not converge to a completely

uncoupled solution. However, as it reduced the R matrix elements (see Eq. (2.55)), the coupling was reduced enough to allow tune rematching as can be seen in Fig. 7.5.
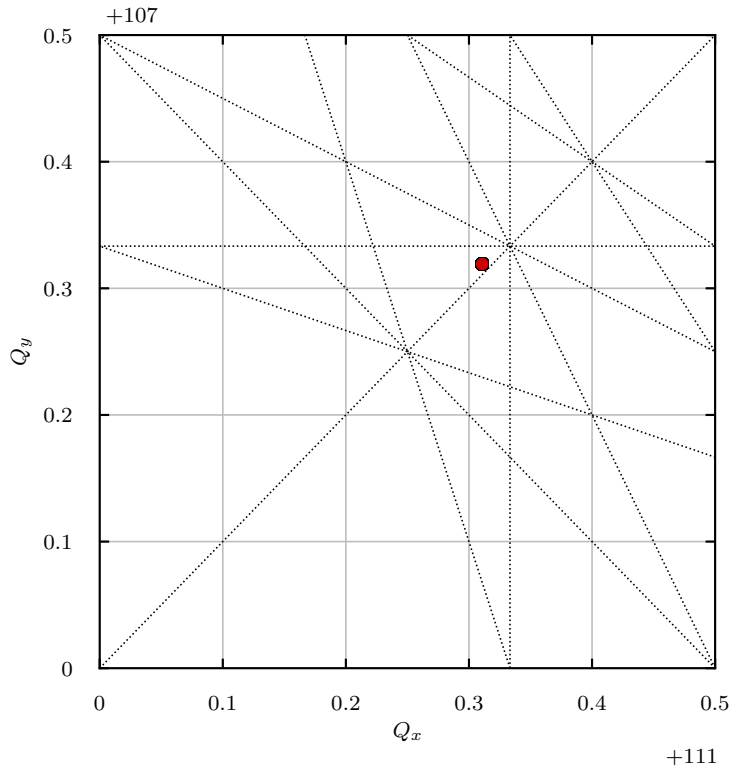

Figure 7.5: Tune spread after coupling correction and tune correction. For all 60 seeds, the tunes could be exactly matched to the design tune (red).

It should be noted that the skew quadrupoles in the LHC corrector package are only used to compensate the skew quadrupole components a_2 locally, not to compensate coupling from feed down effects. Instead, skew quadrupoles in the arcs correct coupling globally by minimizing the corresponding resonance driving terms. Implementing a similar, non-local scheme in FCC-hh will be the next step towards a more sophisticated coupling correction.

Even with a first coupling correction in place, the minimum DA with crossing angles remained zero. This already shows that the beam stability in FCC-hh will be a much larger challenge than in HL-LHC, where studies with the non-linear corrector package turned off resulted in a minimum DA of $5\,\sigma$ [60]. We can expect that for comparable dynamic apertures, the correction system in FCC-hh needs to be improved over the HL-LHC approach.

The benefit of LHC-like local corrections of non-linear field errors has been studied in [4, 61]. They rely on higher order multipole correctors located behind the triplet. The corrector strengths are set to minimize the resonance driving terms by countering the contribution from the triplet errors [62]. This strategy makes use of the known field errors assigned to the magnets while in a real machine, it uses a magnetic model based on measured non-linear errors [50]. Figure 7.6 shows the first result of this study. To get a non-zero DA, an LHC-like local correction of sextupolar errors and local coupling correction to compensate feed-down effects from skew
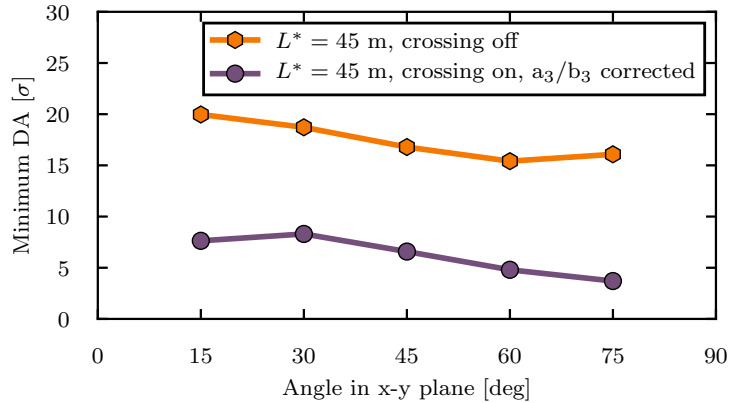
Figure 7.6: Minimum dynamic apertures for the $L^* = 45\,\mathrm{m}$ lattice with $\beta^* = 0.3\,\mathrm{m}$. DA with crossing angles taken from [4].

field errors is needed. The minimum DA with crossing angles in the IRs is $4\,\sigma$ at an angle in the $x - y$ plane of $75\,°$. In a further study correcting also octupolar errors (a_4, b_4) and the normal dodecapolar component (b_6), the minimum DA increased to $10\,\sigma$ [61]. This value is rather encouraging, considering the early stage of the development. For comparison, the target DA of the LHC, including misalignments and field errors of all magnets, is $12\,\sigma$ in the absence of beam-beam interactions [26].

Chapter 8

Summary and Outlook

In this thesis possible interaction region designs for FCC-hh, a $100\,\mathrm{TeV}$ proton-proton collider, were studied. Starting from scaled LHC and HL-LHC lattices, first simulations of energy deposition from collision debris showed that the final focus system would be exposed to levels of radiation that exceed the quench limit by one order of magnitude and the current lifetime dose limit by two orders of magnitude.

It is clear that energy deposition is the main driver of the final focus design that needs to combine high luminosity performance with sufficient radiation mitigation. Several lattice options were developed that allowed β^* values around or below the current "ultimate" goal of $0.3\,\mathrm{m}$, while leaving space for shielding to protect the magnets. Studies of the minimum β^* showed a beneficial effect of long triplet magnets while L^* only had a minor impact on the limitation of β^* by the magnet apertures. Still, L^* should be kept as small as possible in order to limit chromaticity and the impact of field errors.

A new concept for radiation mitigation, the Q1 split, was developed. It distributed the peak doses in the final focus triplet more evenly by splitting the first quadrupole into two submagnets with individual apertures. In combination with a variation of the crossing plane, the sustainable integrated luminosity in the $L^* = 36\,\mathrm{m}$ option could be increased to the order of one high luminosity run, i.e. $5000\,\mathrm{fb}^{-1}$. Nevertheless, the quadrupoles ideally should sustain the FCC-hh lifetime goal of $17\,500\,\mathrm{fb}^{-1}$ in order to avoid having to exchange highly radioactive magnets with long cool-down times. While the conventional approach of very thick shielding in the $L^* = 45\,\mathrm{m}$ lattice already meets this goal, it also limits the achievable minimum β^* to $0.2\,\mathrm{m}$. The more ambitious option using only moderate shielding thickness but featuring a minimum β^* down to $0.05\,\mathrm{m}$ motivates research on more radiation resistant magnets. With materials that feature lifetime limits around $100\,\mathrm{MGy}$ or more, the sustainable integrated luminosity would already be in the order of the FCC-hh life time goal of $17\,500\,\mathrm{fb}^{-1}$ for the $L^* = 45\,\mathrm{m}$ lattice. This also applies to the more compact $L^* = 36\,\mathrm{m}$ lattice if mitigation measures are applied (see Table 8.1).

First tracking studies revealed that orbit excursions in the triplet magnets due to crossing angles are the biggest challenge for the dynamic aperture for $\beta^* = 0.3\,\mathrm{m}$. With a full local correction of sextupolar, octupolar and dodecapolar triplet errors, further studies found a DA of $10\,\sigma$ for the $L^* = 45\,\mathrm{m}$ lattice [61]. This value is rather encouraging for this early design phase. However, the vanishing of the dynamic aperture without local correction poses an operational challenge and needs

Table 8.1: Summary of the presented triplet options. The shielding thickness defines the minimum β^*. The β^* used for FLUKA studies was set to the "ultimate" goal where possible and mainly impacts the dose via the crossing angle.

L^* [m]	Shielding thickness [mm]	Minimum β^{*1} [m]	β^* for FLUKA study [m]	Crossing angle [µrad]	Dose for $17\,500\,\text{fb}^{-1}$ [MGy]
46	0	0.8	0.8	86 (horizontal)	14000
36	15	0.2	0.3	140 (vertical)	250
					175^2
					120^3
61	15	0.2	0.3	170 (vertical)	215
45	15	0.05^4	0.3	178 (vertical)	145
	55	0.15			15

[1] Assuming an ambitious beam stay clear requirement of $12\,\sigma$
[2] With Q1 split
[3] With Q1 split and crossing angle variation
[4] Optics solution for arc integration only found for $\beta^* = 0.1\,\text{m}$ or larger

to be understood. First steps in this direction have been taken in [61] by adapting the correction scheme of the spurious dispersion, resulting in a minimum DA of $2\,\sigma$ without non-linear corrections.

Based on the studies presented in this thesis and the dynamic aperture obtained with local correction, the $L^* = 45\,\text{m}$ lattice has become the reference design for the interaction region of FCC-hh. In terms of β^* it has notably exceeded the goal set by the "ultimate" parameter set, opening the possibility for significantly higher luminosity. This might not be helpful in the 25 ns bunch spacing option if the detector cannot handle the high pile-up. However, the 5 ns option intended to reduce the pile-up relies on a challenging reduction of the transverse emittance in order to keep the luminosity constant. In case the emittance target of the 5 ns option cannot be reached, a lower β^* can compensate the luminosity decrease.

In the next step of the IR lattice development, the design of the triplet magnets has to become more realistic. The current lengths between 26 m and 31 m represent great challenges for manufacture and transportation. Splitting them into several submagnets with adequate spacing in between will have a significant impact on optics and radiation load and will have to be investigated. Furthermore, the heat load from collision debris on the inner shielding will require cooling channels that reduce the effective thickness. The positions of these channels have to be optimized to not compromise the magnet lifetime.

Continuing on the lattice design, the matching section and matching approach will require optimization in order to get enough flexibility to match the $\beta^* = 0.05\,\text{m}$ optics to the arcs and to reduce the overall length of the straight section from currently 1500 m to the foreseen 1400 m.

The current collision scenario for FCC-hh relies on crab cavities to compen-

sate the reduced bunch overlap due to large crossing angles. This technology has never been tried in a high energy collider operation in the multi-TeV regime. An alternative scenario for the high luminosity IRs using flat beams is currently developed [63, 64], featuring smaller crossing angles and thus requiring no crab cavities to recover the overlap of the colliding bunches.

Like the optics of the accelerator, the detector design is still work in progress. The impact of current design developments, e.g with a forward solenoid instead of the spectrometer dipole, have to be studied.

Acknowledgments

Firstly, I want to thank Prof. Thomas Lohse for giving me the possibility to write this thesis.

I would further like to thank my CERN supervisor Rogelio Tomás for his guidance and support throughout my PhD. He was the one keeping the greater picture in mind when I was focusing too much on the little details.

I am grateful to the project leaders of the FCC study, Michael Benedikt and Frank Zimmermann, for giving me the opportunity to work on this exciting project and entrusting me with representing the interaction region development at various workshops and review meetings.

Daniel Schulte, the leader of the FCC-hh design, for many fruitful discussions and in particular for the suggestion of the scaling with constant apertures and gradients.

I warmly acknowledge the explanations and feedback by Maria Ilaria Besana and Francesco Cerutti. Our discussions on radiation issues were invaluable for the progress of the interaction region design.

I want to thank Barbara Dalena for the fruitful discussions, feedback and her help with handling the field errors and running SixTrack, as well as Antoine Chancé for the collaboration on the lattice integration.

I am in debt of Emilia Cruz-Alaniz who, with the help of Ewen Maclean, implemented the local correction of non-linear field errors and continued the tracking studies after I started writing this thesis. The results would look a lot less convincing if we were still stuck at a DA of $0\,\sigma$. I also appreciate the collaboration with the other members of the IR design team from Oxford: the IR work package leader Andrei Seryi who highlighted my work in various presentations and also Léon van Riesen-Haupt and José Abelleira-Fernández who were the first to actually go through my scripts and help correct errors.

Many thanks also to Andy Langner for helping with the matching of the $L^* = 45\,\mathrm{m}$ lattice and for unintentionally introducing me to plotting with Python.

I am furthermore thankful for the advice and discussions with experts of various fields: Ezio Todesco and Luca Bottura on magnet related issues, Javier Barranco García, Xavier Buffat and Tatiana Pieloni on beam-beam issues and Maria Fiascaris on collimation.

I especially would like to thank my good friend Bastian Härer for proof-reading this thesis and providing detailed feedback.

I am furthermore thankful to Bernhard Holzer for coffee and advice as well as helpful discussions on beam optics issues.

Lastly I want to thank my friends at CERN for making my PhD such a great time.

Appendix

Figure A.1 and A.2 show the gradients for the squeeze of the $L^* = 45\,\text{m}$ and $L^* = 61\,\text{m}$ lattices. Compared to the squeeze of the $L^* = 36\,\text{m}$ lattice shown in Fig. 6.5, no new issues with the ranges occur, except that Q6 in the $L^* = 61\,\text{m}$ lattice gets too weak at low β^*. A work-around in the form of a combined ramp has been suggested.

Figure A.1: Variation of the matching quadrupole gradients in the $L^* = 45\,\mathrm{m}$ lattice during transition from injection to collision optics. The ramp is modeled as a simple gradient increase at $\beta^* = 6\,\mathrm{m}$.
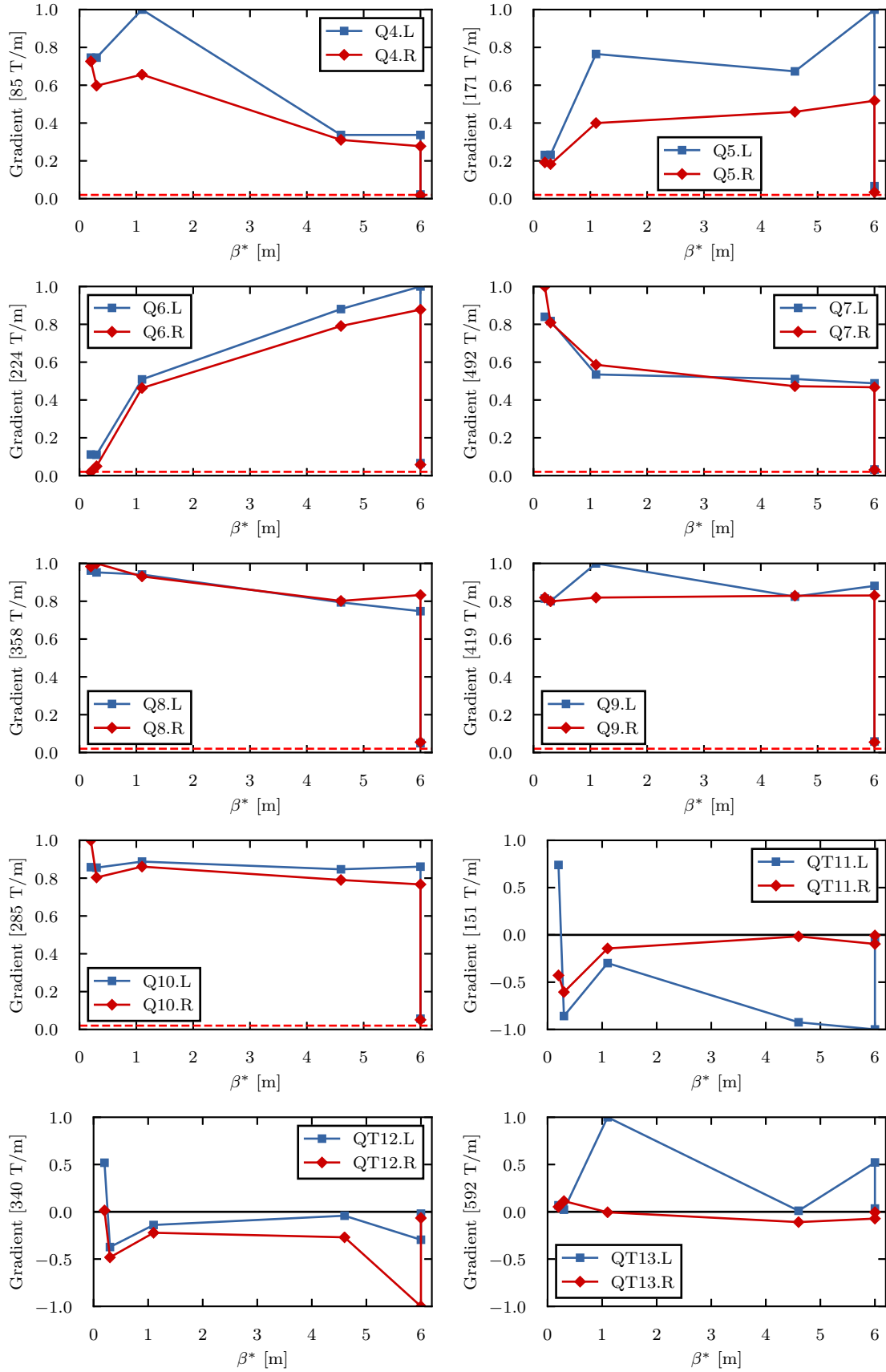
Figure A.2: Variation of the matching quadrupole gradients in the $L^* = 61$ m lattice during transition from injection to collision optics. The ramp is modeled as a simple gradient increase at $\beta^* = 6$ m.
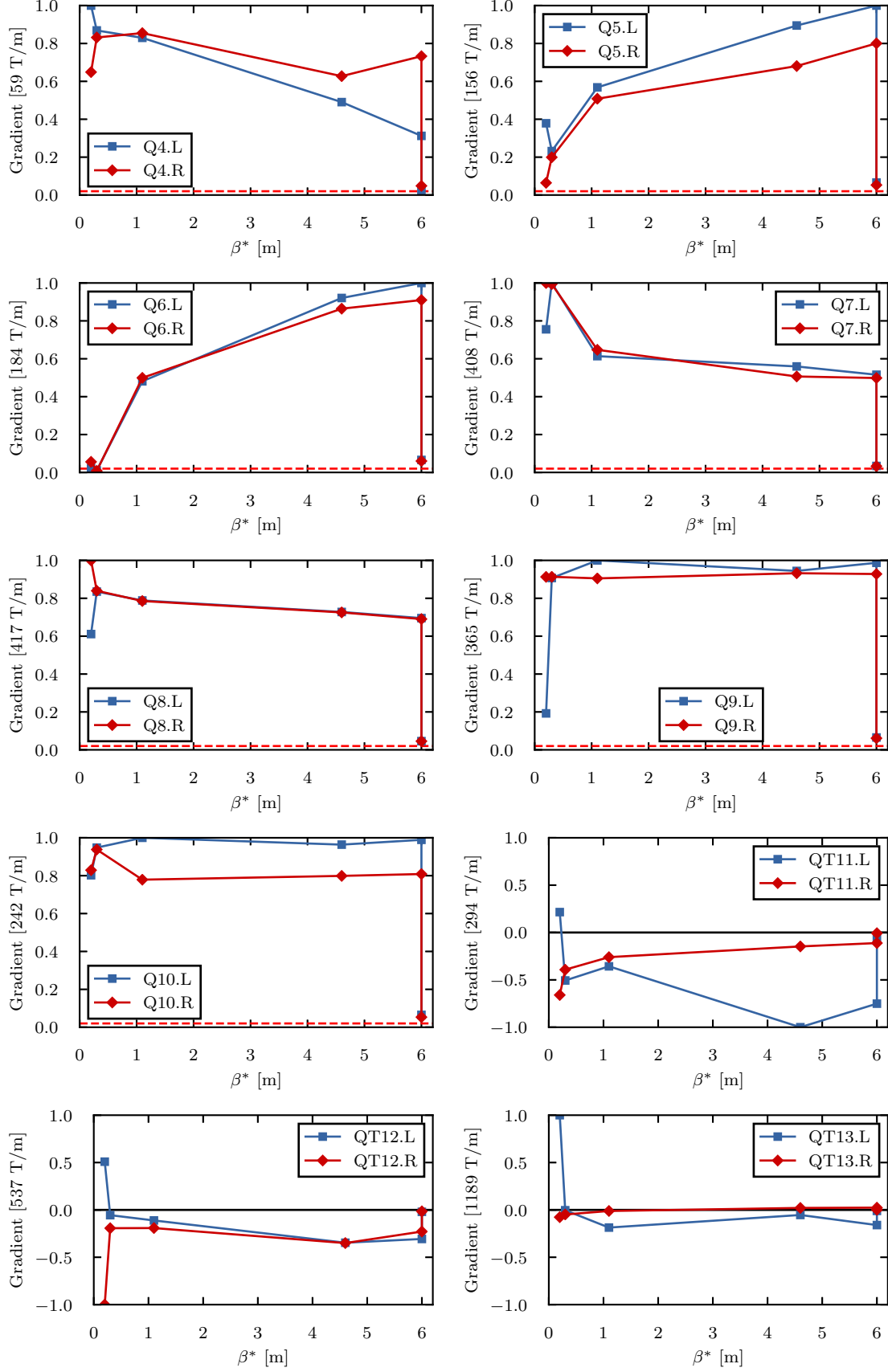
Bibliography

[1] M. I. Besana, F. Cerutti, L. Esposito, and A. Ferrari.

[2] A. Chancé, E. Cruz-Alaniz, B. Dalena, A. Langner, D. Schulte, and R. Tomás.

[3] R. Martin, M. Besana, F. Cerutti, and R. Tomás, "Radiation Load Optimization in the Final Focus System of FCC-hh," in *Proc. of International Particle Accelerator Conference (IPAC'16), Busan, Korea, May 8-13, 2016*, no. 7 in International Particle Accelerator Conference, (Geneva, Switzerland), pp. 1462–1465, JACoW, June 2016. doi:10.18429/JACoW-IPAC2016-TUPMW018.

[4] R. Martin, M. I. Besana, F. Cerutti, A. Langner, R. Tomás, E. Cruz-Alaniz, and B. Dalena, "Interaction region design driven by energy deposition," *Phys. Rev. Accel. Beams*, vol. 20, p. 081005, Aug 2017.

[5] G. Aad *et al.*, "Observation of a new particle in the search for the Standard Model Higgs boson with the ATLAS detector at the LHC," *Phys. Lett. B*, vol. 716, pp. 1–29. 39 p, Aug 2012.

[6] S. Chatrchyan *et al.*, "Observation of a new boson at a mass of 125 GeV with the CMS experiment at the LHC," *Phys. Lett. B*, vol. 716, pp. 30–61. 59 p, Jul 2012.

[7] "The European Strategy for Particle Physics Update 2013. 16th Session of European Strategy Council," May 2013.

[8] "Future Circular Collider Study." `https://fcc.web.cern.ch/`.

[9] T. Behnke *et al.*, "The International Linear Collider - Volume 1: Executive Summary," arXiv:1306.6327. CERN-ATS-2013-037. ILC-REPORT-2013-040, Geneva, Jun 2013.

[10] M. Aicheler *et al.*, "A Multi-TeV Linear Collider Based on CLIC Technology: CLIC Conceptual Design Report," CERN-2012-007. SLAC-R-985, Geneva, 2012.

[11] M. Bicer *et al.*, "First look at the physics case of TLEP," *Journal of High Energy Physics*, vol. 2014, no. 1, p. 164, 2014.

[12] M. Benedikt, D. Schulte, J. Wenninger, and F. Zimmermann, "Challenges for highest energy circular colliders," p. 7 p, Jun 2014.

[13] O. Brüning, O. Dominguez, S. Myers, L. Rossi, E. Todesco, and F. Zimmermann, "HE-LHC beam-parameters, optics and beam-dynamics issues," in *EuCARD-AccNet-EuroLumi Workshop: The High-Energy Large Hadron Collider*, p. 6, Aug 2011. arXiv:1108.1617.

[14] Image by A. Langner.

[15] D. Schulte, "Preliminary Collider Baseline Parameters," Deliverable Report EuroCirCol-D1-1, CERN, 2015.

[16] G. Apollinari, I. Bájar Alonso, O. Brüning, M. Lamont, and L. Rossi, eds., *High-Luminosity Large Hadron Collider (HL-LHC). Preliminary Design Report.* Geneva: CERN, 2015.

[17] D. Schulte *et al.*, "Future Circular Collider Study Hadron Collider Parameters," Tech. Rep. FCC-ACC-SPC-0001, EDMS no. 1342402, CERN, Geneva, 2014.

[18] K. Wille, *The Physics of Particle Accelerators: An Introduction.* Great Clarendon Street, Oxford OX 6DP: Oxford University Press, 2000.

[19] L. C. Teng, "Concerning n-dimensional coupled motions,"FN-229, FNAL, 1971.

[20] M. Giovannozzi, W. Scandale, and E. Todesco, "Dynamic aperture extrapolation in the presence of tune modulation," *Phys. Rev. E*, vol. 57, pp. 3432–3443, Mar 1998.

[21] "MAD - Methodical Accelerator Design." `http://mad.web.cern.ch/mad/`.

[22] "SixTrack - 6D Tracking Code." `http://sixtrack.web.cern.ch/SixTrack/`.

[23] R. De Maria. private communication, March 2017.

[24] A. Apollonio, "LHC Report: astounding availability," *CERN Bulletin*, vol. 28-29, 2016.

[25] The ATLAS Collaboration, "The ATLAS Experiment at the CERN Large Hadron Collider," *Journal of Instrumentation*, vol. 3, no. 08, p. S08003, 2008.

[26] O. S. Brüning, P. Collier, P. Lebrun, S. Myers, R. Ostojic, J. Poole, and P. Proudlock, eds., *LHC Design Report.* Geneva: CERN, 2004.

[27] J.-P. Koutchouk, A. Faus-Golfe, A. Verdier, and S. Weisz, "Modular Optical Design of the LHC Experimental Insertions," in *Proc. of the 5th European Particle Accelerator Conference*, no. 5, p. 911, Jul 1996.

[28] R. Tomás, M. Benedikt, A. Bogomyagkov, L. Bottura, F. Cerutti, L. Esposito, A. Ferrari, B. Haerer, B. Holzer, E. Jensen, M. Koratzinos, R. Martin, L. Medina, D. Schulte, E. Todesco, J. Wenninger, S. White, and F. Zimmermann, "FCC study: parameters and optics for hadron and lepton colliders," *Nuclear and Particle Physics Proceedings*, vol. 273, pp. 149 – 155, 2016. 37th International Conference on High Energy Physics (ICHEP).

[29] R. Bruce, R. De Maria, S. Fartoukh, M. Giovannozzi, S. Redaelli, R. Tomás, and J. Wenninger, "Parameters for HL-LHC aperture calculations and comparison with aperture measurements," Tech. Rep. CERN-ACC-2014-0044, CERN, Geneva, Mar 2014.

[30] M. Fiascaris, R. Bruce, D. Mirarchi, and S. Redaelli, "First Design of a Proton Collimation System for 50 TeV FCC-hh," in *Proc. of International Particle Accelerator Conference (IPAC'16), Busan, Korea, May 8-13, 2016*, no. 7 in International Particle Accelerator Conference, (Geneva, Switzerland), pp. 2423–2426, JACoW, June 2016. doi:10.18429/JACoW-IPAC2016-WEPMW006.

[31] W. Herr and T. Pieloni, "Beam-Beam Effects," in *CAS - CERN Accelerator School: Advanced Accelerator Physics Course*, no. arXiv:1601.05235, p. 29 p, 2014. doi:10.5170/CERN-2014-009.

[32] R. de Maria, "General method for final focus system design for circular colliders," *Phys. Rev. ST Accel. Beams*, vol. 11, p. 031001, Mar 2008.

[33] F. Antoniou *et al.*, "LHC Luminosity Modeling for RUNII," in *Proc. of International Particle Accelerator Conference (IPAC'16), Busan, Korea, May 8-13, 2016*, no. 7 in International Particle Accelerator Conference, (Geneva, Switzerland), pp. 1403–1406, JACoW, June 2016. doi:10.18429/JACoW-IPAC2016-TUPMW002.

[34] A. Ferrari, P. R. Sala, A. Fassò, and J. Ranft, "FLUKA: A multi-particle transport code (program version 2005)." (CERN, Geneva, 2005).

[35] G. Battistoni *et al.*, "Overview of the FLUKA code," *Annals of Nuclear Energy*, vol. 82, pp. 10 – 18, 2015. Joint International Conference on Supercomputing in Nuclear Applications and Monte Carlo 2013, SNA + MC 2013. Pluri- and Transdisciplinarity, Towards New Modeling and Numerical Simulation Paradigms.

[36] S. Roesler, R. Engel, and J. Ranft, "The Monte Carlo event generator DPMJET-III," in *Advanced Monte Carlo for radiation physics, particle transport simulation and applications. Proceedings, Conference, MC2000, Lisbon, Portugal, October 23-26, 2000*, pp. 1033–1038, 2000.

[37] A. Fedynitch and R. Engel, "Revision of the high energy hadronic interaction models PHOJET/DPMJET-III," in *Proc. 14th International Conference on Nuclear Reaction Mechanisms, Varenna, Italy, June 15 - 19, 2015*, (Geneva), pp. 291–300, CERN, CERN, 2015.

[38] N. V. Mokhov, I. L. Rakhno, J. S. Kerby, and J. B. Strait, "Protecting LHC IP1/IP5 Components Against Radiation Resulting from Colliding Beam Interactions," Tech. Rep. LHC-Project-Report-633. FERMILAB-FN-0732., CERN, Geneva, Apr 2003.

[39] D. Tommasini. private communication, July 2016.

[40] W. Riegler, "FCC-hh Detector Overview." presented at FCC Week, March 2015.

[41] L. Bottura and P. Fessia, "What could stop us and when," in *RLIUP: Review of LHC and Injector Upgrade Plans*, 2014.

[42] W. Riegler, "FCC-hh Experiments and Detectors Overview." presented at FCC Week, April 2016.

[43] M. Besana, F. Cerutti, A. Ferrari, W. Riegler, and V. Vlachoudis, "Characterization of the Radiation Field in the FCC-hh Detector," in *Proc. of International Particle Accelerator Conference (IPAC'16), Busan, Korea, May 8-13, 2016*, no. 7 in International Particle Accelerator Conference, (Geneva, Switzerland), pp. 1414–1417, JACoW, June 2016. doi:10.18429/JACoW-IPAC2016-TUPMW005.

[44] X. Buffat, "Beam parameters evolution and luminosity performance." presented at FCC Week, April 2016.

[45] M. Besana, F. Cerutti, S. Fartoukh, R. Martin, and R. Tomás, "Assessment and Mitigation of the Proton-Proton Collision Debris Impact on the FCC Triplet," in *Proc. of International Particle Accelerator Conference (IPAC'16), Busan, Korea, May 8-13, 2016*, no. 7 in International Particle Accelerator Conference, (Geneva, Switzerland), pp. 1410–1413, JACoW, June 2016. doi:10.18429/JACoW-IPAC2016-TUPMW004.

[46] S. Fartoukh, "Achromatic telescopic squeezing scheme and application to the LHC and its luminosity upgrade," *Phys. Rev. ST Accel. Beams*, vol. 16, p. 111002, Nov 2013.

[47] Y. Nosochkov and D. M. Ritson, "The Provision of IP Crossing Angles for the SSC," in *Proc. of the 1993 Particle Accelerator Conference (PAC1993), Washington, D.C., USA, May 17-20, 1993*, no. 15 in Particle Accelerator Conference, (Geneva, Switzerland), pp. 125–127, JACoW, May 1993.

[48] L. Stoel *et al.*, "High Energy Booster Options for a Future Circular Collider at CERN," in *Proc. of International Particle Accelerator Conference (IPAC'16), Busan, Korea, May 8-13, 2016*, no. 7 in International Particle Accelerator Conference, (Geneva, Switzerland), pp. 856–859, JACoW, June 2016. doi:10.18429/JACoW-IPAC2016-MOPOY007.

[49] M. Korostelev, A. Wolski, R. D. Maria, and S. Fartoukh, "Optics Transition between Injection and Collision Optics for the HL-LHC Upgrade Project," in *Proc. of International Particle Accelerator Conference (IPAC'13), Shanghai, China, May 13-17, 2013*, no. 4 in International Particle Accelerator Conference, (Geneva, Switzerland), pp. 1460–1462, JACoW.

[50] E. H. Maclean, R. Tomás, M. Giovannozzi, and T. H. B. Persson, "First measurement and correction of nonlinear errors in the experimental insertions of the CERN Large Hadron Collider," *Phys. Rev. ST Accel. Beams*, vol. 18, p. 121002, Dec 2015.

[51] R. Tomás, M. Giovannozzi, and R. de Maria, "Nonlinear correction schemes for the phase 1 LHC insertion region upgrade and dynamic aperture studies," *Phys. Rev. ST Accel. Beams*, vol. 12, p. 011002, Jan 2009.

[52] P. Vedrine *et al.*, "FCC Main Quadrupoles." presented at FCC Week, April 2016.

[53] M. S. Camillocci, S. Redaelli, R. Tomás, and J. Wenninger, "Combined Ramp and Squeeze to 6.5 TeV in the LHC," in *Proc. of International Particle Accelerator Conference (IPAC'16), Busan, Korea, May 8-13, 2016*, no. 7 in International Particle Accelerator Conference, (Geneva, Switzerland), pp. 1509–1512, JACoW, June 2016. doi:10.18429/JACoW-IPAC2016-TUPMW031.

[54] C. Garion *et al.*, "FCC-hh beam screen studies and cooling scenario." presented at FCC Week, April 2016.

[55] W. Herr, "Features and implications of different LHC crossing schemes," Tech. Rep. CERN-LHC-Project-Report-628, CERN, Geneva, Feb 2003.

[56] O. S. Brüning and S. D. Fartoukh, "Field Quality Specification for the LHC Main Dipole Magnets," Tech. Rep. CERN-LHC-Project-Report-501, CERN, Geneva, Oct 2001.

[57] R. Wolf *et al.*, "Field Error Naming Conventions for LHC Magnets," Engineering Specification LHC-M-ES-0001, EDMS no. 90250, CERN, Oct 2001.

[58] E. Todesco, B. Bellesia, J.-P. Koutchouk, and C. Santoni, "Estimating Field Quality in Low-beta Superconducting Quadrupoles and its Impact on Beam Stability," no. CERN-LHC-PROJECT-Report-1061, 2007.

[59] B. Dalena *et al.*, "First Evaluation of Dynamic Aperture at Injection for FCC-hh," in *Proc. of International Particle Accelerator Conference (IPAC'16), Busan, Korea, May 8-13, 2016*, no. 7 in International Particle Accelerator Conference, (Geneva, Switzerland), pp. 1466–1469, JACoW, June 2016. doi:10.18429/JACoW-IPAC2016-TUPMW019.

[60] M. Giovannozzi, R. D. Maria, and S. Fartoukh, "Specification of a System of Correctors for the Triplets and Separation Dipoles of the LHC Upgrade," in *Proc. of International Particle Accelerator Conference (IPAC'13), Shanghai, China, May 13-17, 2013*, no. 4 in International Particle Accelerator Conference, (Geneva, Switzerland), pp. 2612–2614, JACoW.

[61] E. Cruz-Alaniz, E. H. Maclean, R. Martin, A. Seryi, and R. Tomás, "Non Linear Field Correction Effects on the Dynamic Aperture of the FCC-hh," in *Proc. of International Particle Accelerator Conference (IPAC'17), Copenhagen, Denmark, May 14-19, 2017*, no. 8 in International Particle Accelerator Conference, (Geneva, Switzerland), JACoW, May 2017.

[62] O. S. Brüning, S. D. Fartoukh, M. Giovannozzi, and T. Risselada, "Dynamic Aperture Studies for the LHC Separation Dipoles," Tech. Rep. CERN-LHC-Project-Note-349, CERN, Geneva, Jun 2004.

[63] L. van Riesen-Haupt, J. L. Abelleira-Fernandez, A. Seryi, and E. Cruz-Alaniz, "Exploring the Triplet Parameter Space to optimize the Final Focus of the FCC-hh," in *Proc. of International Particle Accelerator Conference (IPAC'17), Copenhagen, Denmark, May 14-19, 2017*, no. 8 in International Particle Accelerator Conference, (Geneva, Switzerland), JACoW, May 2017.

[64] A. Seryi *et al.*, "Overview of the Design Development of FCC-hh Experimental Interaction Regions," in *Proc. of International Particle Accelerator Conference (IPAC'17), Copenhagen, Denmark, May 14-19, 2017*, no. 8 in International Particle Accelerator Conference, (Geneva, Switzerland), JACoW, May 2017.

,